Prototype Tests for the Liquid Krypton Calorimeter of the CP-Violation Experiment NA48

Diplomarbeit
an der Technischen Universität Wien

durchgeführt von
Georg Viehhauser
2344 Maria Enzersdorf Südstadt, Hohe Wandstr. 32/9

Wien, den 23. September 1993

Georg Vieh...

begutachtet von
Univ. Prof. Dr. Meinhard Regler

Wien, den 23. September 1993

Dr. M. Regler

Contents

Introduction

This work is the result of a one year stay as a technical student in the NA48 group at the European Center for Nuclear Research CERN from May 1992 to May 1993.

The NA48 experiment is a fixed target experiment at the CERN Super Proton Synchrotron (SPS) to study direct CP violation in neutral kaon decays. The aim of the experiment is the measurement of the ratio of the CP violation parameters ε'/ε. Chapter 1 will explain the origin of these parameters and our current knowledge of their size. Chapter 2 will give a description of the NA48 experiment.

A crucial part of the experiment will be a photon calorimeter filled with liquid krypton. It has to meet very ambitious demands concerning the high rate capability and the energy, space and time resolutions. In chapter 3 the principles of electromagnetic calorimetry and ionization chambers are reviewed.

In 1992 two test beam exposures of a prototype of the liquid krypton calorimeter were performed. A description of these tests will be given in chapter 4.

During the two tests I was engaged in the setup and operation of the trigger counters and the flash analog to digital converter (FADC) system. During the data-taking phase I was involved in the actual data-taking. After the runs I participated in the analysis of the test beam results. This work consisted of programming parts of the official off-line code for the test beam analysis and of the study of particular aspects of the prototype tests. I analyzed the data from the FADC system and produced results for the energy, space and time resolutions. I also performed an investigation of non-uniformity effects in the calorimeter response. The results of my analysis are described in chapter 5, followed by a compressed summary in chapter 6.

Chapter 1: Phenomenology of CP Violation

Discrete Transformations in Quantum Physics

The study of symmetries and the conservation laws which follow from the Noether theorem [Noe18] has played an important role in physics. Examples are the conservation of the momentum or of the energy in systems which are invariant under space or time transformations.

In quantum physics, discrete transformations such as parity exchange, charge conjugation and time reversal are added to the classical continuous transformations [Wic58]. Invariance under such discrete transformations exists if processes were to develop in the same way in a world that is somehow a mirror image to our world. For this reason, these symmetries are sometimes referred to as mirror symmetries. During the study of discrete transformations, it turned out that well-accepted principles such as the symmetry between left and right had to be revised.

Parity

Perhaps the most familiar discrete transformation is the reflection of space in the origin. This transformation is described by the parity operator P.

$$\mathrm{P}\,\Psi(\mathbf{r}) \rightarrow \Psi(-\mathbf{r}) \tag{1.1}$$

where $\Psi(\mathbf{r})$ is a scalar state in the Hilbert space and $\mathbf{r}$ is the spatial coordinate. The effects of parity transformation can be studied for a particle with a given spin in a central field. Its Hamiltonian

$$\mathrm{H} = \frac{p^2}{2m} + V(|\mathbf{r}|) + \mathbf{s}\cdot\left(\mathbf{r}\times\mathbf{p}V_1(|\mathbf{r}|)\right) \tag{1.2}$$

with the vector operators $\mathbf{r}$, $\mathbf{p}$ and $\mathbf{s}$ is not changed by the parity transformation

$$\mathrm{P}^{-1}\,\mathbf{r}\,\mathrm{P} = -\mathbf{r}, \qquad \mathrm{P}^{-1}\,\mathbf{p}\,\mathrm{P} = -\mathbf{p} \qquad \text{and} \qquad \mathrm{P}^{-1}\,\mathbf{s}\,\mathrm{P} = \mathbf{s}. \tag{1.3}$$

The commutation laws and the equations of motion stay the same. Thus the system is invariant under a parity transformation.

In quantum physics, the concept of an outer parity can be extended to an inner parity. This expansion is a consequence of the production and destruction of particles and has nothing essential to do with the spatial part of the wave function.

The parity of the π^- particle can be obtained from the experimental observation of the capture of the pions in deuterium with the production of two neutrons [Pan51], [Chi54]

$$\pi^- + d \rightarrow n + n \ . \tag{1.4}$$

The pion has spin 0 and the deuteron spin 1, which gives $J=1$ for the total angular momentum. For the right side, only the state with $L=1$ and $S=0$, which is antisymmetric for the exchange of the particles, is allowed by the Pauli law. Therefore the parity of the pion is $(-1)^L$, in this case -1.

Also the parity of the neutral pion is negative as can be seen from the experimental results for the double Dalitz-decay

$$\pi^0 \rightarrow \gamma^* + \gamma^* \rightarrow e^+ + e^- + e^+ + e^- . \tag{1.5}$$

The negative parity of the pion should favor polarization vectors for the virtual photons which are perpendicular to each other. This prediction was confirmed by measuring the distribution of the angle between the electron-positron pairs [Pla59].

Charge Conjugation

Charge conjugation changes a particle into its antiparticle. All additive quantum numbers like charge or the lepton number change their sign whereas, for example, the mass remains the same.

Again, some particles can be seen as eigenstates of the charge conjugation operator. However, this is only possible for neutral particles. The charge conjugation eigenvalue of the photon is -1, as electromagnetic fields are produced by charge and current densities that change their sign under charge conjugation. The π^0 particle decays into two photons and therefore has the charge conjugation eigenvalue +1.

It was long believed that nature's laws show invariance under discrete transformations. It was not before 1956 that Lee and Yang pointed out that there was no experimental evidence for the validity of mirror symmetries in processes induced by the weak interaction [Lee56]. Indeed, shortly after that in 1957, violation of parity conservation was found in beta decay [Wu57] and the decay of pions and muons [Gar57], [Fri57]. Violation of parity symmetry in these processes is equivalent to the violation of symmetry under charge conjugation [Lee57].

This can be illustrated by the fact that only left-handed neutrinos or right-handed antineutrinos exist in nature. A charge conjugation or parity transformation of this particle would lead to an unphysical state. Yet the invariance under CP transformation, the combination of both, is not forbidden by this argument. A CP-transformation would transform a left-handed neutrino in a right-handed antineutrino and the other way round, thus connecting physical states.

Time Reversal

Time reversal, as defined by Wigner [Wig32], leads to the change of the sign of all momenta and angular momenta, whereas the spatial coordinates remain unchanged.

The question of, whether there is a distinct direction in time, has already played a crucial role in thermodynamics. There, the answer was that many-particle systems develop in the direction of increasing entropy. The equations of microscopic systems on the other hand show a different behavior. If $\Psi(\mathbf{r},t)$ is a solution to the Schrödinger equation then $\Psi^*(\mathbf{r},-t)$ is also a solution.

Non-invariance under time reversal has been intensively searched for and experiments have already reached a remarkable accuracy [Eic92].

The most accurate tests of time reversal invariance search for an electric dipole moment (EDM) of particles with spin, especially of atoms [For84] or of the neutron. One limiting factor of the accuracy in the latter experiments is the velocity of the neutrons which fakes a dipole moment. Therefore experiments in the past used very slow Neutron beams [Dre68], [Ram78] and, more recently, ultra cold neutrons [Alt81], [Pen84]. The combined result of these experiments gives a limit on the electric dipole moment of the neutron of

$$|d_n| < 12 \times 10^{-26} e\,\mathrm{cm} \tag{1.6}$$

at the 95% confidence level [Ram90].

The question of invariance under time reversal is connected to the question of invariance under CP transformation by the CPT theorem.

The CPT Theorem

It was shown by Lüders and Pauli that rather loose requirements for a field theory, like invariance under proper Lorentz transformations and locality, lead to the invariance under the succession of the three discrete transformations independent of their order [Lüd54], [Pau55], [Sch53]. This statement is called the CPT theorem.

As a consequence of the CPT theorem lifetimes and masses of particles and their antiparticles have to be the same. The mass difference can be tested most precisely in the kaon system. The experimental limit is [PDG92]

$$\frac{m_{\overline{K}} - m_K}{m_K} \leq 10^{-18} \tag{1.7}$$

at the 90% confidence level.

It follows from the CPT theorem that a violation of CP invariance includes a violation of invariance under time reversal.

CP Violation in the Neutral Kaon System

The Neutral Kaon System

Our knowledge of violation of invariance under the CP transformation is currently limited to its observation in the neutral kaon system.

The assumption of invariance under charge conjugation (which was still thought to be valid at that time) was used by Gell-Mann and Pais to predict a long-lived partner to the K^0 particle [Gel55]. Both, the long and the short lived kaon — called from then on K_2 and K_1 — are mixtures of the strangeness eigenstates K^0 ($SK^0 = +K^0$) and $\overline{K}^0$ ($S\overline{K}^0 = -\overline{K}^0$). The argument was that a charge conjugation of the experimentally observed decay $K^0 \to \pi^+\pi^-$ would change the initial state into $\overline{K}^0$ and with it the sign of the charge conjugation eigenvalue, but leave the final state the same. This contradiction is avoided with the particle mixtures

$$K_1 = \frac{K^0 + \overline{K}^0}{\sqrt{2}} \quad \text{and} \quad K_2 = \frac{K^0 - \overline{K}^0}{\sqrt{2}} \; . \tag{1.8}$$

These particles were seen as even and odd charge conjugation eigenstates. Only the K_1 can decay into two pions whereas the decay of the K_2 into two pions is forbidden by charge conjugation invariance. The two neutral kaons differ in lifetime due to the different phase space for decays. The mass of the two particles is slightly different.

$$\tau_S = (0.8922 \pm 0.0020) \times 10^{-10}\, s$$
$$\tau_L = (5.17 \pm 0.04) \times 10^{-8}\, s$$
$$m_{K^0} = 497.671 \pm 0.031\; MeV$$
$$\Delta m = \left| m_{K_S} - m_{K_L} \right| = (0.5351 \pm 0.016) \times 10^{-12}\; MeV$$

Tab. 1.1: Properties of the neutral kaon [PDG92].

After the discovery of violation of charge conjugation symmetry it seemed sufficient to replace charge conjugation by the CP transformation with

$$\mathrm{CP}\,\mathrm{K}_1 = +\mathrm{K}_1 \qquad \text{and} \qquad \mathrm{CP}\,\mathrm{K}_2 = -\mathrm{K}_2. \tag{1.9}$$

As $\mathrm{CP}(\pi^+\pi^-) = +(\pi^+\pi^-)$ again the decay of K_2 into two pions should be forbidden. Decays into 3π-states should only be possible for K_2 as $\mathrm{CP}|3\pi^0\rangle = -|3\pi^0\rangle$ and $\mathrm{CP}|\pi^+\pi^-\pi^0\rangle = (-1)^{L+1}|\pi^+\pi^-\pi^0\rangle$, where states with $L \neq 0$ are suppressed by the angular momentum barrier.

But in 1964 CP violating $\mathrm{K}_2 \rightarrow \pi^+\pi^-$ decays were observed [Chr64].

	$\mathrm{K}_S \rightarrow \pi^+\pi^-$	$(68.61 \pm 0.28)\%$
	$\mathrm{K}_S \rightarrow \pi^0\pi^0$	$(31.39 \pm 0.28)\%$
	$\mathrm{K}_L \rightarrow \pi^0\pi^0\pi^0$	$(21.6 \pm 0.8)\%$
	$\mathrm{K}_L \rightarrow \pi^+\pi^-\pi^0$	$(12.38 \pm 0.21)\%$
	$\mathrm{K}_L \rightarrow \pi^\pm\mu^\mp\overline{\nu}(\nu)$	$(27.0 \pm 0.4)\%$
	$\mathrm{K}_L \rightarrow \pi^\pm e^\mp\overline{\nu}(\nu)$	$(38.7 \pm 0.5)\%$
CP-violating:		
	$\mathrm{K}_L \rightarrow \pi^+\pi^-$	$(2.03 \pm 0.04) \times 10^{-3}$
	$\mathrm{K}_L \rightarrow \pi^0\pi^0$	$(0.909 \pm 0.035) \times 10^{-3}$

Tab. 1.2: Relative branching ratios of the dominant decay channels of the neutral kaon [PDG92]. The sign of the hadron in the semileptonic decay follows from the $\Delta S = \Delta Q$ rule.

Kaon State Mixing[1]

Following a Weisskopf-Wigner approximation [Wei30], [Nac91] the time evolution of a mixture $|\Psi(\tau)\rangle = a(\tau)|\mathrm{K}^0\rangle + b(\tau)|\overline{\mathrm{K}}^0\rangle$ can be described by the mass and the decay matrices $\mathbf{M}$ and Γ

$$-i\frac{d}{d\tau}\begin{pmatrix} a(\tau) \\ b(\tau) \end{pmatrix} = H\begin{pmatrix} a(\tau) \\ b(\tau) \end{pmatrix} = \left(\mathbf{M} - i\frac{\Gamma}{2}\right)\begin{pmatrix} a(\tau) \\ b(\tau) \end{pmatrix}, \tag{1.10}$$

where $\mathbf{M}$ and Γ are hermitian 2×2 matrices

[1]The following analysis was first applied to the kaon system by Lee, Oehme and Yang [Lee57] and then used in many other works and reviews, see for example: [Wu64], [Lee65], [Lee66], [Kle76], [Cro83], [Ste89] and other talks there, [Nac91], [Pas92], [Eic92].

$$\mathbf{M}=\begin{pmatrix} M_{11} & M_{12} \\ M_{21} & M_{22} \end{pmatrix} \quad \text{and} \quad \Gamma=\begin{pmatrix} \Gamma_{11} & \Gamma_{12} \\ \Gamma_{21} & \Gamma_{22} \end{pmatrix}. \tag{1.11}$$

The decomposition of the Hamiltonian in (1.10) follows from perturbation theory:

$$H_{ab}=m_K\delta_{ab}+\langle a|H_{weak}|b\rangle+\sum_n \frac{\langle a|H_{weak}|n\rangle\langle n|H_{weak}|b\rangle}{m_K-E_n+i\varepsilon}, \tag{1.12}$$

where the first order Hamiltonian changes strangeness by $\Delta S = 2$ and the second order Hamiltonian by $\Delta S = 1$. H_{ab} decomposes in

$$M_{ab}=m_K\delta_{ab}+\langle a|H_{weak}|b\rangle+\mathrm{P}\sum_n \frac{\langle a|H_{weak}|n\rangle\langle n|H_{weak}|b\rangle}{m_K-E_n} \tag{1.13}$$

and

$$\Gamma_{ab}=2\pi\sum_n \langle a|H_{weak}|n\rangle\langle n|H_{weak}|b\rangle\delta(E_n-m_K)\,. \tag{1.14}$$

Γ_{ab} is determined by the weak Hamiltonian, whereas M_{ab} is related to H_{strong}, H_{γ} and H_{weak}, as $\langle a|(H_{strong}+H_{\gamma})|b\rangle=m_K\delta_{ab}$.

In the following, CPT invariance will be assumed. This requires that $M_{11}=M_{22}$ and $\Gamma_{11}=\Gamma_{22}$.

The solutions of the eigenvalue problem

$$\left(\mathbf{M}-i\frac{\Gamma}{2}\right)|\Psi_{\pm}\rangle=\lambda_{\pm}|\Psi_{\pm}\rangle \tag{1.15}$$

can be written as

$$|\Psi_{\pm}\rangle=\frac{1}{\sqrt{|p|^2+|q|^2}}\left(p|\mathrm{K}^0\rangle\pm q|\overline{\mathrm{K}}^0\rangle\right) \tag{1.16}$$

with the parameters $p^2=\Gamma_{12}+iM_{12}$ and $q^2=\Gamma_{21}+iM_{21}=\Gamma_{12}{}^*+iM_{12}{}^*$. The corresponding time constants are

$$\lambda_{\pm}=M_{\pm}-i\frac{\Gamma_{\pm}}{q}=M_{11}-i\frac{\Gamma_{11}}{2}+ipq. \tag{1.17}$$

The use of the asymmetry parameter

$$\varepsilon=\frac{p-q}{p+q} \tag{1.18}$$

and the CP eigenstates K_1 and K_2 instead of the strangeness eigenstates K^0 and $\overline{K}^0$ results in

$$|\Psi_+\rangle = \frac{1}{\sqrt{1+|\varepsilon|^2}}\left(|K_1\rangle + \varepsilon|K_2\rangle\right) = |K_S\rangle \tag{1.19}$$

$$|\Psi_-\rangle = \frac{1}{\sqrt{1+|\varepsilon|^2}}\left(|K_1\rangle - \varepsilon|K_2\rangle\right) = |K_L\rangle\ . \tag{1.20}$$

These are the physical particles K_L and K_S. These states are no longer orthogonal, since

$$\langle K_L|K_S\rangle = \frac{2\,\mathrm{Re}\,\varepsilon}{1+|\varepsilon|^2}\ . \tag{1.21}$$

Mixing of CP-eigenstates in the physical states is described by $\varepsilon \neq 0$. Assuming that the $\Delta S=\Delta Q$ rule is valid, the charge asymmetry in semi-leptonic decays

$$\delta = \frac{\Gamma(K_L \to \pi^- l^+ \nu) - \Gamma(K_L \to \pi^+ l^- \nu)}{\Gamma(K_L \to \pi^- l^+ \nu) + \Gamma(K_L \to \pi^+ l^- \nu)} \tag{1.22}$$

can be calculated using the amplitudes

$$a_l = \langle \pi^- l^+ \nu|H|K^0\rangle \qquad \text{and} \qquad \overline{a_l} = \langle \pi^+ l^- \overline{\nu}|H|\overline{K}^0\rangle \tag{1.23}$$

with the transformation property (assuming CP invariance)

$$a_l = \langle \pi^- l^+ \nu|(CP)^{-1}\,CP\ H\ (CP)^{-1}\,CP|K^0\rangle = -\overline{a_l}\,. \tag{1.24}$$

The charge asymmetry becomes

$$\delta = \frac{2\,\mathrm{Re}\,\varepsilon}{1+|\varepsilon|^2}\,. \tag{1.25}$$

Experimentally, this value has been determined to be [PDG92]

$$\delta = (0.327 \pm 0.012)\%. \tag{1.26}$$

Isospin Analysis

In two-pion decays the final state wave function can be divided into wave functions of definite isospin. The angular momentum of the pion system vanishes as the kaon is a spinless particle. Therefore the spatial wave function is symmetric. Pions are mesons and thus the isospin wave function must also be symmetric, allowing only the isospin states I=0 and I=2.

$$|+-\rangle = \sqrt{\frac{2}{3}}|I=0\rangle + \frac{1}{\sqrt{3}}|I=2\rangle \qquad (1.27)$$

$$|00\rangle = -\frac{1}{\sqrt{3}}|I=0\rangle + \sqrt{\frac{2}{3}}|I=2\rangle \qquad (1.28)$$

where $|+-\rangle$ stands for a $\pi^+\pi^-$-state and $|00\rangle$ for a $\pi^0\pi^0$-state.

Let $\langle I=0|T|\mathrm{K}\rangle = A_0 e^{i\delta_0}$ with the transition operator T, then $\langle I=0|T|\overline{\mathrm{K}}\rangle = A_0^* e^{i\delta_0}$ because of CPT invariance. Similarly it follows from the definition $\langle I=2|T|\mathrm{K}\rangle = A_2 e^{i\delta_2}$ that $\langle I=2|T|\overline{\mathrm{K}}\rangle = A_2^* e^{i\delta_2}$. A_I describes the weak decay amplitude, whereas δ_I is the s = 0 strong scattering phase for a two-pion final state with isospin I. Adopting a popular phase choice of Wu and Yang A_0 will be defined as a real quantity in the following analysis[2] [Wu64].

The experimentally accessible quantities

$$\eta_{+-} = \frac{\langle +-|T|\mathrm{K}_L\rangle}{\langle +-|T|\mathrm{K}_S\rangle} \quad \text{and} \quad \eta_{00} = \frac{\langle 00|T|\mathrm{K}_L\rangle}{\langle 00|T|\mathrm{K}_S\rangle} \qquad (1.29)$$

can now be written using the parameters

$$\varepsilon = \frac{\langle I=0|T|\mathrm{K}_L\rangle}{\langle I=0|T|\mathrm{K}_S\rangle} \qquad (1.30)$$

$$\varepsilon' = \frac{1}{\sqrt{2}}\left[\frac{\langle I=2|T|\mathrm{K}_L\rangle}{\langle I=0|T|\mathrm{K}_S\rangle} - \varepsilon\frac{\langle I=2|T|\mathrm{K}_L\rangle}{\langle I=0|T|\mathrm{K}_S\rangle}\right] = \frac{i}{\sqrt{2}}\frac{\mathrm{Im}\,A_2}{A_0}e^{i(\delta_2-\delta_0)} \qquad (1.31)$$

$$\omega = \frac{\langle I=2|T|\mathrm{K}_S\rangle}{\langle I=0|T|\mathrm{K}_S\rangle} = \frac{\mathrm{Re}\,A_2}{A_0}e^{i(\delta_2-\delta_0)} \qquad (1.32)$$

as

$$\eta_{+-} = \varepsilon + \frac{\varepsilon'}{1+\frac{\omega}{\sqrt{2}}} \quad \text{and} \quad \eta_{00} = \varepsilon - \frac{2\varepsilon'}{1-\sqrt{2}\omega}. \qquad (1.33)$$

The experimentally observed values are [PDG92]

$$|\eta_{+-}| = (2.268 \pm 0.023)\times 10^{-3} \quad \text{and} \quad |\eta_{00}| = (2.253 \pm 0.024)\times 10^{-3}. \qquad (1.34)$$

[2]This definition is possible as only $|A|^2$ is experimentally accessible.

The Parameters ε and ε′

The mixing of CP-eigenstates in the physical particles is described by the parameter ε. CP violation due to state mixing is called indirect CP violation. The parameter ε can be related to the mass and the decay matrix:

$$\varepsilon \cong \frac{\operatorname{Im} M_{12} + i \operatorname{Im} \frac{\Gamma_{12}}{2}}{\lambda_S - \lambda_L}. \tag{1.35}$$

The phase of ε can be determined from (1.13) [Lee66]. One obtains

$$2 \operatorname{Im} \Gamma_{12} = \Gamma_{12} - \Gamma_{12}^{*} = \pi \sum_n \rho_n \left(A_n^{*2} - A_n^{2} \right) \tag{1.36}$$

with ρ_n giving an appropriate phase space density parameter. With the Wu-Yang phase definition, $\operatorname{Im}\Gamma_{12}$ vanishes for $I = 0$ final states. The other eigenstates of $H_{strong} + H_{\gamma}$ contribute very little to $\operatorname{Im}\Gamma_{12}$. For $I = 2$ two-pion decays the contributions are only of the order $O(A_2 / A_0)$. Three-pion decays also contribute little because of the small three-body phase space. Therefore

$$\varepsilon = |\varepsilon| e^{i\Phi_\varepsilon} \tag{1.37}$$

with

$$\Phi_\varepsilon \cong \arctan\left(-\frac{2(M_S - M_L)}{\Gamma_S - \Gamma_L} \right) \cong \arctan\left(-\frac{2\Delta m}{\Gamma_{SW}} \right) \tag{1.38}$$

and, as $\Delta m \cong -\frac{\Gamma}{2}$ (tab. 1.1),

$$|\varepsilon| \cong \frac{\operatorname{Im} M_{12}}{\sqrt{2}\Delta m}. \tag{1.39}$$

Indirect CP-violation is connected to non-vanishing off-diagonal elements in the mass matrix. The phase of ε is determined from fits to the experimental data [PDG92] to be

$$\Phi_\varepsilon \cong 43.68° \pm 0.14°. \tag{1.40}$$

The second parameter describing CP violation, ε′, is non-zero if there is an interference between the two amplitudes A_0 and A_2 with a relative complex phase. This kind of CP violation is called direct CP violation as it includes a direct decay of the CP-odd eigenstate K_2 into CP-even two-pion states.

Using (1.31), the phase of this second parameter, $\Phi_{\varepsilon'}$, is fully determined by the phase shifts δ_0 and δ_2. It can be approximated by [Wah89]

$$\Phi_{\varepsilon'} \cong 45°\pm15°, \tag{1.41}$$

which is very near to Φ_{ε}.

The parameter ω describes non-CP-violating $\Delta I = \frac{3}{2}$ decays and is relatively small (ω≅0.045). Therefore, it can be neglected and one obtains from (1.33) the Wu-Yang relations

$$\eta_{+-} \cong \varepsilon + \varepsilon' \quad \text{and} \quad \eta_{00} \cong \varepsilon - 2\varepsilon'. \tag{1.42}$$

The similarity of the phases of ε and ε′ allows a relationship between the parameters describing direct and indirect CP-violation and experimentally measurable quantities to be obtained

$$\left|\frac{\eta_{00}}{\eta_{+-}}\right|^2 = \left|\left(\frac{\langle 00|T|\mathrm{K}_L\rangle}{\langle 00|T|\mathrm{K}_S\rangle}\middle/\frac{\langle +-|T|\mathrm{K}_L\rangle}{\langle +-|T|\mathrm{K}_S\rangle}\right)\right|^2 \cong 1 - 6\,\mathrm{Re}\frac{\varepsilon'}{\varepsilon}. \tag{1.43}$$

Theoretical Models of CP Violation

Milliweak and Superweak Models

Theoretical models of CP violation can be divided in milliweak and superweak models, depending on the order of the weak interaction Hamiltonian in the perturbation development that dominates the matrix element in (1.12).

The first explanation of the experimental observation of CP violation was the superweak model of Wolfenstein [Wol64]. It is a purely phenomenological model, in which the kaon state mixing is induced by a very weak new interaction that changes strangeness by $\Delta S = 2$. Due to the weakness of the interaction CP violation should only occur in the kaon system because of the smallness of the mass difference between the neutral kaons. Superweak models predict a zero value for ε′.

CP Violation in the Standard Model

As Kobayashi and Maskawa pointed out [Kob73], CP violation is compatible with the electroweak theory in a world with six quarks, classified in three left-handed doublets and six right-handed singlets

$$q_{L1}^{I} = \begin{pmatrix} u^{I} \\ d^{I} \end{pmatrix}_{L},\ q_{L2}^{I} = \begin{pmatrix} c^{I} \\ s^{I} \end{pmatrix}_{L},\ q_{L3}^{I} = \begin{pmatrix} t^{I} \\ b^{I} \end{pmatrix}_{L} \quad \text{and} \quad u_{R}^{I},\ d_{R}^{I},\ c_{R}^{I},\ s_{R}^{I},\ t_{R}^{I},\ b_{R}^{I} \tag{1.44}$$

where I characterizes these quarks as interaction eigenstates. CP violation is possible because the interaction eigenstates are different from the mass eigenstates.

The couplings of the quark multiplets to the gauge bosons are derived from the kinetic energy term in the Lagrangian

$$L_{kin} = \bar{q}_{Li}^{I} \gamma^{\mu} \left(i\partial_{\mu} - \frac{g}{2} \vec{\tau} \vec{W}_{\mu} - \frac{g'}{2} Y B_{\mu} \right) q_{Li}^{I} + \bar{q}_{Ri}^{I} \gamma^{\mu} \left(i\partial_{\mu} - \frac{g'}{2} Y B_{\mu} \right) q_{Ri}^{I} . \tag{1.45}$$

In this model, masses are generated through quark-Higgs Yukawa couplings with a single Higgs doublet

$$L_{Yukawa} = G_{d}^{ij} \left(\bar{u}_{Li}^{I}, \bar{d}_{Li}^{I} \right) \begin{pmatrix} \Phi^{+} \\ \Phi^{0} \end{pmatrix} d_{Rj}^{I} + F_{u}^{ij} \left(\bar{u}_{Li}^{I}, \bar{d}_{Li}^{I} \right) \begin{pmatrix} \Phi^{0*} \\ -\Phi^{-} \end{pmatrix} u_{Rj}^{I} + h.c. . \tag{1.46}$$

The gauge symmetry is spontaneously broken by assigning a vacuum expectation value to the neutral member of the scalar doublet

$$\langle \Phi \rangle = \left\langle \begin{pmatrix} \Phi^{+} \\ \Phi^{0} \end{pmatrix} \right\rangle = \begin{pmatrix} 0 \\ \frac{v}{\sqrt{2}} \end{pmatrix} . \tag{1.47}$$

This generates the mass terms

$$L_{mass} = \frac{v}{\sqrt{2}} \left(\bar{u}_{Li}^{I} F_{u}^{ij} u_{Rj}^{I} + \bar{d}_{Li}^{I} G_{d}^{ij} d_{Rj}^{I} \right) + h.c. = \left(\bar{u}_{Li}^{I} M_{u}^{ij} u_{Rj}^{I} + \bar{d}_{Li}^{I} M_{d}^{ij} d_{Rj}^{I} \right) + h.c. \tag{1.48}$$

with the mass matrices M_u and M_d. These matrices are neither necessarily symmetric nor hermitian. To find the physical or mass eigenstates for the quarks, one has to diagonalize the mass matrices

$$M_{u}^{diag} = U_{L}^{\dagger} M_{u} U_{R} = \begin{pmatrix} m_{u} & 0 & 0 \\ 0 & m_{c} & 0 \\ 0 & 0 & m_{t} \end{pmatrix} \quad \text{and} \quad M_{d}^{diag} = D_{L}^{\dagger} M_{u} D_{R} = \begin{pmatrix} m_{d} & 0 & 0 \\ 0 & m_{s} & 0 \\ 0 & 0 & m_{b} \end{pmatrix} . \tag{1.49}$$

The charged current interaction in (1.45) becomes

$$L_{c.c.} = \frac{g}{\sqrt{2}} \left(\bar{u}_{Li}^{I} \gamma_{\mu} d_{Li}^{I} W_{\mu}^{+} + \bar{d}_{Li}^{I} \gamma_{\mu} u_{Li}^{I} W_{\mu}^{-} \right) = \frac{g}{\sqrt{2}} \left(\bar{u}_{Li} \gamma_{\mu} V_{ij} d_{Lj} W_{\mu}^{+} + \bar{d}_{Li} \gamma_{\mu} V_{ij}^{\dagger} u_{Lj} W_{\mu}^{-} \right), \tag{1.50}$$

if the weak interaction eigenstates are replaced by the mass eigenstates. The unitary matrix $V = U_{L}^{\dagger} D_{L}$ describes the mixing of quarks in the coupling to the W-bosons and is therefore called the flavor mixing matrix or the Cabibbo-Kobayashi-Maskawa (CKM) matrix. It can be parametrized with four quantities, three rotation angles and one phase. It was the merit of Kobayashi and Maskawa to show that the single phase parameter allows for CP violation in the standard model. The parametrization that is advocated by the Particle Data Group is

$$V = \begin{pmatrix} c_{12}c_{13} & s_{12}c_{13} & s_{13}e^{-i\delta_{13}} \\ -s_{12}c_{23} - c_{12}s_{23}s_{13}e^{i\delta_{13}} & c_{12}c_{23} - s_{12}s_{23}s_{12}e^{i\delta_{13}} & s_{23}c_{13} \\ s_{12}s_{23} - c_{12}c_{23}s_{13}e^{i\delta_{13}} & -c_{12}s_{23} - s_{12}c_{23}s_{13}e^{i\delta_{13}} & c_{23}c_{13} \end{pmatrix} \tag{1.51}$$

where c_{ij} stands for $\cos\Theta_{ij}$ and s_{ij} for $\sin\Theta_{ij}$ with i,j = 1,2,3 [PDG92].

To allow for CP violation several requirements that can be summarized by the condition [Jar85]

$$\det C\left(M_u^2, M_d^2\right) \neq 0 \quad \text{with} \quad iC = \left[M_u M_u^\dagger, M_d M_d^\dagger\right] \tag{1.52}$$

have to be fulfilled by the CKM matrix.

CP-violating effects in the standard model are proportional to J, which is defined by

$$\det C\left(M_u^2, M_d^2\right) = -2T\left(M_u^2\right)B\left(M_d^2\right)J, \tag{1.53}$$

where

$$T\left(M_u^2\right) = \left(m_t^2 - m_u^2\right)\left(m_t^2 - m_c^2\right)\left(m_c^2 - m_u^2\right) \tag{1.54}$$

$$B\left(M_d^2\right) = \left(m_b^2 - m_d^2\right)\left(m_b^2 - m_s^2\right)\left(m_s^2 - m_d^2\right) \tag{1.55}$$

$$\text{and} \quad J = \mathrm{Im}\left(V_{11}V_{22}V_{12}^*V_{21}^*\right) = \mathrm{Im}\left(V_{22}V_{33}V_{23}^*V_{32}^*\right) = \ldots \tag{1.56}$$

From experimental results for the parameters of the CKM-Matrix follows [Eic92]

$$J \leq 10^{-4}. \tag{1.57}$$

Calculation of ε and ε′

CP-violating kaon decays are flavor changing processes with a complex amplitude. Two classes of Feynman diagrams have this property. Box diagrams describe processes with indirect CP violation and have to be calculated for the determination of ε (fig. 1.1). Penguin diagrams describe processes with direct CP violation and can be used to compute ε′ (fig. 1.2). The detailed calculation of these processes is difficult. So far, agreement has not been reached on the results for ε′ [Bur93], [Ciu93], [Frö91], [Hei92]. The results of these calculations cover the range

$$-0.1 \times 10^{-3} < \frac{\varepsilon'}{\varepsilon} < 6 \times 10^{-3} \tag{1.58}$$

for a top quark mass between 100 and 150 GeV. The mass of the top quark influences the results as a higher mass of the top quark reduces the value of ε'/ε [Fly89].

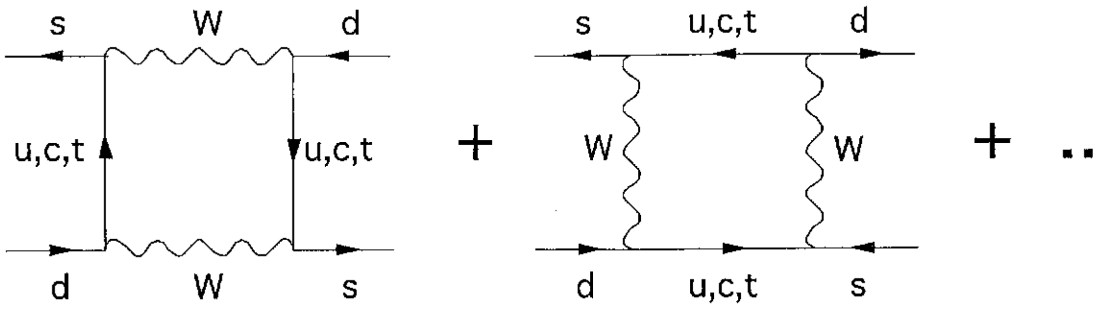

Fig. 1.1: Box Diagrams contributing to indirect CP violation.

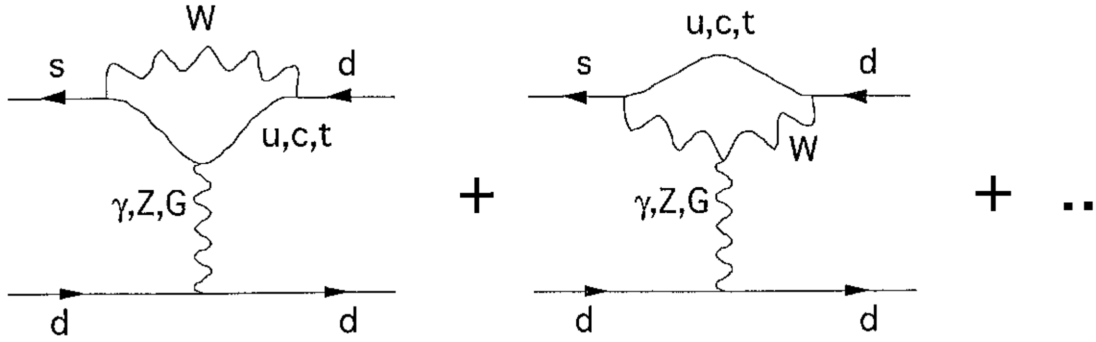

Fig. 1.2: Penguin Diagrams contributing to direct CP violation.

Experimental Evidence for Direct CP Violation

The double ratio (1.40) was recently measured by two experiments, NA31 at CERN and E731 at Fermilab. Their final results are

$$\mathrm{Re}\left(\frac{\varepsilon'}{\varepsilon}\right) = (2.3 \pm 0.65) \times 10^{-3} \quad \text{[NA31/93]} \tag{1.59}$$

$$\mathrm{Re}\left(\frac{\varepsilon'}{\varepsilon}\right) = \left(0.74 \pm 0.52_{(stat.)} \pm 0.29_{(syst.)}\right) \times 10^{-3} \quad \text{[E731/93]} \tag{1.60}$$

The NA31 result shows a non-vanishing result for ε', whereas the E731 collaboration quotes a result still consistent with zero. Unfortunately, these are the only two experiments which have so far reached this level of accuracy. Both groups are working on an improved test of direct CP violation. The experiment at CERN will be NA48 and the experiment at Fermilab will be E832, a part of the KTeV program [Ari92]. Both experiments want to reduce the error to 2×10^{-4}.

Chapter 2: The CP Violation Experiment NA48

The NA48 experiment will measure the ratio ε'/ε by counting the rates of the four decays in the double ratio (1.43). The goal is to achieve an accuracy of 2×10^{-4} on the double ratio [NA48/90]. This will decrease the measurement error by a factor of ten compared to the error of the experiments NA31 and E731.

The NA48 experiment will exploit the fact that the effects of detection efficiencies cancel, if the double ratio is evaluated independently for different kaon momenta and decay positions and if the K_L and K_S beams coincide in space at the position of the detector. The main contributions to the error of the NA31 experiment and their countermeasures in the NA48 experiment are listed below in order of their importance.

- The statistical error of the NA31 experiment was dominated by the number of $K_L \to 2\pi^0$ events, which was approximately 3×10^5 events for three years data taking time. To reach the required statistical error, the event rate of the NA48 experiment will be ten times bigger, thus increasing the expected total number of $K_L \to 2\pi^0$ events to 4.5×10^6. The high intensity of the beam that is necessary to obtain the required rate of 10^{12} particles per pulse and the high hadron and muon fluxes connected with it, forces the installation of the experiment in an underground area sufficiently large to house beamline and detector. Such a place was found at the North Area High Intensity Facility in the ECN3 hall at the K12 beamline of the CERN SPS.

- The effect of differences in the energy scales reconstructed from charged and neutral kaon decays will be reduced by a suitable choice of kaon spectra. In addition a weighting procedure will be used. Each K_L decay will be weighted by a factor $e^{-z/\lambda(p)}$ with $\lambda(p)=\frac{p}{m}\frac{c\tau_S}{1-\tau_S/\tau_L}$ according to its measured vertex position in the z-coordinate. With this procedure the distributions of the longitudinal vertex positions of K_S and weighted K_L are made similar, such that corrections for variations of the acceptance for different vertex positions cancel between K_S and K_L. This method will be used at the expense of an increase of the statistical error of 15%.

- The background to $K_L \to 2\pi^0$ from $K_L \to 3\pi^0$ decays with only four detected photons will be measured by anticounters, which have to detect pions that are emitted under a large angle, and the photon calorimeter. To accomplish this task an energy resolution superior to the NA31 lead/liquid argon calorimeter and good 2γ-separation is required for the calorimeter.

- The background to $K_L \to \pi^+\pi^-$ from three body decays like $K_L \to \pi e \nu\ (K_{e3})$ and $K_L \to \pi^+\pi^-\pi^0$ will be decreased by a magnetic spectrometer.

- To reduce differential effects of accidental activity for K_S and K_L decays the four decay channels in the double ratio (1.43) will be studied simultaneously. The neutral kaons will be produced in two nearly collinear beams. A K_L beam will be produced at a target located 220 m upstream from the spectrometer and a K_S beam will be produced at a target located 90 m from the spectrometer.

An overview of the setup of the NA48 experiment is given in figure 2.1. The different parts of the experiment will be described in the following sections.

Beam and Decay Region

The Kaon Beams

The two kaon beams are obtained from the same primary proton beam of 450 GeV and an intensity of 1.5×10^{12} particles per pulse extracted from the CERN SPS. It hits the first target under a production angle of 2.4 mrad, producing a neutral kaon beam. Behind the first target a bent channeling crystal deviates a fraction of the primary proton beam, about 3×10^{7} particles per pulse. The main part of the primary proton beam continues undeviated and hits a beam dump. The extracted proton beam is transported through a set of sweeping magnets and collimators to the second target. There the second kaon beam is produced under a production angle of 4.2 mrad. The first target is far enough from the fiducial decay region that only K_L survive, whereas K_S decays dominate the decays from the second beam in the fiducial region.

The use of a bent channeling crystal to direct a fraction of the proton beam to the second target was chosen for the following reasons.

- The extracted proton beam is deflected in a direction opposite to the preceding magnet without canceling its sweeping action on other charged particles.

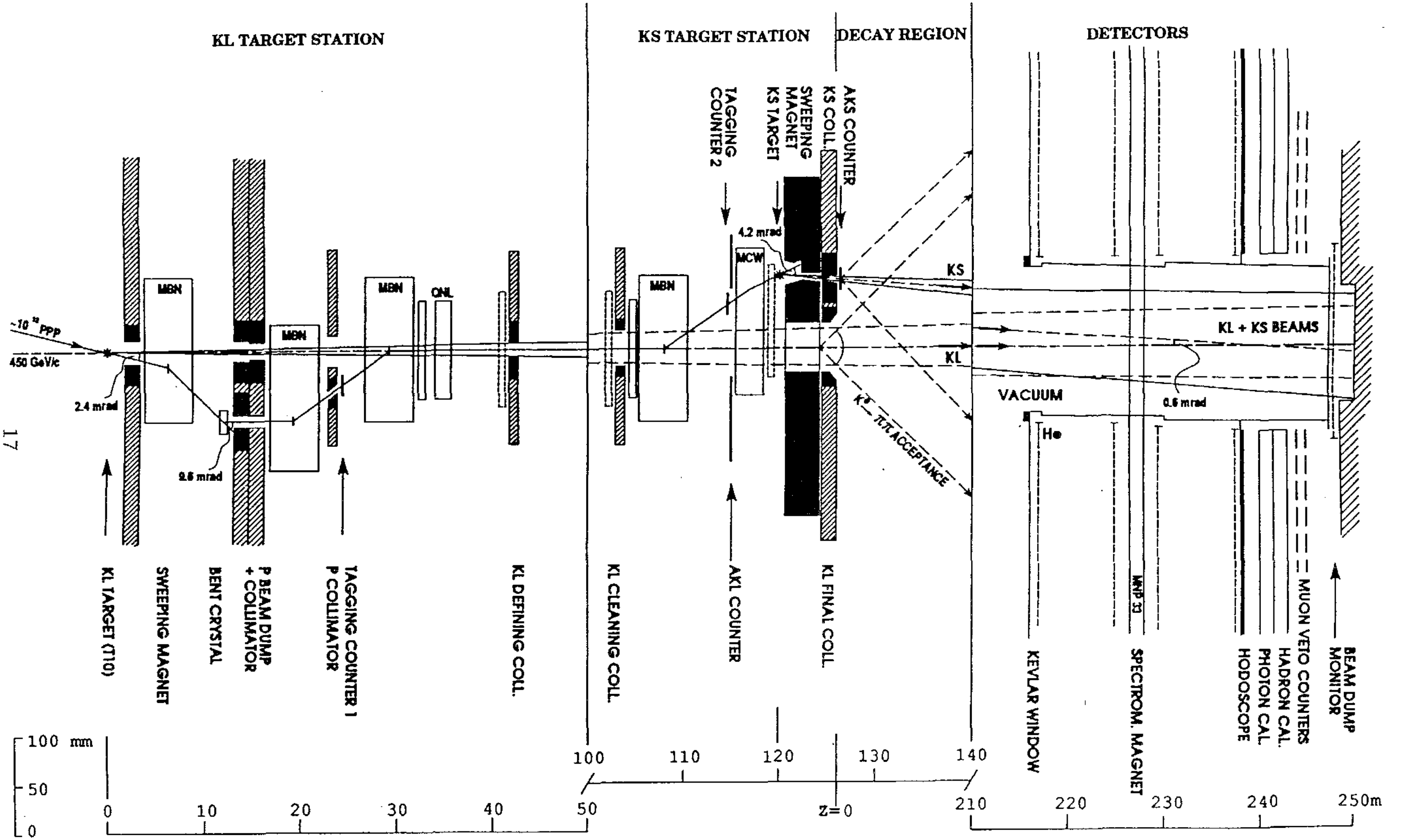

Fig. 2.1: The layout of the NA48 experiment. Note the different vertical and horizontal scale.

- The proton intensity is attenuated to give a suitable number of $K_S \to 2\pi$ decays in comparison to the number of $K_L \to 2\pi$ decays.
- A small emittance beam, suitable for transport to the K_S target, is selected.

The Tagging Counter Systems

Each decay will be assigned to a specific kind of beam by a tagging counter. This counter is placed in the path of the deflected part of the primary proton beam before it hits the second target. Decays in the K_S beam are identified by requiring a proton passing the tagging counter together with an event in the detector after a period that corresponds to the time of flight between the tagging counter and the detector. The time of the event in the detector will be given by a scintillator hodoscope behind the spectrometer for a charged event. For the neutral decay mode two possible methods are under study. The time will be given either by a scintillator layer in the photon calorimeter or by the time information of the calorimeter itself. The decision depends on the time resolution that can be achieved by the photon calorimeter.

The deviated proton beam gives an average rate of about 10 MHz in the tagging counter. It is expected that the time resolution between the tagging counter and the hodoscope will be 0.5 ns. Good time resolution is necessary to keep the time window which is allowed for a K_S decay sufficiently short. A time window of $\pm 5\sigma$ or 5 ns will give 5% K_L misidentified as K_S at a rate of 10 MHz. The effects of tagging errors caused by the length of the time window ($K_L \to K_S$) and inefficiencies in the counter system ($K_S \to K_L$), on the value of the double ratio are understood and can be corrected [Note92/4]. The correction factors can either be obtained from decays in the first part of the decay region, where the beams do not fully overlap, or from runs, in which one beam is switched off.

The high rate in the tagging counter cannot be handled by a single counter. Therefore, the profile of the beam will be covered by two ladders of 11 scintillator foils (NE110), each being 200 μm thick. Adjacent scintillators will overlap by 50 μm. The two ladders are perpendicular to each other to minimize the double pulse probability. The light from the large surfaces ($30 \times 5\ \mathrm{mm}^2$) of the scintillator foils will be collected in an air light guide and viewed by Hammamatsu R2076 photomultipliers, 1 cm below the scintillators. The opposite side of the scintillator foils will be covered with a mirror.

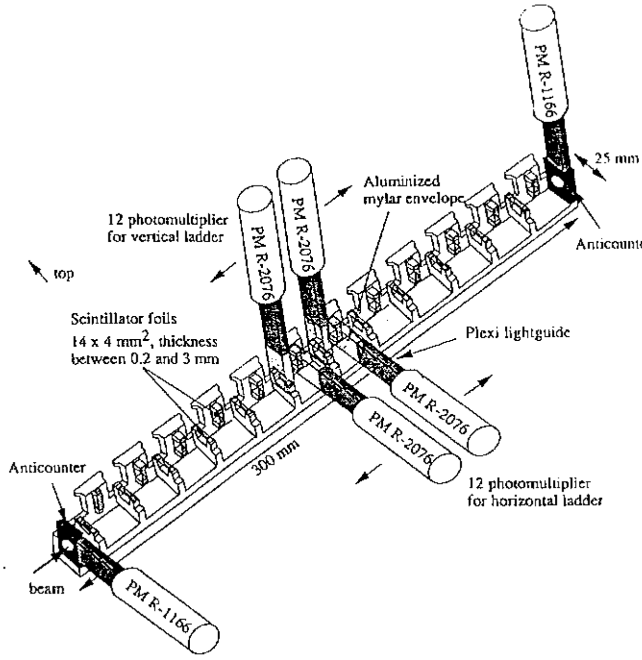

Fig. 2.2: The tagging counter.

The main reason for inefficiencies in the tagging counter will be the loss of tagged protons due to the deadtime. Thus, flash analog to digital converters (FADCs) with a sampling rate of 450 Msamples/s will be used. A deadtime of less than 2 ns and a double pulse resolution better than 5 ns will be achieved.

The Decay Region

The fiducial decay region begins after the final K_S collimator. Only events coming from a vertex within a region of 12 m corresponding to $2\tau_S$ are accepted. The fiducial decay region is contained in the upstream end of an 88 m long vacuum tank with a diameter of 1.9 m in the first and 2.4 m in the second part. The volume of 330 m^3 is kept at a pressure of less than 10^{-3} bar. The tank is terminated by a Kevlar window of 0.8 mm thickness. Locally the overlap of Kevlar slices increases the thickness to 1.1 mm. In the center, the window has an opening for a 14.8 cm wide beam pipe that allows the kaon beams to cross all the detector components in vacuum until they reach a beam dump at the end of the experiment.

To suppress the $K_L \rightarrow 3\pi^0$ background, seven ring anticounters are distributed over the length of the vacuum tank and the following helium tank. These counters contain two layers of scintillators, preceded and separated by a 5 cm thick iron layer. Additional muon veto counters, used to suppress $K_{\mu 3}$ events, will be located behind the calorimeters. These veto counters consist of four large scintillator planes separated by 0.8 m of iron.

The Detection of the Charged Decay

The momenta of charged particles will be measured in a spectrometer consisting of a large aperture dipole magnet and four drift chambers, two in front of and two behind the magnet. The distance between the two drift chambers of one pair will be 10 m. The inner chambers will be 2.5 m away from the magnet. This is far enough, so that the resolution is not worsened by the fringe field of the magnet. The spectrometer will be installed in a helium tank behind the Kevlar window.

The momentum resolution of the spectrometer is limited by multiple scattering to $\Delta p/p = 0.6\%$. This is matched to a position reconstruction accuracy of 100 μm of the chambers for the average pion momentum of 60 GeV/c.

The magnet has a bending power equivalent to a change of the transverse momentum of 200 MeV/c. The non-uniformity of the field integral is expected to be less than 10%.

The spectrometer plays a crucial role for the trigger of the experiment. It has to reject decays downstream of the fiducial decay region, as well as K_{e3} and $K \rightarrow \pi^+\pi^-\pi^0$ decays, which dominate the branching ratio. Thus, it is necessary to reach sufficient on-line resolution and tracking efficiency to enable a fast vertex reconstruction and the calculation of the two-particle invariant mass. This can be achieved by measuring the drift times with a 100 MHz clock, equivalent to 500 μm time bins. In addition, it is necessary to keep variations of the integrated magnetic field below 10%. Inefficiencies are avoided by small drift spaces of 5 mm. Each chamber consists of four layers with two wire chamber planes. Two layers are oriented horizontally (x) and vertically (y) and the two remaining layers are twisted by 45° with respect to the first ones (u and v).

Events with a two-particle invariant mass below 450 MeV or with a reconstructed transverse kaon momentum above 60 MeV/c will be rejected. This cut rejects all $K \rightarrow \pi^+\pi^-\pi^0$ decays and 90% of the K_{e3} decays without loss of $K \rightarrow 2\pi$ events. The ratio of accepted $K \rightarrow 2\pi$ to K_{e3} events will improve from 1 : 135 to 1 : 20. Tighter off-line cuts, with the two-particle invariant mass in a range of 10 MeV around the kaon mass and requiring less than 15 GeV/c transverse momentum, will give a contamination with K_{e3} events of about 40%. Comparison of the energy in the calorimeter with the momentum in the spectrometer will decrease this level further by a factor of 500 to about 0.1%.

Additional rejection with reduced deadtime for K_{e3} and $K_{\mu 3}$ decays will be provided by a hadron calorimeter located behind the photon calorimeter by requiring energy thresholds for charged decays. In addition, the hadron calorimeter will improve the particle identification capability of the photon calorimeter and will be used in the search for rare kaon decays like $K \to \mu\mu\gamma$. For this the NA31 hadron calorimeter with a renewed scintillator system will be used. An energy resolution similar to the resolution in the NA31 experiment ($\sigma(E)/E = 65\%/\sqrt{E}$) is expected.

The Detection of the Neutral Decay

Decays of the kaon into neutral pions will be identified through the photon pairs from the decaying pions in a photon calorimeter [Buc92]. The photons have an energy range of 2 to 200 GeV and an average energy of 25 GeV. The photon calorimeter has to fulfill the following demands.

- The multi-photon event rate will be 1 MHz.
- The energy resolution is required to be substantially better than the energy resolution of the NA31 lead/liquid argon calorimeter, which was $\frac{\sigma(E)}{E} = \frac{7.5\%}{E[GeV]} \oplus 0.5\% \oplus \frac{100 MeV}{E}$ [NA31/88].
- The space resolution has to be better than 1 mm and two photons separated by more than 4 cm have to be distinguished.
- The photon calorimeter has to provide a neutral event trigger.
- The time resolution should be sufficient to cope with the resolution of the tagging counter (~1 ns).

Structure and Readout of the Liquid Krypton Calorimeter

To meet these requirements a homogenous liquid krypton calorimeter with charge readout will be built. Some of the properties of liquid krypton are listed in table 2.1.

Capacitance and resistance of the readout electrodes must be kept small to achieve the necessary speed. Therefore the calorimeter will be divided into "towers" parallel to the beam. These towers consist of two parallel plate capacitors with a common anode in the center of the tower and two cathodes at the left and right edge of the towers.

	Liquid Argon	Liquid Krypton
Z	18	36
A	40.0	83.8
Density ρ [g/cm^3]	1.40	2.41
Radiation length X_0 [cm]	14.0	4.72
Molière radius R_M [cm]	7.2	4.7
Nuclear interaction length λ [cm]	84	60
Ionization energy [eV/pair]	23.3	20.5
Electron drift velocity [mm/μs]		
at 1 kV/cm	2	3
at 5 kV/cm	3.5	4
Critical energy E_c [MeV]	41.7	21.5
Dielectric constant ε_r	1.54	1.72
T (boiling point) [K] , at 1 bar	87.3	119.8
T (triple point) [K]	83.8	116.0
Radioactivity		^{85}Kr, β^-, E_{max} = 0.7 MeV 400 Bq/cm^3

Tab. 2.1: Properties of liquid argon and liquid krypton [Buc92].

The amplifiers are connected to the anodes and located directly at the downstream end of the towers, still in liquid krypton, to avoid the capacitances and inductances of connecting cables. The towers are 125 cm or 27 radiation lengths long, which is sufficient to keep the longitudinal leakage small.

There are two reasons for the choice of a longitudinal readout structure, over the alternative commonly used transverse segmentation.

- The transverse structure is more than four times as susceptible to accidental events as the longitudinal structure. 0.5% loss of events is expected in the case of a longitudinal and 2.5% loss in a transverse structure.

- A good time resolution will be difficult to achieve in a transverse structure, as the charge has to be summed up from the signal in more towers. As the signal for each tower will be lower additional noise problems will arise.

The required space resolution defines the lateral size of the towers. A cross-section of 2×2 cm^2 was chosen.

The lateral dimensions of an electromagnetic shower in liquid krypton can be illustrated by the result of an EGS (Electron Gamma Shower) Monte Carlo simulation (fig. 2.3). The small core of the shower is the reason for a highly non-uniform ionization in the calorimeter.

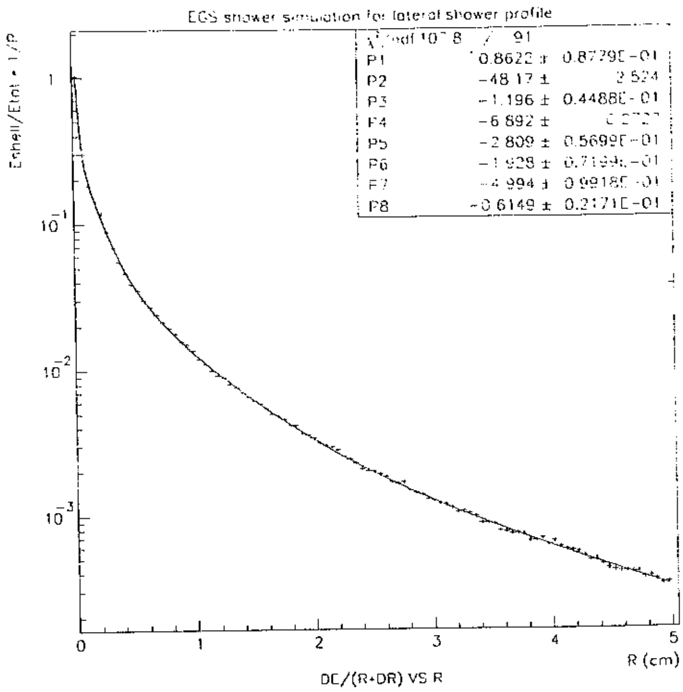

Fig. 2.3: Radial charge density from an electromagnetic shower as obtained from an EGS Monte Carlo simulation [Schi].

To decrease non-uniformity effects in the response of the calorimeter due to the non-uniform ionization in the gap between the electrodes, the towers will have a zig-zag shape with a small angle (50 mrad) with respect to the beam axis.

The readout of the liquid krypton calorimeter will use the initial current readout method with fast pulse shaping. This technique was already used in the test beams of the liquid krypton calorimeter prototype and will be explained in detail in chapter 4. The signal from the shapers will be recorded in a 40 MHz FADC system. To keep the cost of the electronics reasonable, this FADC system will use one 10 bit ADC (analog to digital converter) chip per channel. To increase the dynamic range of the system, the gain of the FADC input preamplifier will vary in three steps depending on the height of the input signal. A similar principle was used in the prototype tests in 1992. The properties of such a FADC system will be discussed in chapter 4.

Prototype Tests

A prototype which was slightly different in construction from the prototype used for the runs in 1992, was tested in 1991 [Buc92]. It consisted of 184 towers. A detailed description of the prototype and the test beam results is given in [NA48/91] and [NA48/92]. This prototype test showed that the concept of the longitudinal tower structure was feasible. Still many problems appeared. The space and the time resolution were sufficient, whereas the energy resolution was much worse than the prediction of an EGS Monte Carlo simulation. The sampling term of the prototype was $4.4\% / \sqrt{E}$ for events, where the incoming electron had hit the calorimeter at a position that was at least 3 mm away from the electrodes. The result for the sampling term from the Monte Carlo simulation was $1.8\% / \sqrt{E}$ without the selection of the impact point [NA48/90/2]. This simulation did not consider the effects of the collection of the ionization charge in the calorimeter and the readout.

In addition, technical problems which were partly the reason for the insufficient energy resolution appeared. Due to impurities of the liquid krypton, short electron lifetimes (few 100 ns) were observed. These impurities (as well as high voltage and noise problems) resulted in a bad signal-to-noise ratio. Pickup effects in the calibration system led to miscalibrations of the calorimeter.

It was the goal of the beam tests during 1992 to solve these problems. The improved results were to be compared with the results from the Monte Carlo simulation and possible remaining discrepancies were to be understood. These tests will be discussed in the chapters 4 and 5.

Status of the NA48 Experiment in Summer 1993

The following parts of the NA48 experiment are already installed or shortly before installation in the final experimental area.

- The complete vacuum tank and the helium tank without the Kevlar window is installed.
- The magnet is in its place. For technical reasons the magnetic field measurements are not completed.
- The tagging counter, the hodoscope and the ring anticounters are in place.
- One plane of the drift chambers will be operational in fall 1993.

- The hadron calorimeter with the new scintillator system is installed.

A first test in fall 1993 will be used to test these parts of the experiment and the setup of the beam. A second beam test in fall 1993 is dedicated to the test of a new prototype for the liquid krypton calorimeter. The main topic is the investigation of the construction and the performance of a zig-zag-shaped calorimeter.

Chapter 3: Calorimetry in High Energy Physics

The Principles of Calorimetry in High Energy Physics

A high energy physics calorimeter is a block of matter, which forces an incoming particle to disperse into a cascade (shower) of secondary particles with rapidly decreasing energy. After a sufficiently long time ($\sim 100\ \mu s$) the energy of the particle is converted into heat. Actual calorimeters in high energy physics measure the energy of intermediate states, which can be ionization charge, scintillation light or Cherenkov radiation[3]. The goal is to detect a constant fraction of the primary energy of particles of different kind, different energy and different position and direction. Due to the large discrete number of secondary particles in the shower the behavior of calorimeters is dominated by statistical processes.

Apart from their energy measuring capability, calorimeters have several properties, which make them a powerful detection tool.

- Calorimeters are sensitive to neutral as well as to charged particles. For charged particles only calorimeters can provide the energy information if the momentum is too high to allow the exact measurement of the sagitta of the particles track in a magnetic spectrometer.

- Particle identification is possible because of the characteristic shapes of the showers for different kinds of particles.

- Due to the statistical nature of the measurement process the relative energy resolution improves for higher energies.

- The calorimeter dimensions necessary for the containment of the shower increase only logarithmically with the energy of the particle.

- Calorimeters do not need a magnetic field for the energy measurement.

[3]The first calorimeters in particle physics measured indeed the heat, which was produced in the calorimeter. See for example [Mei30] and [Ort30].

- Calorimeters can be very fast particle detectors, which allows their use in high rate experiments. The fast calorimeter information can be used at early trigger levels.

Depending on the kind of interaction that dominates the production of secondary particles, the showers can be divided into electromagnetic showers and hadronic showers. As the NA48 liquid krypton calorimeter has to measure the energy of photons, the properties of electromagnetic calorimeters will be discussed in this chapter. Detailed reviews about hadronic calorimetry can be found in [Fab82], [Fab89], [Wig87], [Wig91].

Electromagnetic Showers

Development of Electromagnetic Showers

Photons interact with matter through the photoelectric effect, Compton scattering and, dominating at higher energies, pair production (fig. 3.1). Thus, the first process induced by a high energy photon entering a block of matter will be the production of an electron-positron pair.

Electrons and positrons in matter either emit bremsstrahlung photons or produce ionization charge. The first process is dominant for particle energies higher than 100 MeV, whereas for lower energies, the energy loss due to ionization dominates (fig. 3.1). The critical energy ε_c is the energy, at which the energy losses by these two processes are equal. This energy can be approximated by [Ama81]

$$\varepsilon_c \cong \frac{550}{Z_{mat}}[MeV] \quad \left(\frac{\Delta\varepsilon_c}{\varepsilon_c} \leq \pm 10\%, \text{ for } 13 \leq Z_{mat} \leq 92\right). \tag{3.1}$$

If a high energy electron or photon hits the calorimeter a chain of pair production and bremsstahlung emission develops, which lasts until the critical energy is reached. At this point the particle multiplication stops and the maximum number of secondary particles, also called the shower maximum, is reached.

Dimensions of Electromagnetic Showers

A characteristic dimension for the interaction between electrons and matter is the radiation length X_0. One radiation length is the distance after which the energy of the electron is reduced by the factor 1/e.

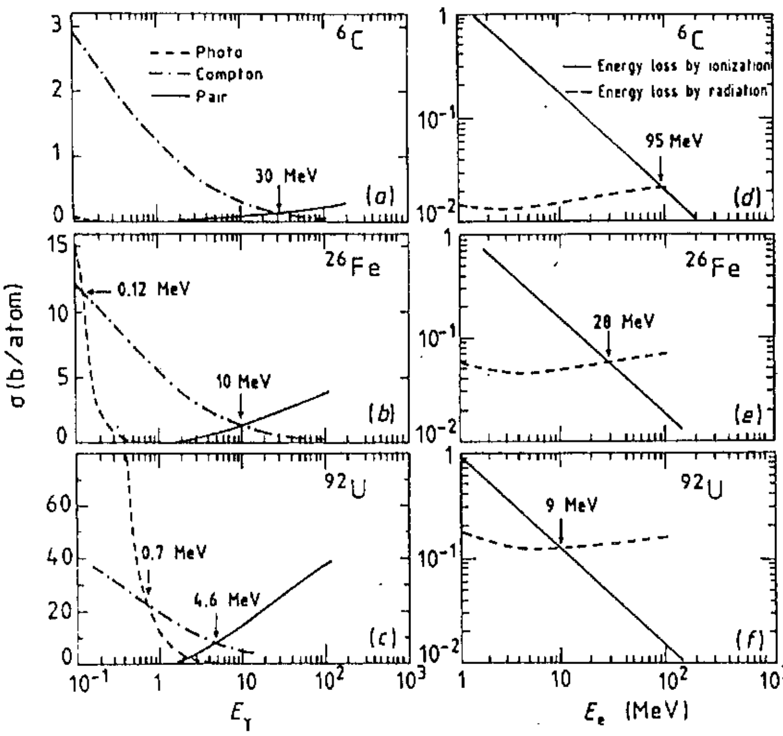

Fig. 3.1: Photon cross section and energy loss of electrons and positrons in different materials [Fab89].

$$\frac{dE}{E} = -\underbrace{n_A \sigma_{brems}}_{1/X_0} dx \tag{3.2}$$

With σ_{brems} from QED calculations [Bet34], the radiation length follows for high energies as

$$X_0^{-1} \cong \sigma_0 n_A \left[4 \ln\left(183 Z_{mat}^{-1/3}\right) + \frac{2}{9} \right] \quad \text{with} \quad \sigma_0 = \frac{Z_{mat}^{2} \alpha^3}{m^2}, \tag{3.3}$$

which is independent of the energy. Since the bremsstrahlung is dominated by the interaction with the nuclei[4] it is proportional to Z_{mat}^{2} (fig. 3.2).

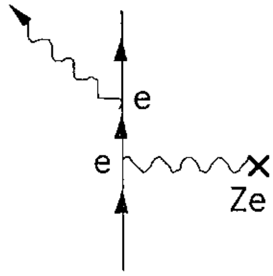

Fig. 3.2: Emission of Bremsstrahlung.

[4]The dependence on Z_{mat} is different for the energy loss due to ionization as described by the Bethe-Bloch formula. There it is proportional to Z_{mat} as it is derived from an interaction with the shell electrons.

As an approximation [Ama81]

$$X_0\left[\frac{g}{cm^2}\right] \cong \frac{180A}{Z_{mat}^{\ 2}} \quad \left(\frac{\Delta X_0}{X_0} \le \pm 20\%, \text{ for } 13 \le Z_{mat} \le 92\right). \tag{3.4}$$

can be used.

As the pair production in QED is very similar to the bremsstrahlung process this emission can be described by the radiation length as well. The average distance that a very high energy photon propagates before converting into an electron-positron pair is $\frac{9}{7}X_0$.

The longitudinal development of the electromagnetic shower is almost independent of the material if it is scaled with the radiation length (fig. 3.3). Approximately 25 radiation lengths are necessary to contain 99% of the shower. The larger distance to the shower maximum and the longer tail of the shower for materials with higher Z is because the critical energy is lower and therefore particle multiplication continues to lower energies.

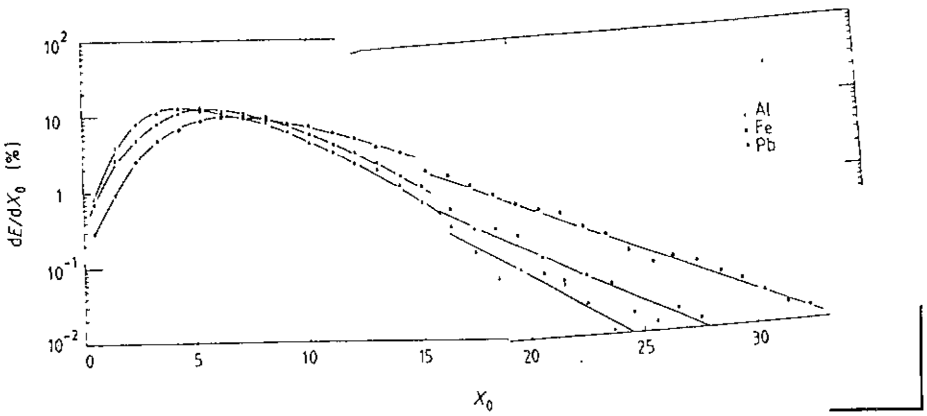

Fig. 3.3: Longitudinal development of the showers from 10 GeV electrons in different materials [Fab89].

In an approximation, where a constant energy loss of ε_c per radiation length is assumed, the distance from the calorimeter front to the center of gravity of the deposited energy is given by [Ros41]

$$t_{\max}[X_0] = 1.01 \cdot \ln\frac{E}{\varepsilon_c} - \alpha \quad \text{with } \alpha \cong 0.4 \text{ for } e^+, e^- \text{ and } \alpha \cong 1.2 \text{ for photons.} \tag{3.5}$$

The depth of the electromagnetic shower increases logarithmically with the energy of the incoming particle (fig. 3.4).

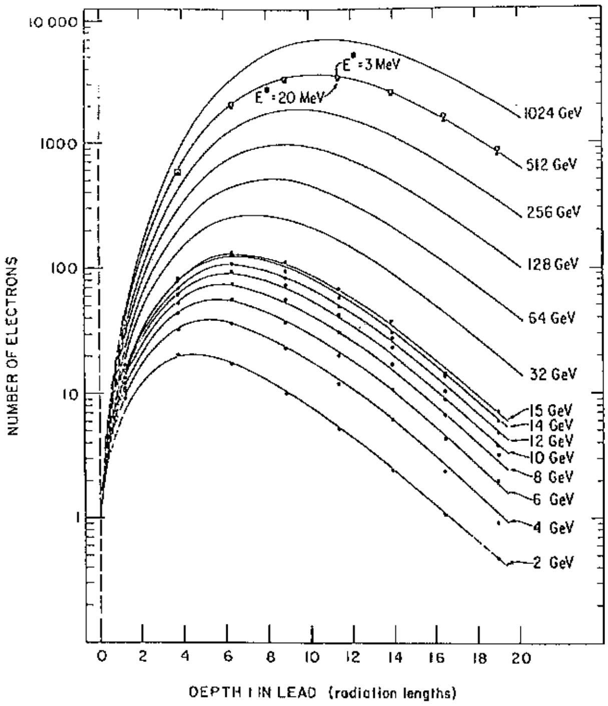

Fig. 3.4: Longitudinal dimensions of electromagnetic showers for different particle energies [Mül72].

The lateral development of an electromagnetic shower is caused by two effects. A narrow core is formed by multiple scattering of low energy electrons in the calorimeter material. This core is surrounded by a halo of bremsstrahlung photons. The narrow central core decreases beyond the shower maximum as the two processes are of different importance in different longitudinal sections of the shower (fig. 3.5).

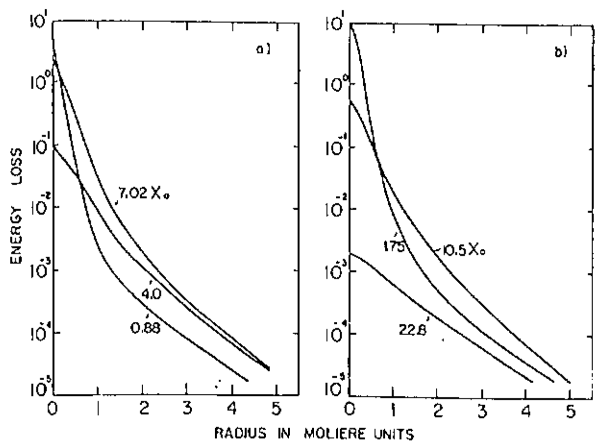

Fig. 3.5: The lateral distribution of the energy deposition by an electromagnetic shower with 1 GeV for various depths in lead. Results of an EGS4 simulation (Figures are from [Ama81]; original work is done by [Yud69]).

A suitable measure for the lateral dimension of the electromagnetic shower is the Molière radius. About 95% of the shower are contained in a cylinder with a radius of two Molière radii. An approximation for the Molière radius is given by [Ama81]

$$\rho_M\left[\frac{g}{cm^2}\right]=\frac{7A_{mat}}{Z_{mat}}\quad\left(\frac{\Delta\rho_M}{\rho_M}\leq\pm 10\%,\ \text{for } 13\leq Z_{mat}\leq 92\right). \tag{3.6}$$

The lateral spread increases further if the shower crosses regions of smaller absorption ability. Therefore the lateral dimension has to be scaled by a density factor even when it is given in units of the Molière radius.

Particles that produce an electromagnetic shower in the calorimeter can easily be distinguished from other particles. The showers from particles with the same energy that interact hadronically - like charged pions - are much deeper and broader. Muons do not induce showers in a calorimeter, as the cross-section for bremsstrahlung emission is proportional to $1/m^2$ (3.3). Therefore they create a single track with an energy loss of about $2\frac{MeVcm^2}{g}$ due to ionization along the path of the particle (fig. 3.6).

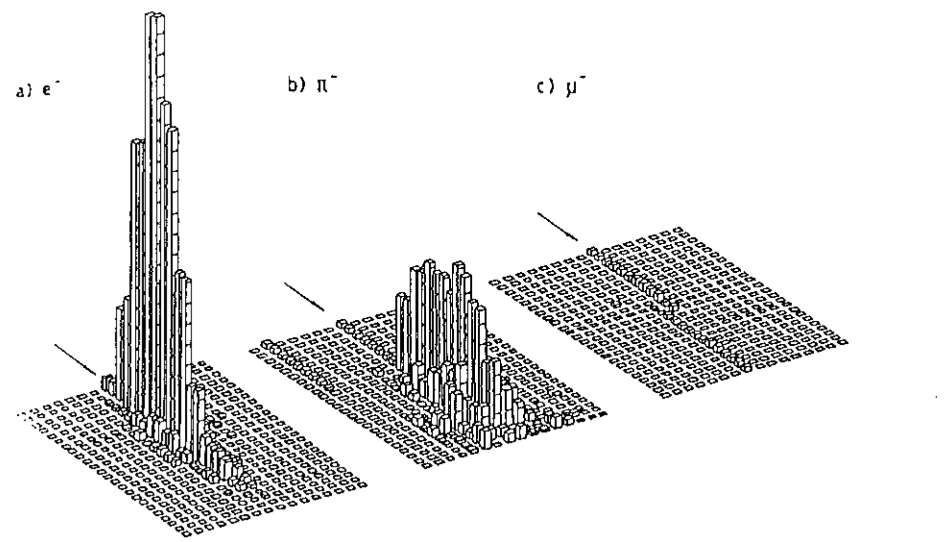

Fig. 3.6: Different shower shapes of electromagnetic showers (left) and hadronic showers (middle) and a muon track (right) in the same calorimeter [MARS83].

Construction of Electromagnetic Calorimeters

Homogenous Calorimeters and Sampling Calorimeters

A simple calorimeter construction principle is to build the whole calorimeter out of one material that forces the development of the shower and provides a useful signal.

Very often crystals like NaI(Tl), lead glass, CsI(Tl), Bismuth Germanium Oxide (BGO) or CsF_3 are used. They have a short radiation length (typically a few centimeters) and emit either scintillation or Cherenkov light. The advantage of homogenous calorimeters is their superior energy resolution.

To reduce the detector length one can build a calorimeter that consists of layers of a passive absorber material with a short radiation length, in which the shower mainly develops, alternated by active detector layers. Such devices are called sampling calorimeters. Sampling calorimeters can be less deep than homogenous calorimeters and there is more freedom in the choice of the readout method. The absorber material can be optimized for particular tasks, for example for electron-hadron discrimination.

Detection and Readout

As for the construction type there exist different choices for the detection method in calorimeters. Light emission is measured with photomultipliers or photodiodes. Homogenous calorimeters are usually segmented in towers of light-emitting crystals pointing to the vertex with photomultipliers or photodiodes attached to their ends [L3/88]. In sampling calorimeters, scintillator layers can be inserted between the absorber material. The light is collected with light guides. Often wavelength shifters are used to shift the frequency of the signal to a region, where the light guide has its optimum transmission capability [Gar60]. The light enters the wavelength shifter through an air gap where it is absorbed and reemitted with a longer wavelength.

Electric charge from ionization can be measured in proportional or ionization chambers. Gas-filled proportional chambers are only used in sampling calorimeters as fluctuations in the gas gain give an additional contribution to the deterioration of the resolution. In these devices layers of proportional chambers are alternated with the absorber material. More often the ionization chamber setup is used. In ionization chambers the charge is collected in capacitors with large electrode plates, which can be the plates of the absorber material in the calorimeter. Ionization chambers are either filled with liquid noble gases like argon [NA31/88], [H1/88], [D0/88], [RD3/92] and more recently krypton and xenon or with warm liquids (TMP, TMS, HEDS) [UA1/91]. It is possible to use the drift time information of the ionization charge [DELPHI85], [DELPHI87].

Each construction type has its advantages and disadvantages. The use of crystals with light readout offers the best energy resolution in homogenous calorimeters. However, mechanical stability, radiation hardness, problems with hygroscopic crystals and the price cause difficulties. Stable calibration is difficult because of the non-uniformities and the non-linearities in such devices. Light readout in sampling calorimeters allows for the easy construction of large devices at the cost of problems with the calibration and aging of scintillators and light guides. Light guides and photomultipliers introduce dead space in the detector. Ionization chambers have a good uniformity and linearity and negligible radiation damage but require a high purity of the liquid detection media, especially for warm liquids. The cryostats necessary for liquid noble gases are additional dead space in the detector.

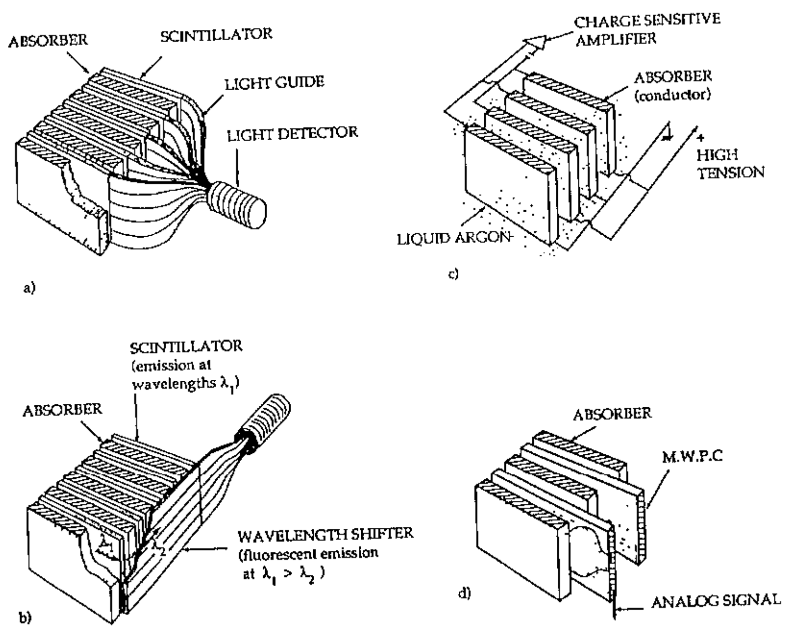

Fig. 3.7: Construction Principles of Calorimeters [Fab92].

Electromagnetic Calorimeters as Particle detectors

Energy Measurement

The total track length of all secondary particles in the calorimeter is proportional to the energy of the incoming particle

$$S_{tot}[X_0] \propto \frac{E}{\varepsilon_c}. \tag{3.7}$$

A signal proportional to the energy of the incoming particle is achieved, if the energy loss per unit track length is constant. For the ionization charge, this is fulfilled to very good approximation, as the secondary particles have an energy that is well in the relativistic plateau of the Bethe-Bloch formula. In real calorimeters the measurable track length S_{meas} depends on the minimum detectable energy η and is smaller than the total track length. However, the measurable track length is still proportional to the energy of the incoming particle [Ama81]

$$S_{meas}[X_0] \propto \mathrm{F}(\eta)\frac{E}{\varepsilon_c}. \tag{3.8}$$

Statistical fluctuations of the measurable track length give the intrinsic limitation to the energy resolution. The estimate

$$\frac{\sigma(E)}{E} = \frac{\Delta N}{N} = \frac{\sqrt{N}}{N} = \frac{1}{\sqrt{N}} \propto \frac{1}{\sqrt{E}} \tag{3.9}$$

gives the functional dependence of the energy resolution on the energy. In sampling calorimeters the energy resolution is dominated by fluctuations of the energy deposited in the detector layers. In a sampling calorimeter consisting of cells of one absorber and one detector layer with a combined thickness d, particles pass the active layers

$$N = \frac{S_{tot}}{d} = \frac{E}{\Delta E} \tag{3.10}$$

times, if ΔE is the energy loss in one cell. The energy resolution of sampling calorimeters becomes

$$\frac{\sigma(E)}{E} = \frac{\sqrt{N}}{N} = \sqrt{\frac{\Delta E}{E}} = 0.032\sqrt{\frac{\Delta E[MeV]}{E[GeV]}}. \tag{3.11}$$

Additional contributions to the energy resolution of real calorimeters can be included by

$$\frac{\sigma(E)}{E} = \frac{\sigma_f}{\sqrt{E}} \oplus \sigma_{sys} \oplus \frac{\sigma_{noise}}{E} \tag{3.12}$$

where σ_f describes all effects of statistical fluctuations of the energy that is seen in the calorimeter. This term is often called sampling term, as it gives the main contribution to the energy resolution of sampling calorimeters. The second term contains the effects of non-uniformities and miscalibrations which are independent of fluctuations, but depend for example on the impact point of the particle. Pile-up effects also contribute to this term. The last parameter describes the effect of noise, which is independent of the energy of the incoming particle.

It is important to choose the size of the calorimeter which is instrumented comparable to the size of the showers. Leakage - longitudinal or lateral - increases mainly the sampling term, whereas the energy measurement of showers which are small compared to the calorimeter leads to an unnecessarily low signal-to-noise ratio. Longitudinal shower leakage affects the energy resolution more than lateral leakage (fig. 3.8). Full containment of the shower has to be achieved for all impact points in the calorimeter, even at the edge of the fiducial volume of the detector.

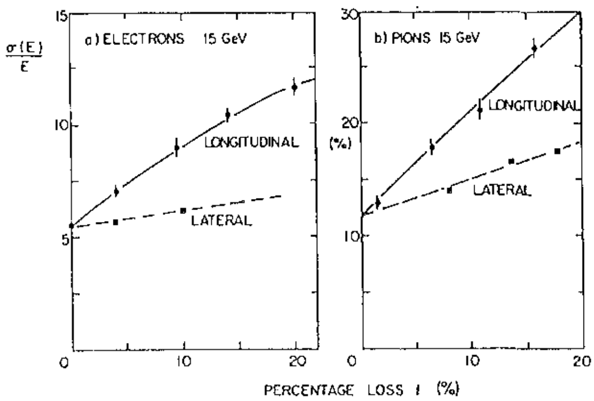

Fig. 3.8: The effects of longitudinal and lateral shower leakage on the energy resolution [Ama81].

Design Criteria for Electromagnetic Calorimeters

Although a good energy resolution is the main task of a calorimeter, there are further points, which have to be considered in the design of electromagnetic calorimeters.

- High counting rates and the use of calorimeter data for fast trigger signals have major impacts on the construction of the calorimeter electronics.
- The requirements for the reconstruction of the position and the direction of the incoming particle influence the choice of the construction type and the granularity of the calorimeter.
- The size of the calorimeter and the spatial angle, which has to be covered, can make particular designs mechanically and financially impracticable.
- In large detector systems, especially in collider experiments, calorimeters have to be integrated into other detector components. They have to work in magnetic fields. Sufficient space is necessary for cryostats, electronics, photomultipliers etc..
- A limiting factor is the cost of the calorimeter. The cost for the calorimeter and for the readout electronics have to be considered.

Ionization Chambers and Their Readout

Signal Formation in Ionization Chambers

Ionization chambers consist of large parallel plate capacitors with high voltage between the plates [Wil74]. The signal on the electrodes is induced by the motion of the drifting charge carriers, negative electrons and positive ions, which were produced in the gap of the capacitor. The shape of the signal can be calculated using the reciprocity or the Gauss theorem [Rad88/1]. It uses the fact that the partial capacitance between any two electrodes is independent of the direction in which it is measured.

$$\frac{Q_1}{V_2} = \frac{Q_2}{V_1} = C_{12} \ , \tag{3.13}$$

where a voltage V_1 applied on electrode 1 induces a charge Q_2 on electrode 2, and vice versa. The drifting charge carrier can be described by an infinitesimally small electrode. The induced current on the electrode becomes

$$I_1 = \frac{d\left(\dfrac{q_{cc}V_{cc}}{V_1}\right)}{dt} = q_{cc}\underbrace{\mathrm{grad}\left(\frac{V_{cc}}{V_1}\right)}_{-E_w}\frac{d\bar{\mathbf{r}}_{cc}}{dt} \tag{3.14}$$

with the virtual weighting field E_w. It can be calculated supposing that electrode 1 is at unity potential, whereas all other electrodes in the detector have potential zero. In an infinite plate capacitor a single drifting charge carrier induces a current shaped like a step function. The current induced from uniform ionization in the gap can be obtained from the superposition of the current of single charge carriers and has a triangular shape

$$I(t) = \begin{cases} I_0\left(1-\dfrac{t}{t_d}\right) & ,0 < t < t_d \\ 0 & ,t < 0 \text{ or } t > t_d \end{cases} \ , \text{ with } I_0 = \frac{Ne}{t_d}. \tag{3.15}$$

In both cases the current signal is as long as the drift time of the charge carriers. However, in plate capacitors of finite size and for non-uniform ionization in the capacitor gap, the current shape deviates from these ideal pulse forms, as will be discussed in chapter 5.

A finite lifetime of the drifting electrons in the liquid inside the capacitor gap superimposes a falling exponential curve to the current.

Speed and Noise Limits

A simplified circuit for the readout of ionization chambers is given in figure 3.9.

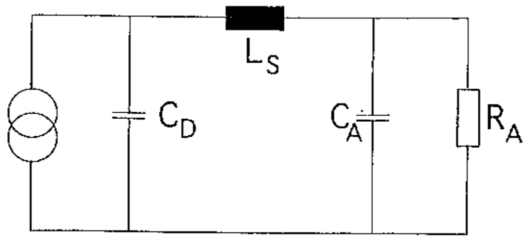

Fig. 3.9: Simplified circuit diagram for the readout of ionization chambers. C_D is the detector capacitance, L_S is the inductance of the connections, C_A and R_A are the capacitance and the resistance of the amplifier.

The limiting factor for the speed of ionization chambers is the charge transfer time that is necessary to discharge the detector capacitance into the connections to the preamplifier. This time is normally much longer than the signal propagation time in the circuit. A detailed analysis [Rad88/2] shows that the shortest signal propagation time is achieved for critical damping, i.e. $R_A = 1.54\sqrt{L_S / C_D}$ and $C_A / C_D = 1/8$. In this case

$$t_T \approx 3.5\sqrt{L_S C_D} \approx 2.3 R_A C_D \tag{3.16}$$

for the time in which 95% of the charge have been transferred to the amplifier. The minimum width of the output signal is four to five times longer. As the large surface of the electrode plates in ionization chambers results in a high capacitance (up to several nanofarads), fast signals are difficult to achieve. A possible technical solution is the direct connection of the preamplifiers to the calorimeter electrodes as used for the uranium-liquid argon calorimeter of the HELIOS experiment [BNL90] and the calorimeter prototypes of the RD3 collaboration [RD3/92] and the NA48 experiment. This technique requires the preamplifiers to be kept in the cold liquid.

As a consequence of (3.16), the input impedance of the preamplifier has to be small and is therefore neglected in the analysis of chapter 5.

The fundamental limit to the noise of the electronic chain is introduced by the amplifying device ("series noise"). All other electronic noise sources can be made negligible with proper effort. A detailed analysis of the equivalent noise charge for ionization chamber calorimeters due to the amplifier series noise [Rad88/2] gives

$$ENC_S = \frac{2}{\sqrt{3}}\sqrt{kT}\sqrt{C_D}\underbrace{\left[\frac{1}{n}\sqrt{\frac{C_D}{C_{in}}}+n\sqrt{\frac{C_{in}}{C_D}}\right]}_{=1,\text{ in the matched case}}\sqrt{\frac{\tau_A}{t_m}}\xi_S\sqrt{a_{F1}}. \tag{3.17}$$

In this formula n is the transformer ratio, which is used for capacitance matching (n = 1 if no transformer is used), $\tau_A = C_{in} / g_m$ is the amplifier time constant, C_{in} consists of the input capacitance of the amplifying device and the stray capacitance of the circuit at the secondary side of the transformer and ξ_S is the excess noise factor for white noise. a_{F1} is derived from the series noise integral

$$I_1 = \int_{-\infty}^{\infty}[h(t)]^2 dt = \frac{a_{F1}}{t_m}\left[s^{-1}\right] \tag{3.18}$$

with $h(t)$ being the impulse response of the shaping system.

The ratio of the equivalent noise charge and the observed signal charge becomes

$$\frac{ENC_S}{Q_S(t_m)} \propto \frac{1}{\sqrt{t_m}\left[\frac{t_m}{t_d}-\frac{1}{2}\left(\frac{t_m}{t_d}\right)^2\right]} \propto \begin{cases} t_m^{-1/2} & ,\frac{t_m}{t_d}>1 \\ t_m^{-3/2} & ,\frac{t_m}{t_d}<1 \end{cases}. \tag{3.19}$$

In the first region the effects of filtering on the noise with the variation of the high frequency cutoff dominate the behavior. In the second region the variation of the observed charge is added. There is a strong increase in the electronic noise for high speed calorimeters.

Chapter 4: The Prototype Tests

Experimental Setup

The Structure of the Prototype

The prototype NA48 liquid krypton calorimeter used in the 1992 tests had a cylindrical active volume of 32 cm diameter and 125 cm length, which corresponds to 7 Molière radii (R_M) and 27 radiation lengths (X_0) in liquid krypton. It was segmented in 184 $2\times2\,\mathrm{cm}^2$ cells parallel to the beam. The cells consisted of two half-cells, separated by electrodes stretched in the beam direction. Each half cell formed a parallel plate capacitor of 19 mm height, 125 cm length and a gap of 1 cm filled with liquid krypton. The electrodes consisted of 75 μm thick Kapton foils clad on both sides with 17.5 μm thick copper strips, resulting in a total thickness of 130 μm including glue. The electrodes in the center of a cell acted as anodes. They were connected through a 10 MΩ resistor to the high voltage supply and via a coupling capacitor (3 nF, 13 kV) to the preamplifiers. The electrodes at the edge of the cells acted as cathodes, connected to ground. The capacitance between one anode and the opposite cathode was measured to be 30 pF [Buch]. The anodes of both half-cells were connected to one preamplifier. Adjacent cells were separated by a gap of 1 mm. Figure 4.1 shows the layout of four cells.

All electrodes in a vertical row were glued on one side of a Kapton foil. 33 foils of different size were used (fig. 4.2). The ends of the foils were glued in sandwiches with boards of Stesalit-G10, which provided signal and high voltage connections. These blocks were fixed at the ends of a cylindrical support structure of stainless steel, which slid into the inner vessel of the cryostat. 1 mm thick Stesalit-combs, located every 30 cm for the first test and every 15 cm during the second test, helped to keep the distance between the foils constant. At room temperature the precision of the position of the foils was generally better than 100 μm. Unfortunately displacements due to different shrinking during cool-down led to displacements of 300 μm in the first 15 cm of the calorimeter [Mart]. The readout boards were installed downstream of the foil structure, the high voltage connections were mounted on the upstream end of the foils.

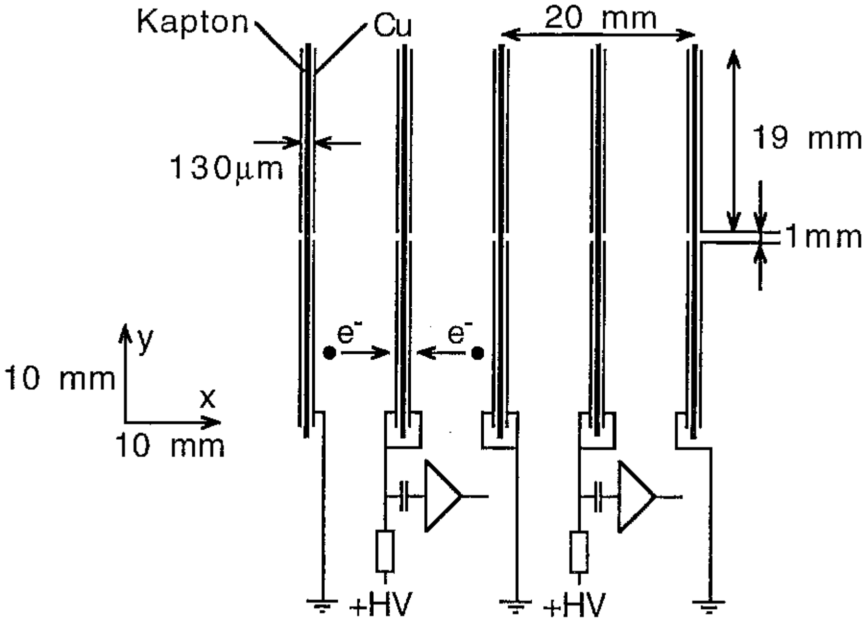

Fig. 4.1: Four cells of the readout structure, seen against the direction of the beam.

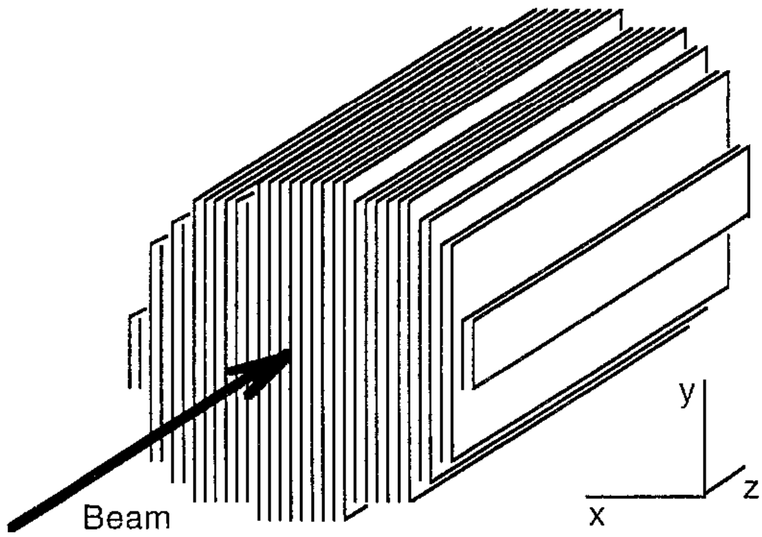

Fig. 4.2: Foil structure of the prototype.

Cryogenics and Gas System

The cryostat of the liquid krypton calorimeter prototype consisted of two coaxial stainless-steel vessels. The space between the vessels was evacuated to provide sufficient insulation. In the front of the cryostat a circular stainless steel beam window of 9 cm diameter was located.

Two high-voltage and two signal feedthroughs provided the electrical connections to the readout structure.

The inner vessel contained approximately 180 liters of liquid krypton, which was kept at a pressure of 1.2 bar. The boiling temperature of the liquid was 122 K. During one hour approximately one liter of liquid krypton evaporated, which was then warmed up to room temperature, purified in a gas purifier and sent to the krypton cooler for reliquefication.

The Readout of the Calorimeter Prototype

The demand on the high rate capability for the NA48 experiment determines the readout of the photon calorimeter. A longitudinal tower structure with preamplifiers mounted on the end of the towers keeps connections short and capacitances low. As a consequence, the preamplifiers are contained in the liquid krypton, which makes access to them difficult.

The electronic part of the readout uses the initial current readout method. The signal from the calorimeter is in first approximation a triangular shaped current pulse as described in (3.15). This signal is integrated in a charge integrating preamplifier. These preamplifiers, which were originally designed at the BNL for the liquid argon accordion calorimeter of RD3, have a risetime of 30 ns and a time constant of 6.6 μs. For the second test, the feedback capacitor of the preamplifier was changed to double the gain with the aim of improving the signal-to-noise ratio. This shortened the time constant to 3.3 μs. The risetime of the preamplifier was not influenced by this change as additional modifications kept the bandwidth constant.

The preamplifiers were mounted on motherboards which were connected to the foils such that each preamplifier on one motherboard was connected to a different anode foil (fig. 4.3).

The output of the preamplifiers was led through the signal feedthroughs and via 20 m long flat cables to the shapers, where the signal was differentiated twice and integrated four times [Note91/9]. The shaper output pulse had a risetime of less than 100 ns and a full width at half maximum (FWHM) of less than 200 ns. This pulse was followed by a small undershoot (5% of the amplitude) with a length as long as the drift time of the electrons in the gap (~3 μs). The pulse height of the shaper output signal was proportional to the result of an integration of the current signal from the calorimeter during the first 60 ns. This is the reason, why this method is called initial current readout technique. An overview of the different signals in the readout is given in figure 4.4.

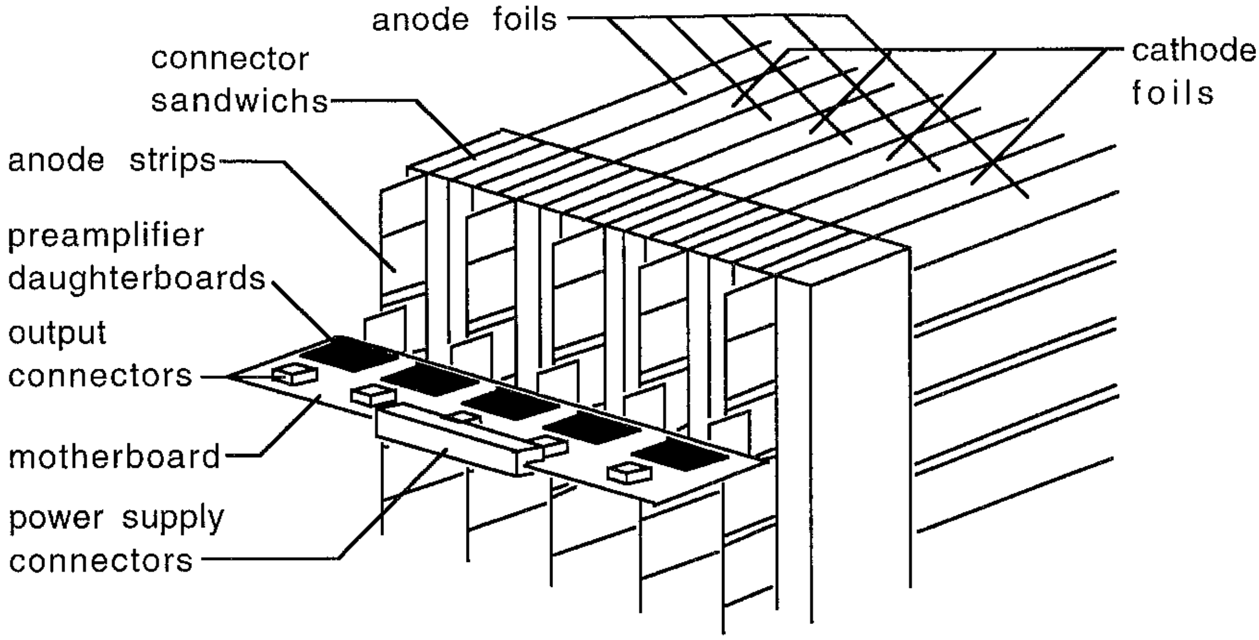

Fig. 4.3: Connection of motherboards to the foils (back side of the calorimeter).

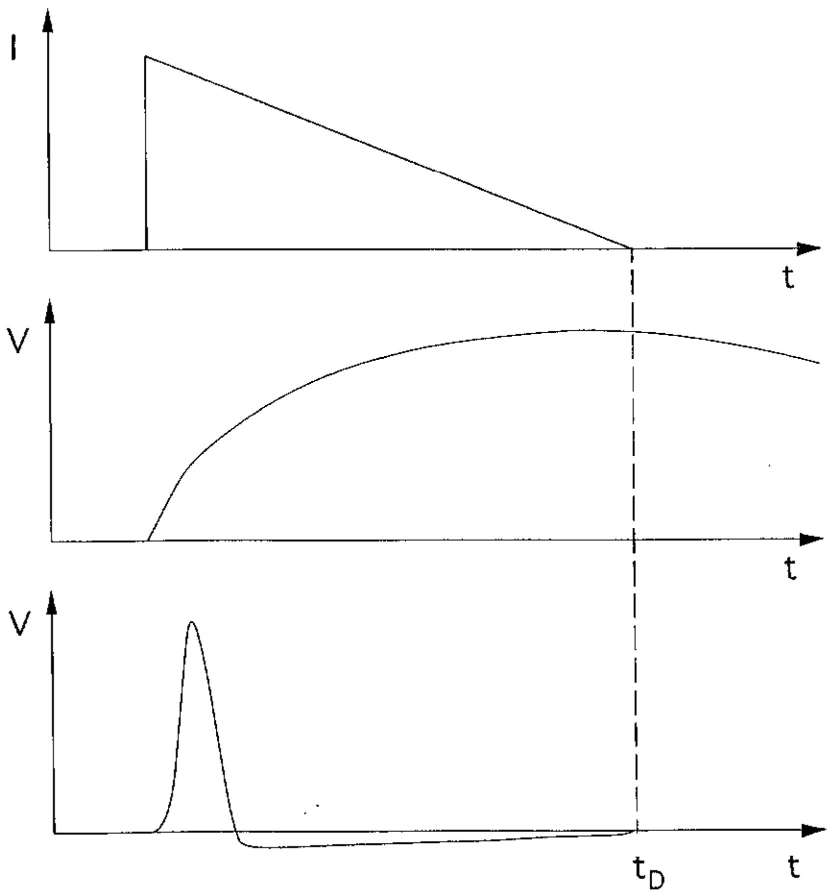

Fig. 4.4: The calorimeter readout. The upper figure shows an (idealized) current pulse from the calorimeter. The sketch in the middle shows the resulting preamplifier output pulse. The signal decays exponentially after the period shown in this figure. The last figure shows the resulting shaper output pulse.

The integration of the current during a period of 60 ns led to a different shaper output for the same amount of ionization charge if the falling slope of the current signal changed (fig. 4.5). The resulting shaper output signal had a different pulse height and a different length. An extremely fast drop of the current signal (as it happened for very short electron lifetimes) led to an increased undershoot and the shaper output pulse became bipolar.

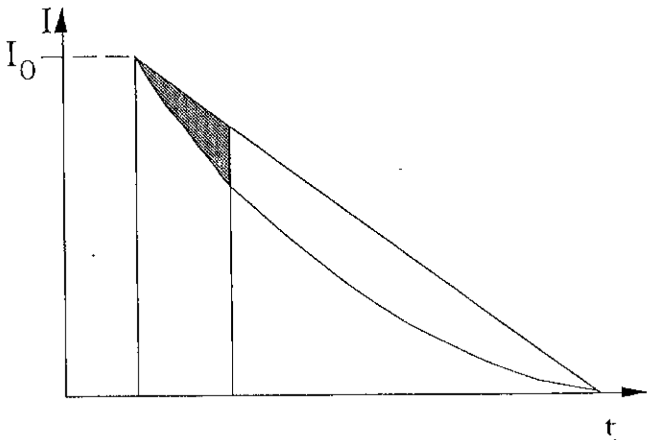

Fig. 4.5: Different results for for different signal shapes.
dashed area gives the differen ırements for the two curves.
integration time is shown larg.

The shaper has three different outputs for each readout channel. These were used during the two tests of 1992 to connect three different analog to digital converter (ADC) systems: A conventional peak sensing and a charge integrating ADC system (LeCroy LRS 2281 and LRS 2282) and a Flash-ADC system (STRUCK STR 750). During the second test a waveform analyzer (LeCroy LRS 6841) was connected to the preamplifier output of one cell per run to record the pulse shape of the signal at the shaper input.

The FADC System

The FADC system consisted of STRUCK STR755 FADCs with a STRUCK STR751 master module. The properties of this FADC system can be found in table 4.1.

resolution	8 bit linear
sampling frequency	40 MHz
DC - linearity	± 1/2 LSB
AC - linearity	± 2 LSB
bus standard	VME
channels per module	8

Tab. 4.1: The STRUCK STR750 FADC system.

As the dynamic range of a FADC channel was too small for the expected signals[5], more than one FADC channel was connected to the center cells of the calorimeter. The FADC channels connected to the same cell differed in the gain. For the first test 32 cells were equipped with two FADC channels per cell. The different gains were achieved by modifying the input amplifiers of the FADCs. During the second test 16 cells were connected to three FADCs and other 16 cells were connected to two FADCs. During the second test all FADCs had the same input amplifiers. The difference in gain was achieved by passive attenuation of the signals by factors of 2, 6 and 18. The setups for the two tests are listed in table 4.2 and the connection schemes are shown in figure 4.6.

Test	channels	FADC gains	chan/gain	dynamic range
June 92	104	high gain (×20)	72	1:1000
		low gain (×5)	32	
November 92	128	high gain (×10)		1:15000
		shaper gain off (×1)	38	(whole system)
		shaper gain on (×6)	42	1:2500
		medium gain (×3.3)	32	(one channel)
		low gain (×1.1)	16	

Tab. 4.2: The setups of the FADC systems during the 1992 tests.

[5] Since the FADC system should operate up to 50 GeV showers, the noise due to quantization effects would be about ten times the required value as about 50% of the shower energy is expected in the center cell. Then 1 LSB corresponds to 100 MeV and the error becomes $\frac{100 MeV}{\sqrt{12}} \cong 30 MeV$ per cell.

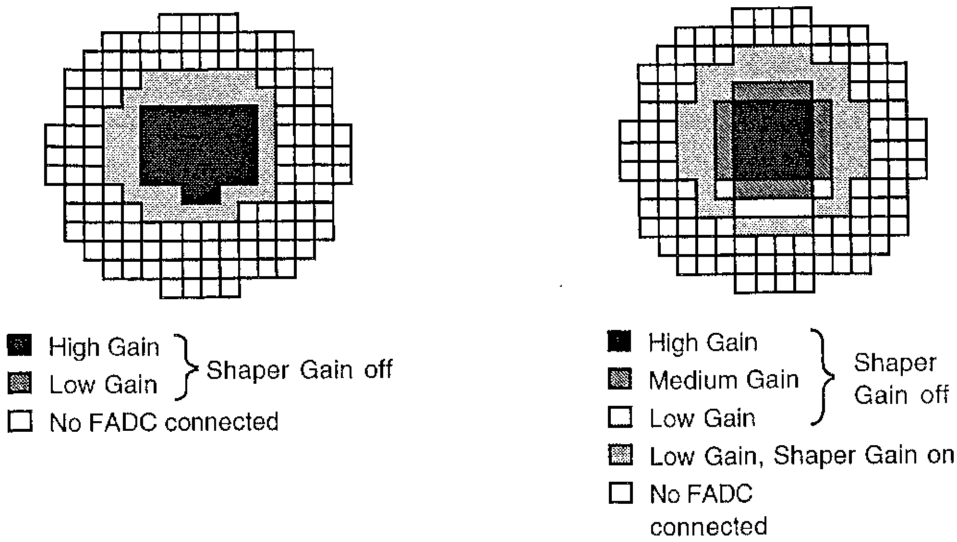

Fig. 4.6: Connection of FADCs during the two tests. The calorimeter is seen from the back.

The behavior of the FADC system for different beam energies was simulated under the conditions of the second test. The connection scheme together with the count-to-energy conversion factors for the different gain types defined the possible energy ranges for each cell and for the connected FADCs. A pedestal of 15 LSB was assumed. The response was investigated for impact points reconstructed from the data. The energy in each cell was computed from a radial profile of the signal height that was obtained from the test data (fig. 4.7). This shower profile was scaled in magnitude with the beam energy whereas the lateral dimension was not modified.

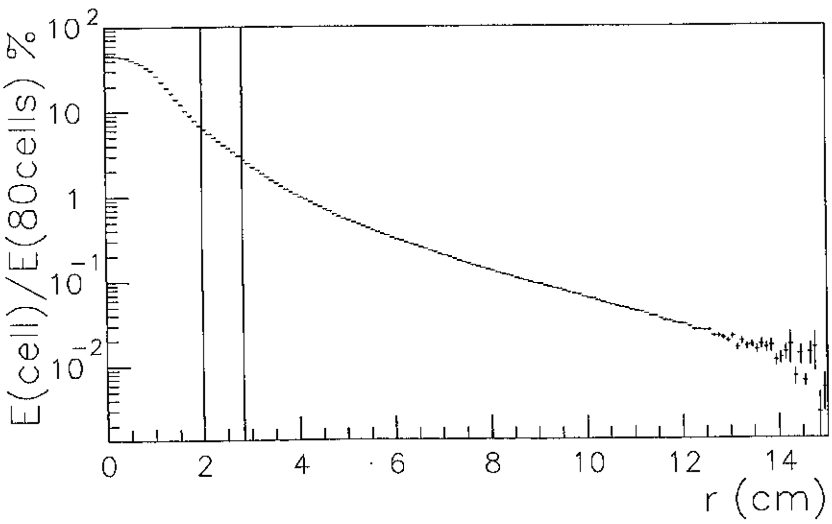

Fig. 4.7: Signal height as a function of the distance between the center of gravity and the center of the particular cell. The two lines give the position of the eight nearest cells, if the particle had hit the center of one cell (the distance between two cells is 2 cm).

The number of cells for each FADC gain type is shown in figure 4.8. The result of the simulation shows a discontinuity at 12 GeV because the shaper gain was switched on for all cells during runs with energies lower than that. From the same simulation the fraction of events, for which it was not possible to recover a saturation by replacing the saturated FADC with a lower amplifying FADC, was also determined (fig. 4.9).

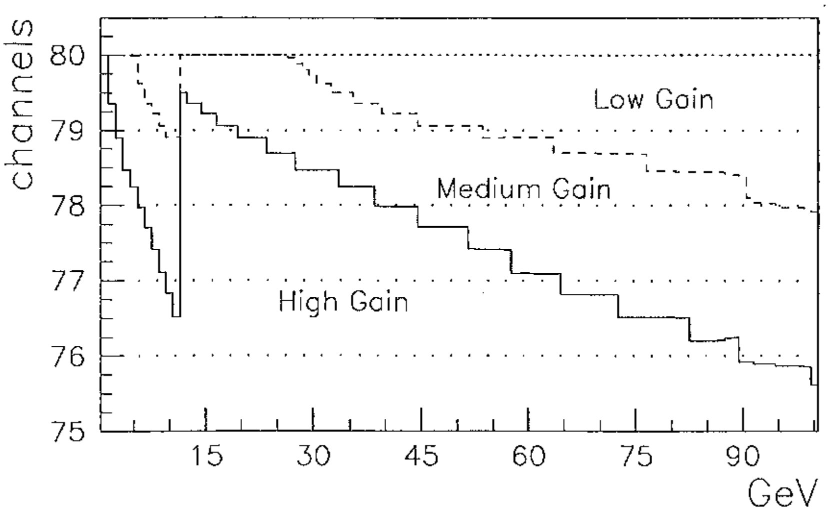

Fig. 4.8: Average number of cells per FADC gain type for different beam energies. The plot shows the number of cells, where the particular gain type had the highest gain without being saturated. The complete showerbox contained 80 cells.

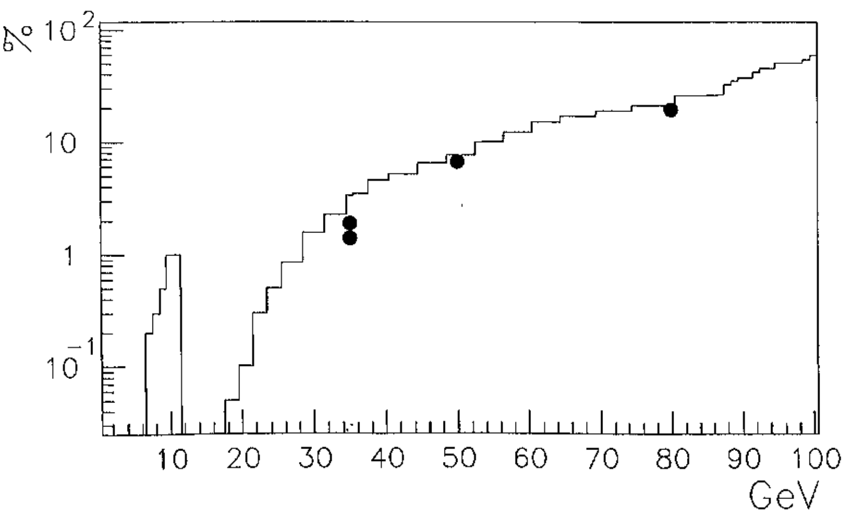

Fig. 4.9: Fraction of saturated events for different beam energies. The line shows the result from the simulation, points give results of the test.

With the information of the number of FADC channels of different gain used in each event, the noise due to quantization errors was calculated. The contribution of the quantization noise to the energy resolution assuming a pure quantization error of $1/\sqrt{12}$ LSB is shown in figure 4.10.

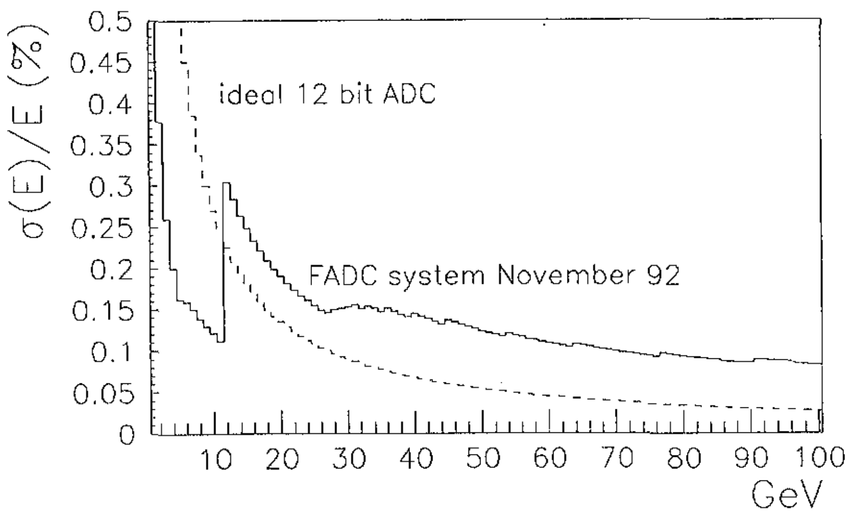

Fig. 4.10: Contribution of the quantization noise to the energy resolution for different beam energies. For a comparison the effect of the quantization noise of a 12 bit linear ADC system is shown.

To give more exact information of the time of the FADC samples, a TDC (LeCroy LRS2228A, 50 ps time samples) was used. This device measured the time between the trigger signal and the clock signal of the FADC system.

The error of the clock phase measurement can be estimated from the spectrum of the TDC counts. The ideal 500 counts wide rectangular distribution was broadened by 5 counts on average (fig. 4.11). The error on the clock phase measurement was therefore estimated to 100 ps.

During the first test the STOP signal for the FADC system was not synchronized with the clock phase, which could lead to a missing sample, if the STOP signal reached the master module at an edge of the clock signal. This occurred in about 1% of the events. The problem was solved in the second test by synchronizing the STOP signal such that it arrived in the middle of an FADC clock signal.

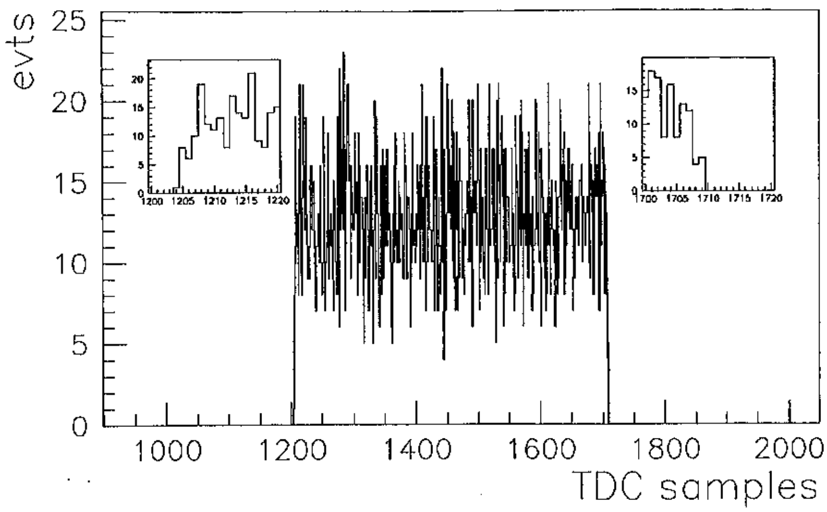

Fig. 4.11: Spectrum of counts of the TDC that measured the clock phase of the FADC system.

During both tests, 48 FADC time samples were recorded per event, thus providing a time window of 1.2 μs. In the time window the signal from the shaper started with a delay. This delay was 32 samples long during the first test and 20 samples long during the second test. From the samples before the start of the signal, the pedestal (the positive offset of the FADC) was determined event by event and channel by channel. It had been set by the data acquisition to approximately 15 LSB. The shape of the pulse supplied to the FADC input for electron events is shown in figure 4.12. Two typical FADC raw data sets are shown in figure 4.13.

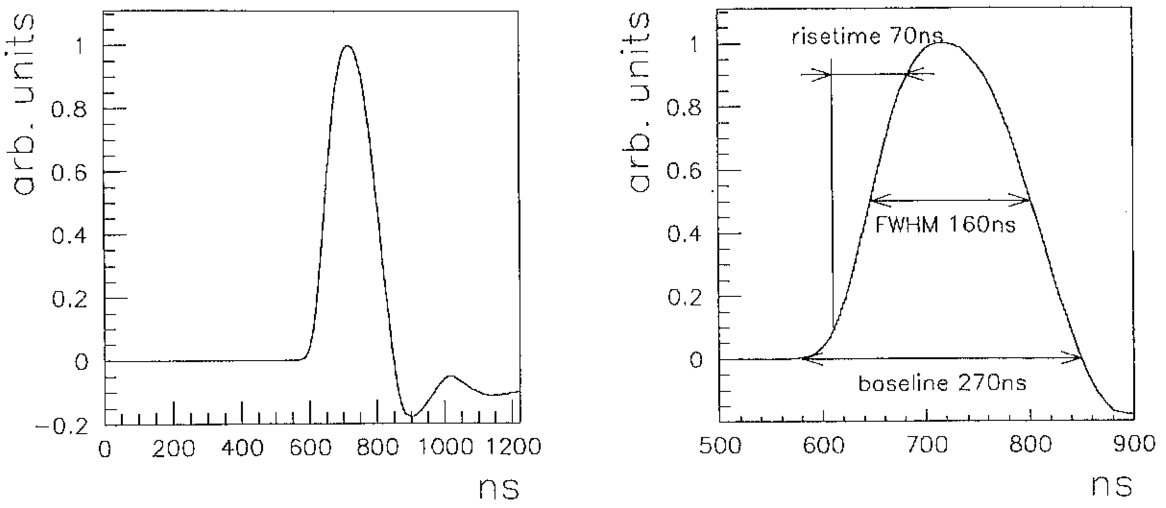

Fig. 4.12: FADC input signal. The plot is the vertical average of approximately 6000 normalized electron events. The FADC clock phase information from the TDC was used to fill the data into bins of 1 ns width (November 92).

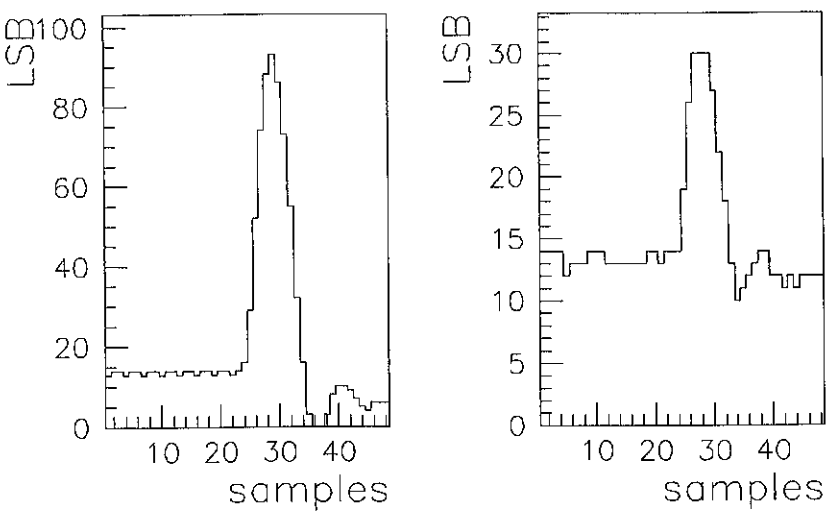

Fig. 4.13: Examples of FADC raw data (one event). The pedestal of about 14 LSB is visible. The left plot shows the output from a low gain FADC in the cell nearest to the center of gravity of the charge in the calorimeter. The right plot gives the result from a high gain FADC during the same event, about 4 cm from the center of gravity.

The Calibration System

Variations in the electronics of the calorimeter lead to cell-to-cell differences in the response of the calorimeter. Therefore the output of the calorimeter has to be calibrated. The goal of a constant term of 0.5% leads to the requirement, that cell-to-cell differences should be kept at the level of 1%.

For the calibration, current pulses, which were comparable in size and shape to the expected signals from the calorimeter, were produced. The pulse height of the FADC signals resulting from these reference pulses could be compared with the known input current. The calibration current signals were produced by a calibration circuit on each motherboard to avoid distortions by long signal connections. From these pulses a conversion factor between FADC counts and the input current was obtained for each ADC. The conversion factor was used in the off-line analysis of the electron data to translate the measured pulse height of the pulse into a current.

A displacement of the electrodes changes the cell capacitance and the current that is induced by the drifting charges. Thus cell-to-cell deviations in the gap width cannot be corrected by this calibration.

The calibration signal was obtained by discharging a capacitor of 2 nF through a 1 kΩ resistor, giving a time constant of 2 μs (fig. 4.14). The discharching was switched with a very fast switching Field Effect Transistor (FET). The signal was coupled to the preamplifier with a small capacitor of 13 pF. The pulse height of the calibration pulses was controlled with the voltage supplied to the FET by a digital to analog converter (DAC) under control of the data acquisition system.

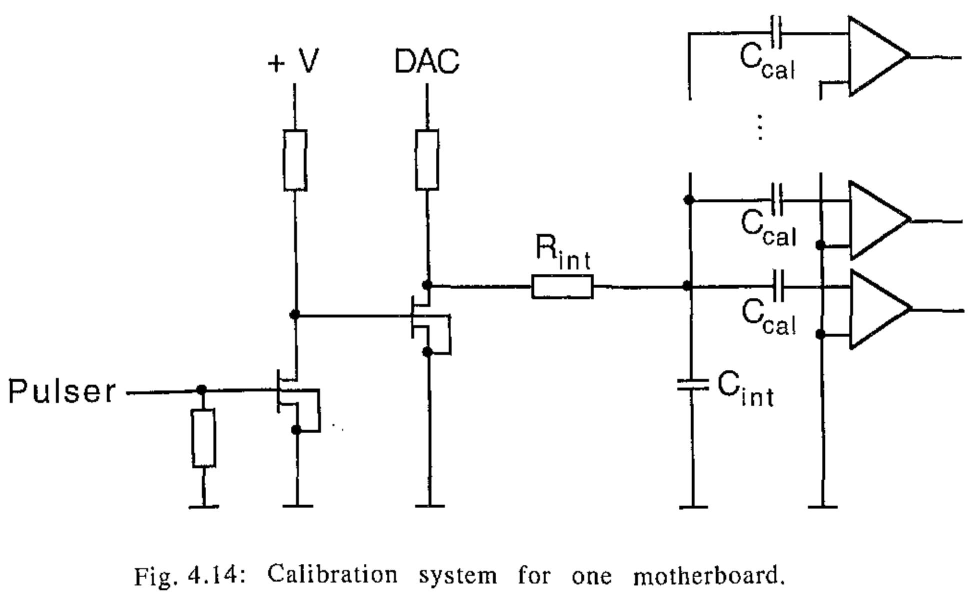

Fig. 4.14: Calibration system for one motherboard.

The capacitances and resistances of the calibration system had to be measured for each channel at room temperature and in liquid nitrogen [Note91/5]. The results of these measurements were linearly extrapolated to liquid krypton temperature. After the analysis of the 1992 tests it was realized that the resistance of the FET showed a non-linear temperature dependence. This introduced miscalibrations between different motherboards at the level of 2-3% [Min3/6/93].

The initial current from the calibration circuit can be calculated from the measured properties as

$$I_{\max} = \frac{C_{cal} V_{DAC}}{\left(C_{int} + \sum C_{cal}\right)\left(R_{int} + R_{FET}\right)}. \tag{4.1}$$

The calibration system was pulsed by a second FET that was used to address specific motherboards. To reduce cross-talk only the calibration circuits on every fourth board were addressed for one calibration pulse.

The switching of the FET induced a pickup pulse, which led to a distortion of small signals. This pickup caused a signal even if no voltage was applied. The size of the pickup was up to 100 MeV (fig. 4.15). During the first test several motherboards (9, 10, 13 and 14) showed larger pickup signals due to broken cables inside the cryostat. To avoid disturbances for other motherboards the addressing of the motherboards was divided for the first test such, that these motherboards were calibrated separately.

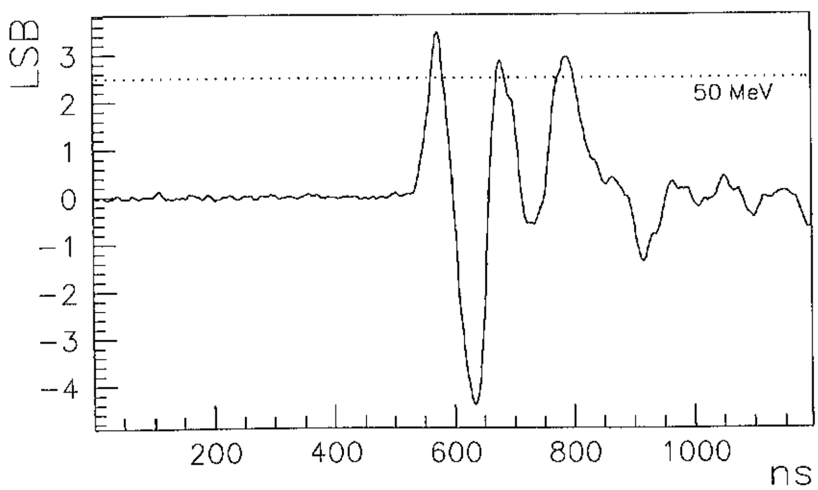

Fig. 4.15: Pickup pulse averaged from 500 calibration events, in which a zero reference voltage was provided by the DAC to an addressed calibration system. The FADC clock phase TDC provided the exact time information (November 92).

The Test Beam Setup

The beam tests took place in the H4 beam line at the North Experimental Area of the CERN SPS. The prototype was exposed to electron, muon and pion beams with momenta between 10 and 120 GeV with an intensity of about 10 ktrigger/burst during the first and 1 ktrigger/burst in normal runs during the second test. The pion contamination in the electron beam at nominal setting was at the per mille level (high intensity). Detuning the beam intensity for the second test increased the pion rate in the beam to a few percent.

A scintillator hodoscope started the data acquisition. Two different types of triggers, an electron trigger and a muon trigger, were used, depending on the beam type. The electron trigger was given by the coincidence of a signal in two small trigger counters (S_1 and S_2, $9 \times 9\,\mathrm{cm}^2$) and no signal in an anticounter (A, $35 \times 35\,\mathrm{cm}^2$) in front of the calorimeter. The anticounter had a hole of 8.5 cm diameter, which was slightly smaller than the beam window of the cryostat to ensure that no particle hits the flange of the window. The muon trigger required a hit in the two muon counters (μ_1 and μ_2, $35 \times 35\,\mathrm{cm}^2$), one in front and one behind the calorimeter. In addition the trigger logic provided a logical OR of S_1, S_2 and A, which was used to flag events with additional activity in the calorimeter within a short time ($3\,\mu$s) before and after the recorded event. For the second test all counters were equipped with constant fraction discriminators (EG&G Ortec 935) to provide better information on the time at which the particle passed the hodoscope. The time resolution of the trigger with respect to a signal from a fast reference trigger counter (NE110) with 70 ps time resolution was measured to be 190 ps. The standalone time resolution of the trigger signal from the electron trigger hodoscope is therefore 180 ps. During the second test the pulse height in the trigger counters S_1 and S_2 was measured by ADCs.

Two drift chambers between the trigger counters were used to reconstruct the impact point of the incoming particle at the calorimeter. Each chamber consisted of four staggered planes in x and in y with 12 mm wire spacing and covered an area of $16 \times 16\,\mathrm{cm}^2$. The space resolution for the impact point at the front of the calorimeter was $190\,\mu$m at 50 GeV/c increasing to $470\,\mu$m at 10 GeV/c due to multiple scattering in the trigger counters [NA48/93]. Two large proportional chambers were located behind the calorimeter. They were used to detect particles that had escaped from the calorimeter. During the second test a lead wall had been built between the prototype and the proportional chambers to improve the pion rejection with respect to electrons.

The total length of material in front of the calorimeter was estimated to be about 0.3 radiation lengths consisting mainly of 4 (5) trigger counters, the two stainless steel beam windows and 0.11 radiation lengths of Sintimid in the cryostat.

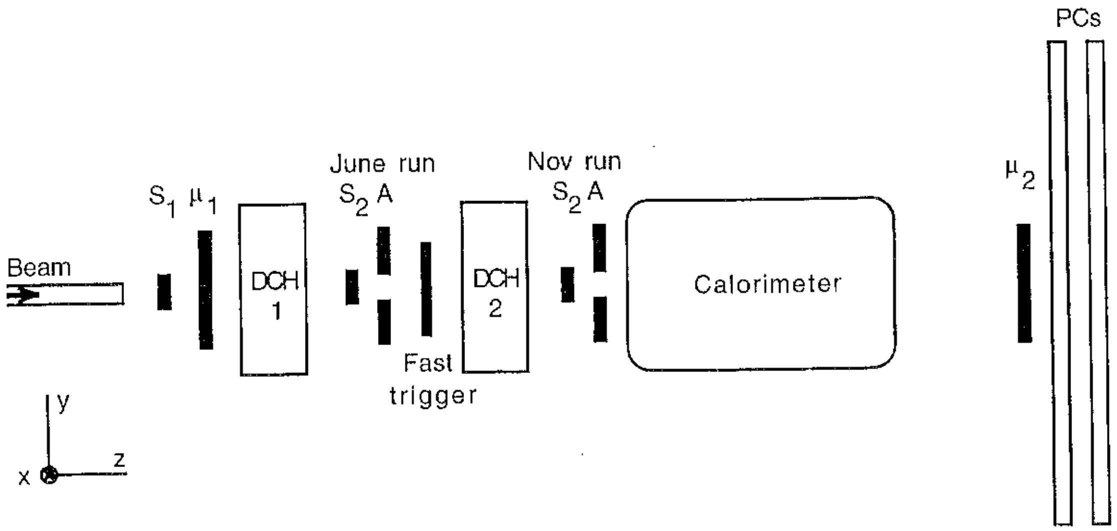

Fig. 4.16: Layout of the detector setups during the tests (no scale).

Changes in the Setup for the Second Test

The results of the first test suffered from a bad signal-to-noise ratio. Therefore several improvements to increase the signal-to-noise ratio were introduced before the second test started.

1. To increase the signal:

- During the first test, the electron lifetime in the liquid krypton was very short (100-200 ns) leading to a loss of signal height. After the run, a leak in the signal feedthroughs was identified as the source of the pollution of the liquid. For the second test, new feedthroughs were constructed, which solved the problem. The lifetime was then measured to be longer than 2 μs.

- The gain of the preamplifiers was increased by a factor of two. This did not affect the bandwidth as additional modifications in the preamplifier circuit restored the speed of the amplifier.

- The shaper gain was switched on ($\times 6$) for cells where the pulse height was low enough (outer region of the calorimeter). This provided a factor of two for the increase of the signal-to-noise ratio of these channels.

2. To decrease the noise:

- The analog electronics system was separated as much as possible from any noise sources, especially power supplies and crates housing digital electronics. Cables were protected with additional shielding.
- The FADCs with gain 5 showed a larger intrinsic noise than the FADCs with gain 20. These two types had a different amplifier in the input stage. During the second test, all FADCs were equipped with the same amplifier circuit like the high gain FADCs in the first test. Attenuating the signals by appropriate factors gave the different gains.
- As the number of available FADCs increased for the second test, it was possible to equip the center cells with three instead of two FADC channels per calorimeter cell. In addition the system had to operate only up to a beam energy of 50 GeV before saturation, as the low energy range was of greater interest. This decreased the contribution of the quantization by the FADCs to the energy resolution from less than 1.3% for the first test to less than 0.35% during the second test for energies greater than 5 GeV. These numbers improved for higher energies (fig. 4.10).

These efforts decreased the equivalent noise energy (ENE) for the complete showerbox from 60 MeV per calorimeter cell during the first test to 6 MeV/cell for the second test.

To decrease non-uniformities in the response of the calorimeter two changes were made compared to the first test. First, the calorimeter was equipped with more spacers between the electrode foils to fix their position more accurately. Secondly the calorimeter was tilted by a small angle (26 mrad) for several runs.

Analysis Methods

Software Techniques

For the off-line analysis of the data a FORTRAN program was written by a subgroup of the NA48 collaboration. The purpose of this analysis program was not only the calculation of the test beam results but also the test of several software tools and techniques for their usefulness in the final NA48 experiment. The code was written following the idea of object-oriented programming. To organize and handle the data the software package ADAMO was used. The conclusions of this software test are summarized in [Coll2/93].

Main Analysis Strategy

The basic procedure of the analysis was to obtain count-to-current conversion factors from the analysis of the calibration data. These were used in the analysis of the electron data to derive the initial current, which was induced by the drifting ionization charge, from the pulse height in each channel.

For both, calibration and electron data, the amplitude of the signal from the FADC data had to be calculated. To avoid non-linearities for small pulses and to reduce cross-talk effects, the amplitude of the signal was determined as the pulse height at a fixed time. For the analysis of calibration and of electron data two passes through the data were performed by the program. During the first pass the mean time of the amplitude of the signal was computed for each FADC as a function of the amplitude. For the analysis of the first test, the amplitude dependence was neglected by taking an average of the mean time for higher amplitudes. During the second pass, the exact amplitude was determined as the height of the signal at that derived fixed mean time.

After two passes in the calibration analysis a count-to-current conversion table for each FADC was obtained. It was used after the second pass of the electron data analysis to assign a value for the initial current to each cell of the calorimeter.

Signal Reconstruction Methods

To reconstruct time and pulse height of the signal from the FADC data two different approaches were used. For the analysis of the first test, the FADC data were fitted with a parabola. The time of the amplitude was taken as the time of the maximum of a parabola fit, where seven time samples were used in the fit. This number of points for the parabola fit showed the best resolution for the time of the amplitude. The center point of the fit range was given as the sample with the highest value measured by the FADC that could be found in an interval of 100 ns (samples 40-44 for calibration and samples 39-43 for electron data). This interval had been chosen according to the experience gained from the data. For all channels the same interval was used.

The amplitude was then calculated, reconstructing the signal with a parabola through the three time samples that were the closest to the mean time obtained during the first pass. The value of the parabola at this mean time was taken as the final amplitude of the signal.

The main disadvantage of this method was that due to the asymmetry of the pulse shape, the seven point parabola fit did not give the correct time of the amplitude but a later time (approximately 20 ns later for calibration signals). This resulted in a lower value for the calculated amplitude at this later time. For the first test the pulses from electrons were less asymmetric than the calibration pulses. The risetime was 65 ns and the fall time was 85 ns for calibration pulses, whereas both, rise- and falltime, were 65 ns for pulses from electrons. As a result, the time shift and the underestimation of the amplitude was smaller for the latter ones. Thus the use of the count-to-current conversion factor from the calibration was overestimating the initial current of the signal from the electrons. A comparison with the results of the Le Croy ADC systems showed that the initial current was overestimated by approximately 16%.

In the analysis of the second test, digital signal processing methods were used in order to be independent of the exact pulse shape. The time of the maximum was obtained by comparing a reference pulse with the signal. The best agreement was searched for by maximizing an auto correlation function (ACF)

$$ACF(\Delta x) = \sum_i F(x_i) F_{ref}(x_i + \Delta x). \tag{4.2}$$

The ACF was calculated in steps of 1 ns for an interval of 100 ns (samples 32-36 for calibration and samples 30-34 for electron data). Again, this interval was chosen according to the experience gained from the data. The time of the maximum was determined from the time of the maximum of a parabola through the points given by the ACF of the time step with the largest value for the ACF and of the two adjacent time steps.

The reference pulse was obtained by averaging approximately 6000-10000 pulses larger than 20 LSB (pedestal subtracted). The phase of the pulses was taken from the TDC. The mean value for time slices of 1 ns each was calculated. The resulting pulse was filtered with a digital Butterworth filter of second order with a cutoff frequency of 40 MHz[6].

In addition, the ACF was normalized as

$$ACF_{norm}(\Delta x) = \frac{\sum_i F(x_i) F_{ref}(x_i + \Delta x)}{\sum_i F(x_i)} \tag{4.3}$$

which gave an amplitude-independent measure for the similarity of the signal with the reference pulse. This was used to reject distorted pulses for the analysis of

[6] As the shaper bandwidth was limited to approximately 7 MHz one could have used a filter with a lower cutoff frequency than in this analysis. This was not done, as the quality of the algorithm was dominated by distortions of the input signal, not of the reference pulse. The cutoff frequency was chosen far away from the signal region to avoid any bias of the results.

calibration and, during the first pass, of electron data. Such pulses occurred especially at low pulse heights due to noise and quantization effects. A threshold of 0.7 for the normalized auto correlation function ACF_{norm}, common for all channels, was required (fig. 4.17).

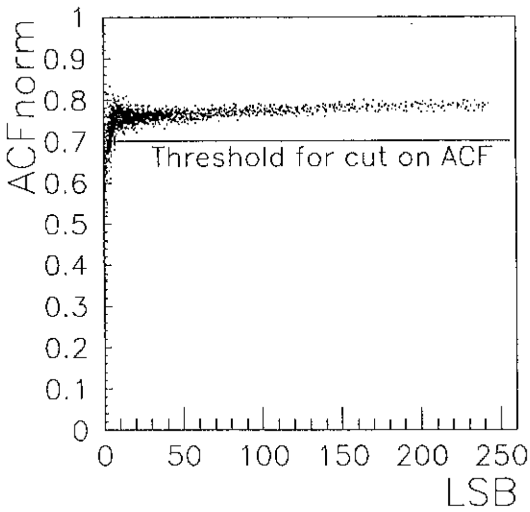

Fig. 4.17: Normalized auto correlation function ACF_{norm} as a function of the amplitude, electron data, November 92.

A digital low pass filter was used to reconstruct the pulse during the second pass. If the signal is ideally bandwidth limited at half the sampling frequency, the best approximation of the input signal for the FADC is given by

$$f(x) = \sum_i F(x_i) \frac{\sin(x - x_i)}{x - x_i}. \tag{4.4}$$

For the NA48 liquid krypton calorimeter, it is necessary to cut the long undershoots of the signals. This unfortunately violates the requirement of bandpass limitation. But as the undershoot is small, the error on the reconstructed pulse remains small at the time of the peak.

To obtain the pulse height at the time determined during the first pass of the analysis program, the time scale of the samplings was divided into 1 ns slices. The signal height at the three time slices closest to the mean time obtained in the first pass was computed using (4.4). The results for these time slices were connected with a parabola. The value of this parabola at the mean time gave the amplitude of the pulse. This procedure was used instead of using (4.4) directly to avoid errors due to very small numbers for $(x - x_i)$.

Event Selection Criteria

The requirements that had to be fulfilled by the events used in the analysis are listed in tab. 4.3. The activity within 3 μs before and after the event was measured by the trigger counters. This information is therefore uncorrelated with the calorimeter data. In addition for electron data no events out of the spill were allowed (this never happened because the trigger for beam events was gated by the SPS timing signals).

selection criterion	% of events loss PC HV off	% of events loss PC HV on
no activity within 3 μs before the event	1.1	0.7
no activity within 3 μs after the event	2.9	2.1
no clusters in the proportionalchambers	-	4.0
one track in x and y in the drift chambers	43.8	41.8

Tab. 4.3: Selection criteria for valid events (35 GeV, 1500 triggers/burst, November 92). 'PC' stands for 'Proportional Chambers'.

During the analysis of the first test, it was only required that a track was found in two views, independent of their orientation. Only later it was realized that in addition the correct orientation of the two views, one track in x and one track in y, had to be required.

For several runs during the second test beam period, especially for the runs belonging to the energy scan with the tilted calorimeter, the high voltage of the proportional chambers was switched off. Therefore the cut on the number of clusters in these chambers could not be used for the analysis of these runs.

The efficiency for the rejection of pions was measured with pure pion runs. At 35 GeV more than one tenth of the pion events passed all the cuts. The pion rejection improved with higher energy of the pions.

selection criterion	% of events loss
no activity within 3 μs before the event	0.5
no activity within 3 μs after the event	1.1
no clusters in the proportionalchambers	70.8
one track in x and y in the drift chambers	13.4
% of pion events that passed all the cuts	14.2

Tab. 4.4: Event rejection for a pure pion run (35 GeV, 1500 triggers/burst, November 92).

Chapter 5: Test Beam Results

As the off-line code was developed during the off-line analysis and the time between the two tests was just four months, only the noise behavior, the calibration results and the energy resolution were studied for the first test. These results and the corresponding results from the second test are discussed in the first part of this chapter. This is followed by a description of the results for the studies of the time and space resolution and of non-uniformity effects in the calorimeter during the second test. In the last part of this chapter the reason for the observed non-uniformities will be discussed.

Results of the Analysis for Both Tests

Noise

The total noise seen by the FADC system was computed from the fluctuation of the values measured by the FADCs in the first 32 samples of each event for the first test and of the first 16 samples for the second test. These samples contained only pedestals. The mean value of the pedestal was subtracted from each of these data. The resulting values were converted into charge and summed for each sample over all the FADCs. The RMS of a Gaussian fit to the distribution of the sums for all events defined the noise. The noise was calculated for each gain system separately.

To study the impact on the energy resolution it is necessary to consider the FADCs that were really used in the particular event (including which gain was used on a given channel). For this reason, non-Gaussian tails appear in the distribution (fig. 5.1). The width of a Gaussian fit to the distribution increases slightly with the energy (fig. 5.2).

The noise was divided into a coherent part and an incoherent part. For the calculation of the incoherent part of the noise, the sum for the values of all even-numbered channels was subtracted from the sum of all odd-numbered channels. The result was again histogrammed. The sigma of the distribution divided by the square root of the number of channels gave the incoherent noise per channel. The part of the coherent noise was obtained as the quadratic difference of the total noise in the system and the incoherent noise in the system. The coherent noise had to be divided by the number of FADCs used in the calculations to give the value for the noise per cell. The numbers for the noise per cell are given in table 5.1.

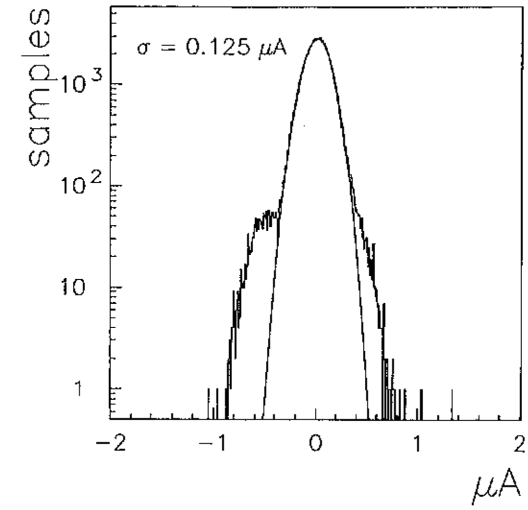

Fig. 5.1: Distribution of fluctuations in the first 16 samples, which contain only pedestals. The charge for each sample of all the cells used in the particular event for the calculation of the energy resolution is histogrammed. 1 μA corresponds to approximately 0.5 GeV (November 92, 35 GeV).

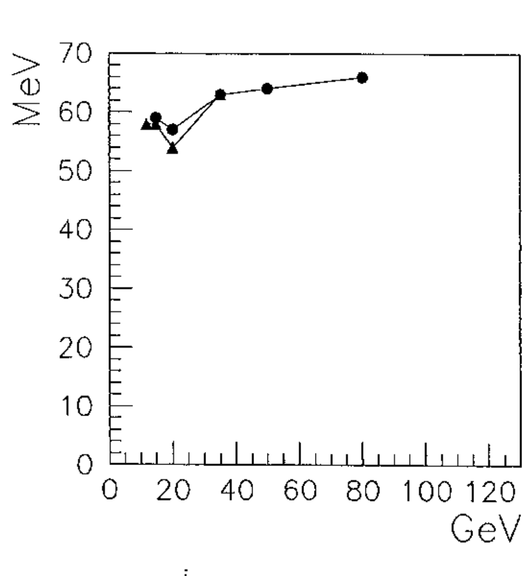

Fig. 5.2: Equivalent noise energy in the FADC system summed for all 80 FADCs used in the particular event for the calculation of the energy resolution. Circles give the result for the energy scan with the tilted calorimeter, triangles for the non-tilted calorimeter (November 92).

Test	FADC gain type	total noise	incoherent noise	coherent noise
June 92	high gain	28 MeV	27 MeV	6 MeV
	low gain	158 MeV	156 MeV	24 MeV
November 92	high gain ×6	1.7 MeV	1.7 MeV	< 1 MeV
	high gain ×1	6.8 MeV	6.7 MeV	< 1 MeV
	medium gain ×1	14.2 MeV	14.1 MeV	1.7 MeV
	low gain ×1	47.4 MeV	47.3 MeV	2.3 MeV

Tab. 5.1: Equivalent noise energy per cell for the two tests for different FADC gain types. The gain of the shaper is marked with '×6' (shaper gain on) or '×1' (shaper gain off).

As the noise was a severe problem during the first test, several efforts were made to find criteria to select noisy events that could be rejected in the analysis. After observations from the on-line monitoring it was assumed that the noise appears in packages of limited duration followed by periods of lower noise intensity. As the duration of these periods was longer than the length of the event it should have been possible to distinguish between events with higher and lower noise intensity. This expectation could not be met.

- The RMS of the noise and the peak to peak difference of the first 32 samples for each event were studied. They had a continuous spectrum for all events. No particular noisy events could be identified.

- The noise in the first 16 samples of the pedestal region showed no correlation to the noise in the second 16 samples of this region. This showed that no conclusions regarding the noise in one period of the event could be drawn from the noise in a different period. Therefore it was not possible to conclude from the noise intensity during the pedestal samples (sample 1-32) to the noise intensity during the pulse of the event (sample 33-48).

Results of the Calibration

For a long calibration run, which was used for the calibration of the FADCs, the voltage of the DAC was increased in steps proportional to n^2-1 with n=1,...64 and additional steps at very low pulse heights for the second test considering the larger dynamic range. For each step, 500 events were recorded. The pickup signal was determined from the first 500 events, in which the motherboards were addressed, but no reference voltage was applied to the calibration system. The signals of these events were averaged for each FADC in time slices using the phase information of the TDC. These time slices were 12.5 ns wide for the first test and as this turned out to be too rough, 1 ns wide for the analysis of the second test. In the latter case, the reconstructed pulse were smoothed by a digital low pass filter (Butterworth filter with 40 MHz cutoff frequency) as the low statistics in each time slice distorted the reconstructed pickup pulse. The resulting pickup pulse was subtracted at the beginning of the calibration analysis for each event.

The reconstructed time of the maximum ACF showed an amplitude dependence as shown in figure 5.3. Figure 5.4 shows examples for the characteristics of different gain types.

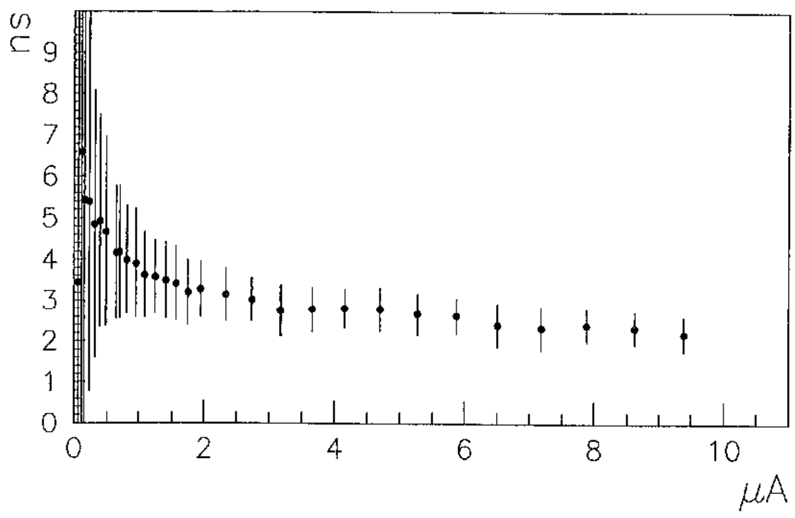

Fig. 5.3: Time of the maximum as a function of the pulse height, calibration, November 92.

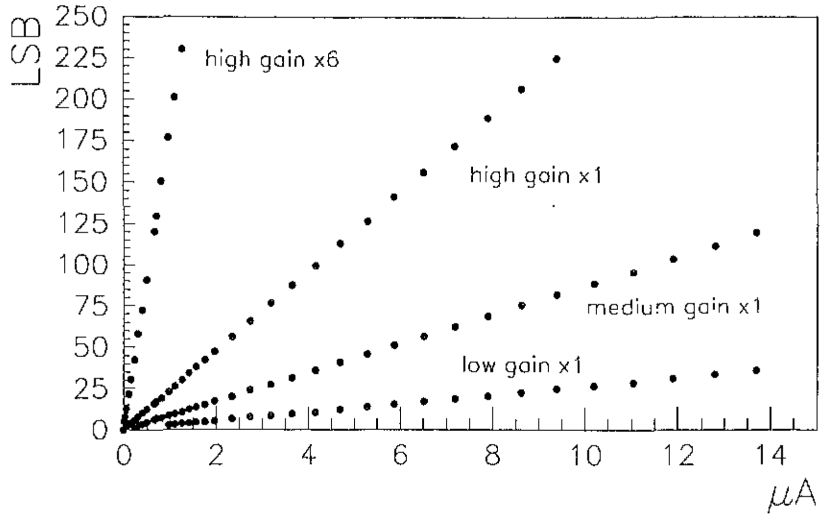

Fig. 5.4: Example for the count-to-current characteristics of the FADC system as obtained from the calibration for the different FADC gain types. Error bars are shown but too small to be visible.

The calibration resulted in a count-to-current conversion factor for each FADC channel. An overview of the count-to-current conversion factors for the different FADC systems is given in table 5.2. The count-to-energy factors result from a comparison of the beam energy to the sum of the current added in the showerbox.

Test	FADC gain type	μA per LSB	MeV per LSB
June 92	High gain	0.05	30
	Low gain	0.19	130
November 92	High gain ×6	0.006	3
	High gain ×1	0.04	20
	Medium gain ×1	0.1	50
	Low gain ×1	0.35	170

Tab. 5.2: Count-to-current and count-to-energy conversion factors.

Energy Resolution

The sum of the initial current in all cells of the calorimeter is proportional to the charge produced by the shower and therefore to the energy of the incoming particle. In practice, the charge is not summed in the whole calorimeter but in a number of cells around the impact point of the particle. The size of the showerbox which contains the cells to be summed is preferred to be large to keep the deterioration of the energy resolution due to transverse shower leakage small. However, the size of the showerbox is limited by the noise, which scales with the square root of the number of cells in the showerbox. For the FADC system used in the 1992 tests of the liquid krypton calorimeter, the restricted number of available FADCs yielded another limitation to the size of the showerbox. For the analysis of both tests, all cells, which were equipped with FADCs were used in the showerbox. This gave a box of 72 cells for the first test and of 80 cells for the second test. A typical distribution for the sum of the charge in the 80 cells showerbox is shown in figure 5.5.

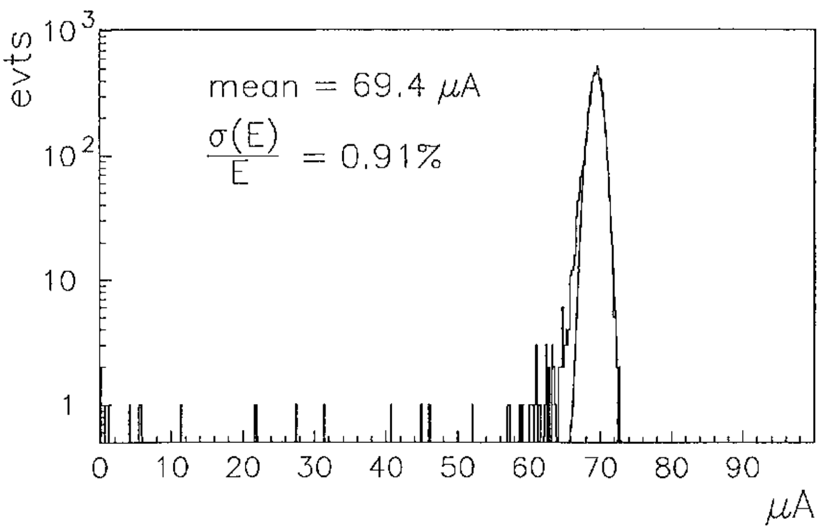

Fig. 5.5: Distribution of the initial current summed in a showerbox of 80 cells (November 92, 35 GeV, non-tilted calorimeter).

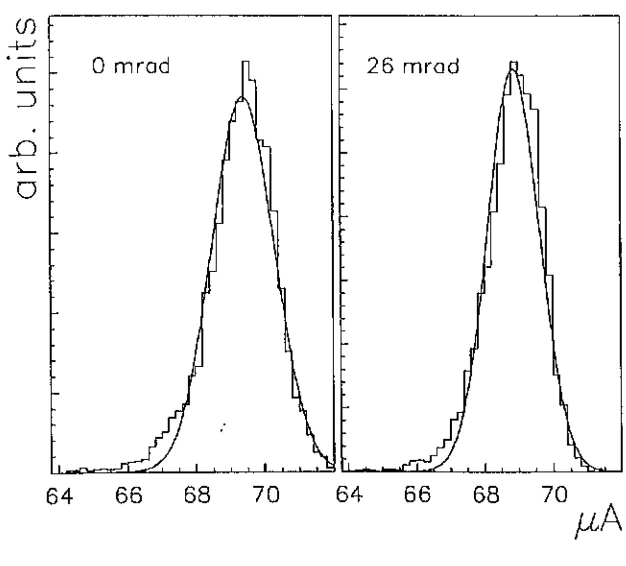

Fig. 5.6: Comparison of the peak of the initial current distribution for a non-tilted calorimeter and for a tilted calorimeter (November 92, 35 GeV).

The low energy side of the peak of the distribution showed a non-Gaussian shoulder. The reason for this shoulder can be found in the non-uniform response of the calorimeter and will be explained later. The non-Gaussian shoulder was reduced in the case of the tilted calorimeter configuration (fig. 5.6).

The energy distribution had low energy tails. 0.7% of the events remaining after the normal trigger cuts showed an energy which was smaller than 90% of the mean energy of the peak of the energy distribution. Different approaches to understand the reason for this low energy tail were investigated:

- The efficiency of the protection against additional activity in the calorimeter before and after the event was tested. Most of the events that contained an additional pulse in the time window, which was provided by the FADC data, were correctly marked with a protection flag. Neither pile up effects nor errors in the calculation of the pedestal due to additional pulses could be found.

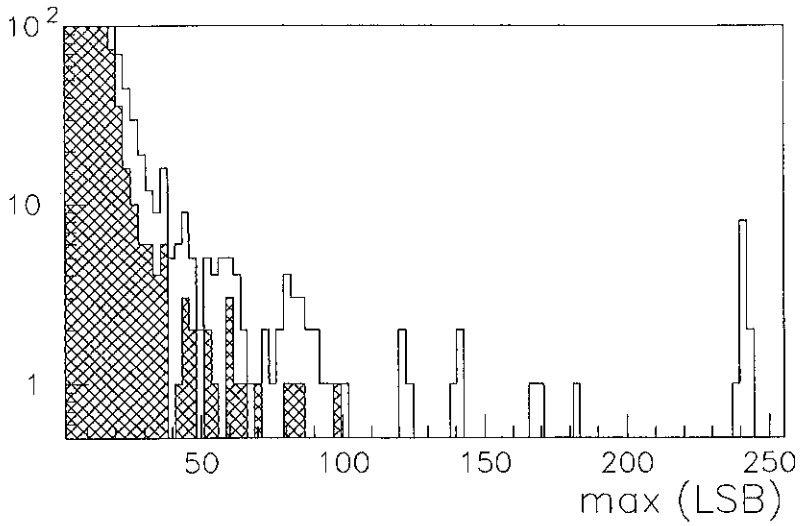

Fig. 5.11: Distribution of the highest value recorded in any high gain FADC outside the time of the pulse. The full line shows all events without requiring that no additional activity occurred in the calorimeter. The dashed area gives the distribution for the events for which the before and the after protection flags were not set.

• The pulse height spectra in the trigger counters show the same distribution as the spectra for events with correct total energy in the showerbox. This excludes that events in the low energy tail are from particles which induce showers before they hit the calorimeter.

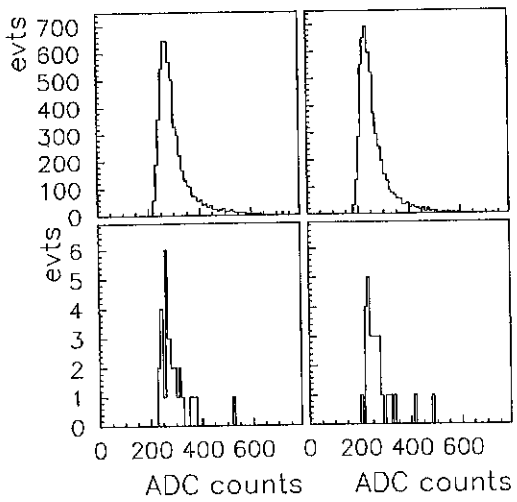

Fig. 5.9: Pulse height spectra for the signals in the two small trigger counters S_1 (left) and S_2 (right). The upper row shows the spectra for all events. The lower histograms contain only events with an energy less than 90% of the mean value of the peak of the energy distribution.

• The distribution of pedestals was studied to look for events with a corrupted pedestal. The deviations from a Gaussian distribution are too small to explain the observed low energy tail.

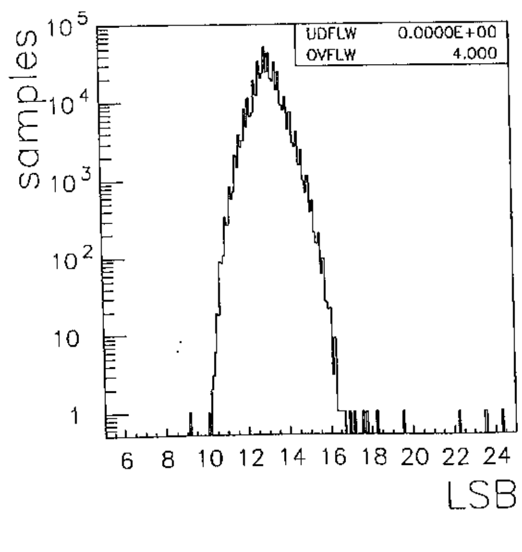

Fig. 5.12: Distribution of the pedestals.

- The full width at half maximum (FWHM) of the pulse in the center cell of the shower was calculated to look for any deformation of the signal for events with a lower total energy. No distorted pulses could be observed which could be an indication for an error in the electronics chain.

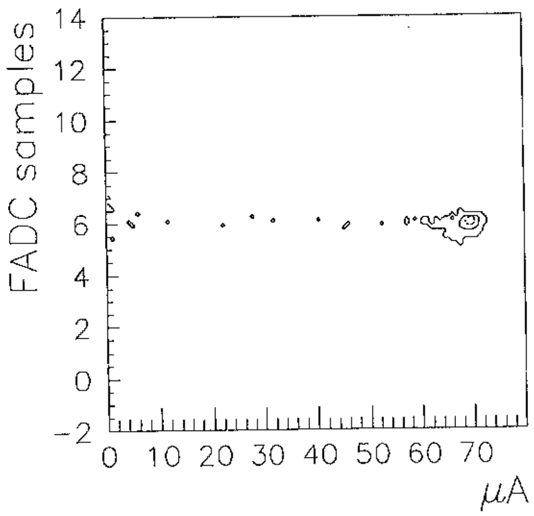

Fig. 5.10: FWHM of the pulse in the cell with the highest amplitude as a function of the total initial current added in an 80 cells showerbox.

- The events in the tail show no significant position dependence, as reconstructed with the drift chambers.

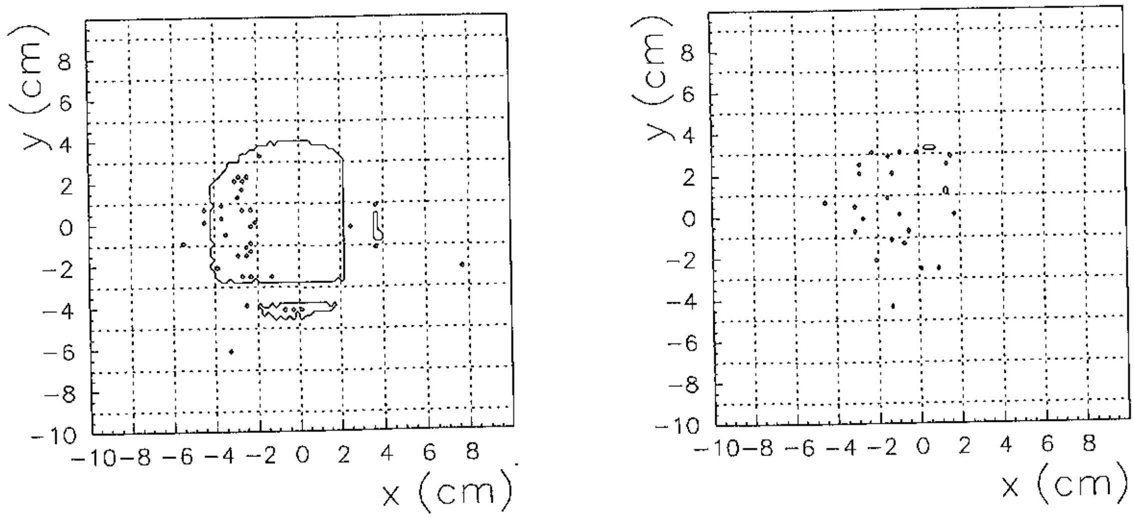

Fig. 5.8: Beam profile reconstructed with the drift chambers. In the left figure the beamprofile for all events is shown. One can see the circle defined by the anticounter in the trigger. Missing slices are due to dead wires in the drift chambers. In the right figure, only events with an energy less than 90% of the mean value of the peak of the energy distribution are plotted. The dotted lines give the dimensions of the cells.

• The sum of the current in an 80 cell shower box is the same for the FADC system as for the LeCroy peak sensing ADC system. Therefore the low energy tail could not be explained by an ADC specific error.

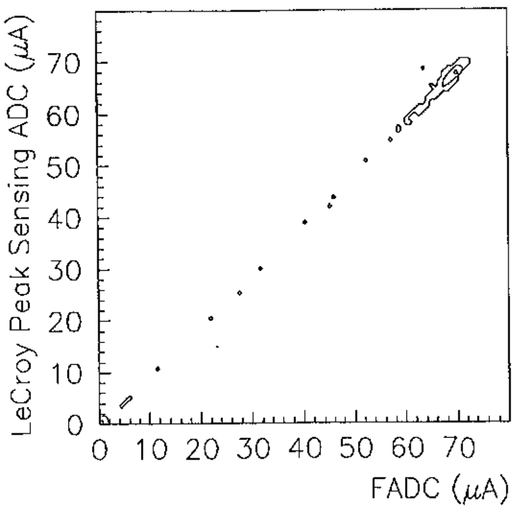

Fig. 5.7: Current summed in the 80 cells showerbox for two different ADC systems (FADC and LeCroy Peak Sensing system).

• The ratio of the initial current in a box of 3×3 cells around the cell with the highest signal to the initial current summed up in 80 cells showed a behavior comparable to a pure pion run.

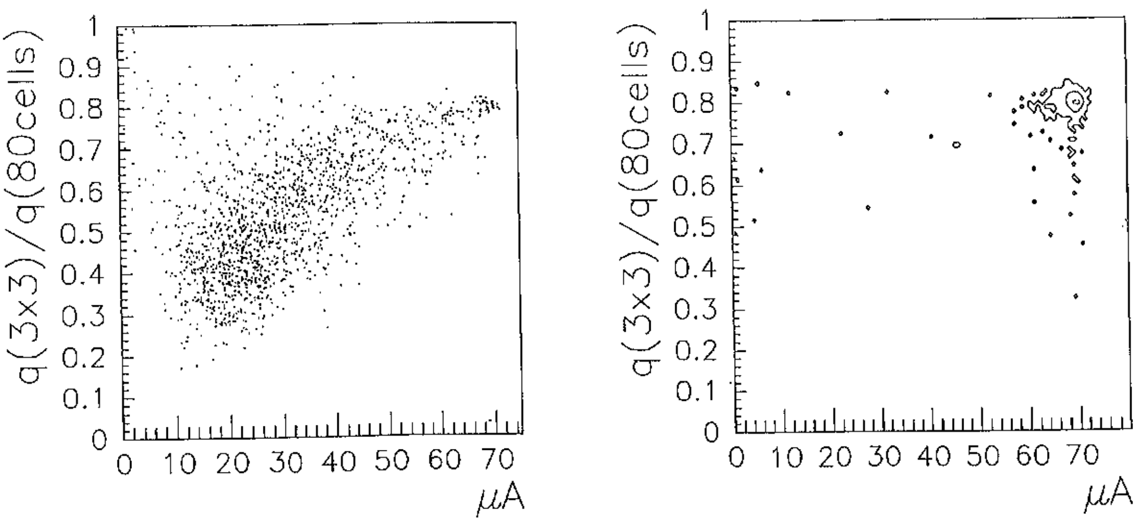

Fig. 5.13: Ratio of the current in a box of 3×3 cells around the cell with the maximum initial current to the initial current summed up in an 80 cell showerbox. The left plot shows a pure pion run, the right run shows the result of an electron run.

- The fraction of events in the tail decreased for runs with higher energies (from 2.0% for 35 GeV to 1.5% for 80 GeV) and for runs at higher intensities (from 0.7% for 1 ktrigger/burst to 0.3% for 50 ktrigger/burst).

The last two results suggest that the events in the tail are pions but no quantitative proof was found. The high pion contamination of the beam, which would be necessary to explain the low energy tail (approximately 4.5% pions), could be caused by the detuning of the electron beam to obtain the desired low rate for the second test. If this assumption is true the amount of events in the tail should decrease for higher energies and higher intensities, which could be observed in the data. To reach a definite conclusion in this question a Cherenkov counter will be used during the test in fall 1993.

Another hardware problem was the reason for additional non-Gaussian effects in the energy distributions of the first test. The improper measurement of the FADC clock phase (for 1% of the events one FADC sample was missing) led to a false shift of 25 ns away from the mean time of the amplitude. As the amplitude of each event was taken as the pulse height at the fixed mean time, the energy of the shower was underestimated for these events. This led to a small second peak at 85% of the real energy.

For the energy scan with the tilted calorimeter during the second test, the high voltage of the proportional chambers was switched off. Therefore events caused by muons could not be rejected. This led to a small peak at very low energies. It contained about 1% of the events remaining after all the cuts. The distribution was similar to the energy distribution obtained from dedicated muon runs.

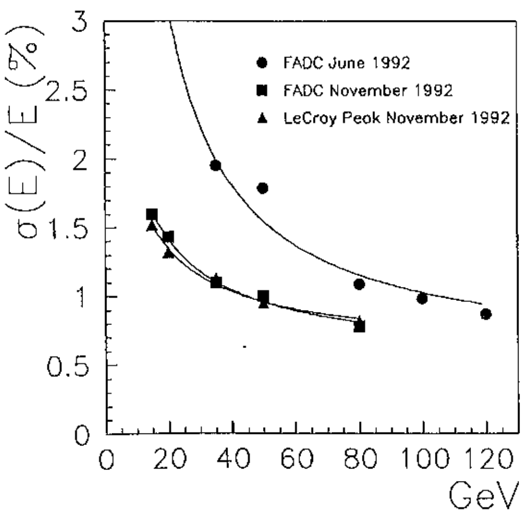

Fig. 5.14: Energy resolution as a function of the energy of the incoming electron.

The energy resolution as a function of the beam energy is shown in figure 5.14. A fit following (3.12) gives

$$\frac{\sigma(E)}{E} = \frac{7.1\%}{\sqrt{E[GeV]}} \oplus 0.52\% \oplus \frac{525MeV}{E[GeV]} \quad \text{(June 1992),} \tag{5.1}$$

$$\frac{\sigma(E)}{E} = \frac{5.4\%}{\sqrt{E[GeV]}} \oplus 0.57\% \oplus \frac{60MeV}{E[GeV]} \quad \text{(November 1992).} \tag{5.2}$$

For both equations the value of the last term, which is determined by the noise, was computed with the method explained above. These parameters were fixed in the fit. The fit can only give an approximation to the real behavior as the small number of points and the structure of the function made the fit procedure unstable.

For the second test, the energy resolution was also calculated for the LeCroy peak sensing ADC system for the same events and the same showerbox as for the FADCs. The results for both systems are of the same magnitude (fig. 5.14). For the first time the FADC system of the NA48 liquid krypton calorimeter prototype with 8 bit linear FADCs with 3 different gains was as good as a conventional 12 bit ADC system.

The mean values from the Gaussian fits to the energy distributions can be used to calculate the linearity of the liquid krypton calorimeter prototype. The measured energies for the tilted calorimeter are linear with respect to a fit with constant weight within less than 0.5% (fig. 5.15).

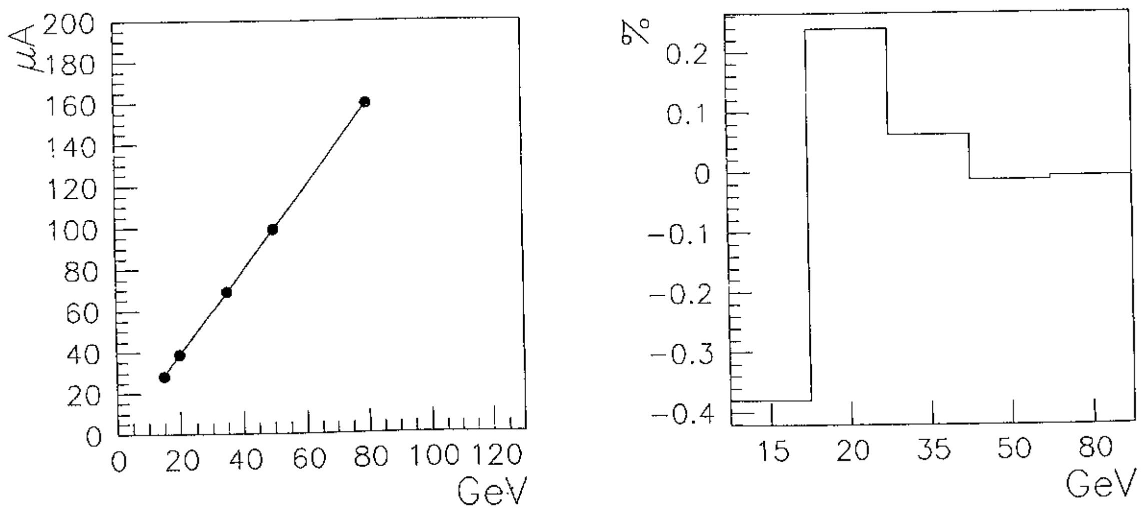

Fig. 5.15: Linearity of the energy response (tilted calorimeter, November 93). The right plot shows the deviation from the linear fit for the energies of the energy scan.

Results for the Second Test

The following investigations were only done for the data of the second test. Except from the trigger requirements used for the analysis of the energy resolution it was required that the energy in the 80 cells showerbox was within the peak of the energy distribution. Only events with an energy larger than 90% of the mean energy of a Gaussian fit to the distribution were taken.

Space Resolution

The impact point of the incoming particle was obtained from the center of gravity of the initial current in each cell at the position of the center of the particular cell. The center of gravity was computed in the showerbox of 80 cells that were equipped with FADCs and in a showerbox of 3x3 cells around the cell with the highest amplitude. The position had to be corrected by

$$x_{corr} = \lambda \ln\left(\frac{2x_{cog}}{d_{cell}F} \sinh\frac{d_{cell}}{2\lambda} + \sqrt{\left(\frac{2x_{cog}}{d_{cell}F} \sinh\frac{d_{cell}}{2\lambda}\right)^2 + 1} \right) \tag{5.3}$$

to count for the discrete cell structure of the calorimeter (fig. 5.16). The parameters λ and F had to be found from a fit to the data. A set of parameters was calculated for each coordinate direction and for each size of the showerbox in which the center of gravity was calculated. These parameter sets were common for all energies. The correction improved the resolution by a factor 2-5 depending on the size of the showerbox.

The space resolution was obtained from the width of the distribution of the difference of the center of gravity and the point, where the extrapolated track from the drift chambers had crossed the front of the calorimeter. The results for the space resolution are shown in figure 5.17. The distribution shows small non-Gaussian tails after the normal trigger requirements and the additional demand for the total energy in the peak of the energy distribution. Less than 0.5% of the events had a difference greater than 0.5 cm between corrected center of gravity and impact point from the drift chambers.

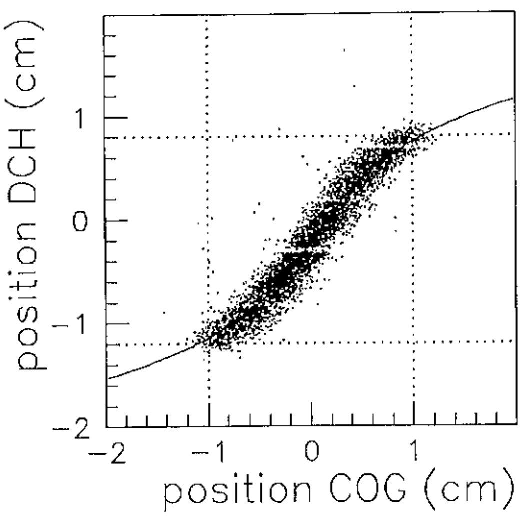

Fig. 5.16: Non-linear relation between the uncorrected center of gravity and the impact point as reconstructed with the drift chambers. The line shows the fit using (4.7).

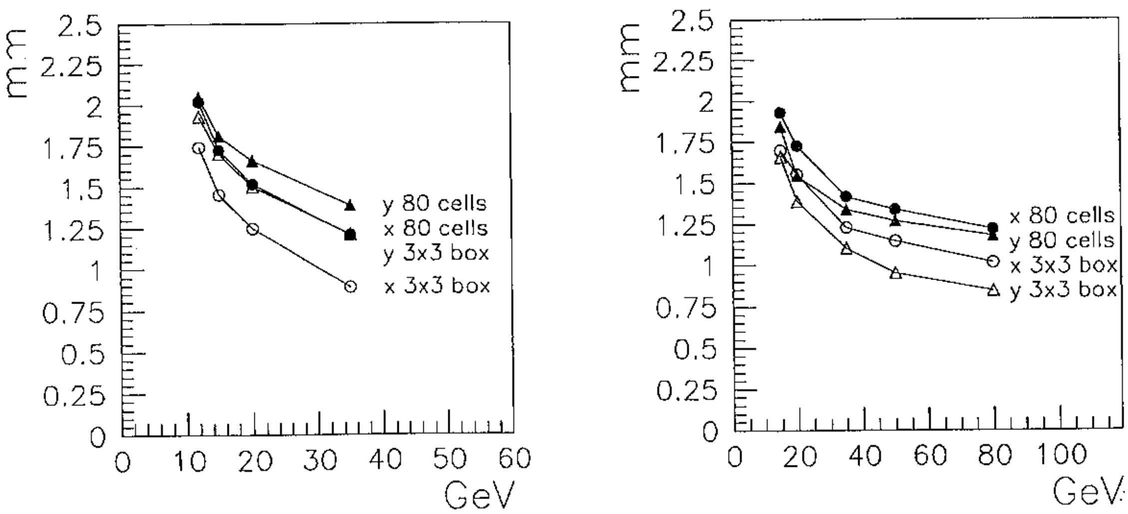

Fig. 5.17: Space resolution of the center of gravity as a function of the beam energy for different showerbox sizes. The left plot shows the results for a calorimeter parallel to the beam. The right plot shows the results for a tilted calorimeter.

The space resolution was computed for runs during which the calorimeter was tilted, and also for runs during which the calorimeter was parallel to the beam. The space resolution for the x-coordinate is worse in the case of a tilted calorimeter, as the shower spreads over more cells in this direction. Again the results are of the same order of magnitude as for the LeCroy peak sensing ADC system [Coll12/92].

Time Resolution

Different methods were used to calculate the time resolution of the calorimeter. In the first approach, the time of the maximum ACF was taken. Better results were achieved by determining the time at which the signal reached half the maximum amplitude. For each approach, the time for each event was taken from the highest not saturated FADC gain type of the cell with the highest pulse height. Both resolutions improved after taking the weighted mean of the times from the nine cells of a 3×3 cells box around the cell with the highest signal. The squared value of the pulse height in the particular cell was used as the weight. All results were corrected for the pulse height dependence. The spectrum for each FADC was divided into slices of 5 LSB and a mean time for each slice was calculated (fig. 5.18). The mean time was subtracted from the computed time of each event. The method also corrects for cell-to-cell differences in the timing, which can be up to 25 ns (fig. 5.19).

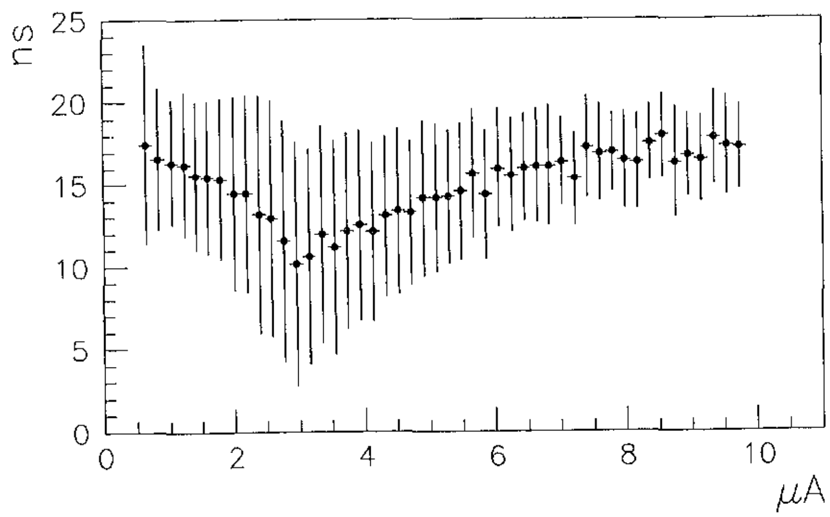

Fig. 5.18: Time of the amplitude as obtained from the ACF as a function of the amplitude (electron data, November 92).

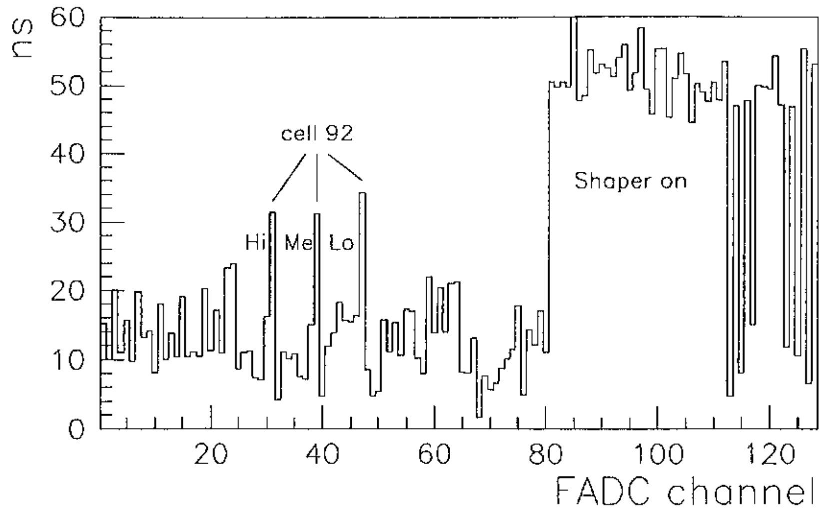

Fig. 5.19: Channel to channel differences of the time of the amplitude as obtained from the ACF. Note the similar behavior for FADC channels of different gain, which were connected to the same calorimeter cell. The use of the shaper amplification (×6) delayed the signal by about 40 ns.

To obtain the time at half the maximum amplitude, the peak of the signal was reconstructed using a parabola through the largest data sample and the two adjacent samples. The time of the intersection of a parabola through three points at the leading edge with the level at half the amplitude was taken as the time information for this event.

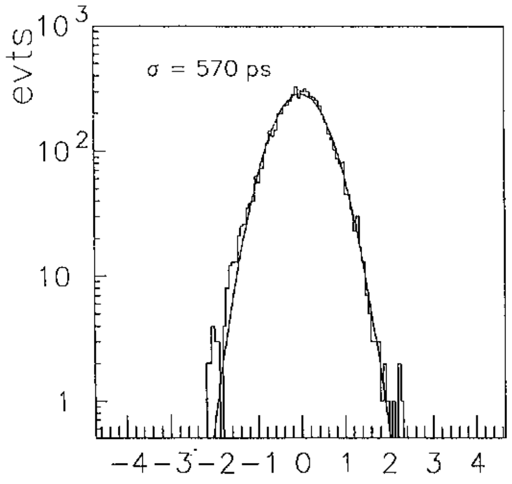

Fig. 5.20: Time distribution for the time at which half the amplitude is reached. The time is the weighted average in a 3x3 cells box (35 GeV).

The resulting time distributions showed no non-Gaussian tails, if all trigger conditions were required and only events with a total energy greater than 90% of the mean energy of the peak of the energy distribution were used (fig. 5.20).

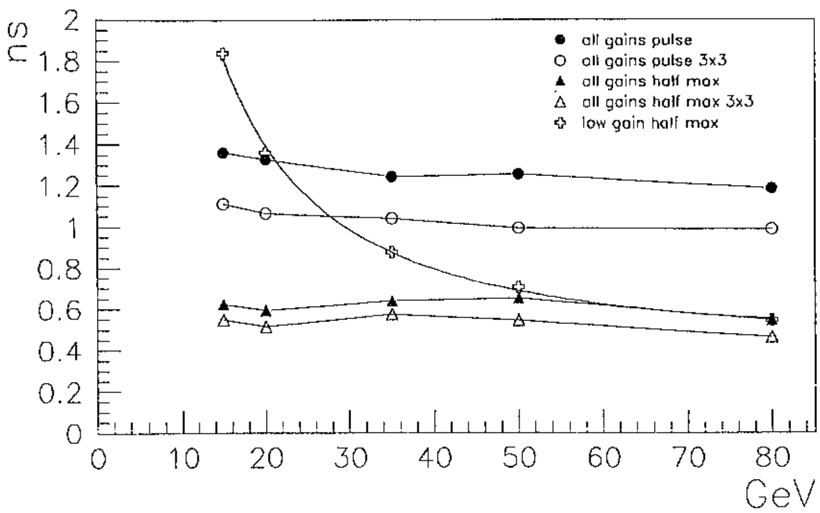

Fig. 5.21: Time resolution of the calorimeter as function of the beam energy. The two upper curves give the time resolution for the whole pulse obtained from the ACF, whereas the other curves show the time resolution of the time at which half the amplitude is reached. '3×3' denotes the weighted average of the time in a 3×3 cells box around the center cell of the shower. The fit for the low gain FADC is explained in the text. Other lines are simply to guide the eye.

To understand the sharp limitation of the time resolution without any improvement for higher energies one has to keep in mind that the FADC gain type in the center cell of the shower changes with the energy. For high energies the time resolution for all gain types behaves similarly to the time resolution for the low gain FADC. At these energies at least one FADC had to be a low gain FADC. With decreasing energies the time resolution of the low gain FADC alone deteriorates, whereas the time resolution for all gain types remains stable. For these energies more and more medium FADCs can be used for the center cell of the shower.

The time resolution for the low gain FADC can be fitted with

$$\sigma_{time} = \frac{26.4ns}{E[GeV]} \oplus 434ps. \tag{5.4}$$

The 1/E term in the fit can be estimated from the noise in the FADC system. From the average pulse in figure 4.12 the slope of the rising edge can be approximated by

$$slope = \frac{35\% \cdot amplitude}{25ns} . \tag{5.5}$$

Assuming that on average one third of the energy of the incoming particle is deposited in the center cell (in reality 20%—50% depending on the impact point of the particle) the slope is given by

$$slope = \frac{7}{1500ns} E_{beam} \,. \tag{5.6}$$

The time resolution can now be estimated from the noise of one low gain channel $\sigma_{noise} = 47MeV$ (tab. 5.1)

$$\sigma_{time} = \frac{\sqrt{2}\sigma_{noise}}{slope} = \frac{14.2ns}{E[GeV]} \tag{5.7}$$

which is in the order of magnitude of the fitted result. The factor $\sqrt{2}$ was used to consider the error on the knowledge of the amplitude and of the rising edge.

Contributions to the constant term of the time resolution come from the time resolution of the trigger signal (180 ps) and from the uncertainty of the clock phase measurement with the TDC (about 100 ns). Still, these contributions cannot explain the high value for the constant term of the time resolution.

Non-uniformity of the Calorimeter Response

The measured energy shows a dependence on the impact point in the x-coordinate, perpendicular to the electrodes (fig. 5.22).

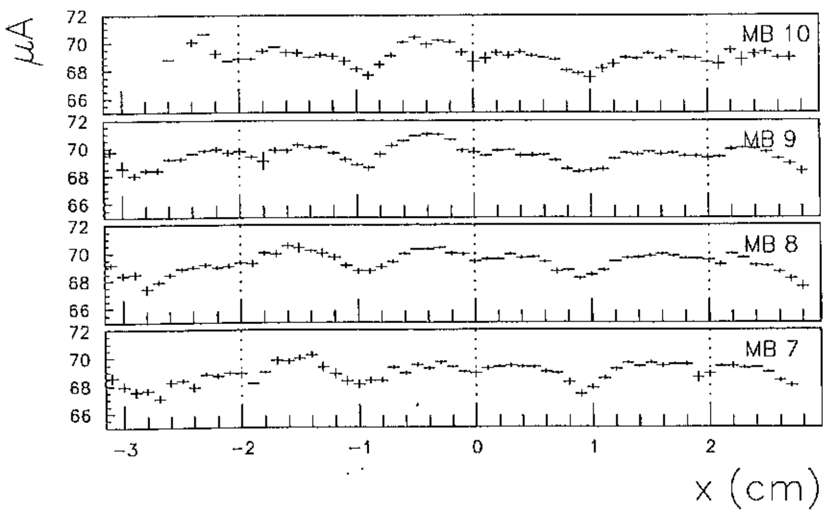

Fig. 5.22: Non-uniformities in the energy response of the non-tilted calorimeter for different motherboards (MB). The positions of the anodes are ...,-3,-1,1,3,... cm, the positions of the cathodes are ...,-2,0,2,... cm.

Two different types of non-uniformities can be distinguished:

- Left-right asymmetries: The response depends on whether the particle hit the left or the right half-cell. One possible explanation is a misplacement of the foils, which leads to different capacitances of the two half-cells. Left-right asymmetries decreased after the insertion of additional spacers between the foils to define their position more accurately.

- Dips at the position of the foils: They are deeper for the readout foils at the center of the cell (3% energy loss), smaller at the high voltage foils at the edge of the cells. The depth of the dips decreased after turning the calorimeter by a small angle (26 mrad) whereas the width increased.

The variation of the energy response in the y-direction shows a small non-uniformity. One possible explanation could be the miscalibration between different motherboards due to the incorrect extrapolation of the resistance of the FET in the calibration circuit. No patterns periodic with the dimension of the cell structure could be found.

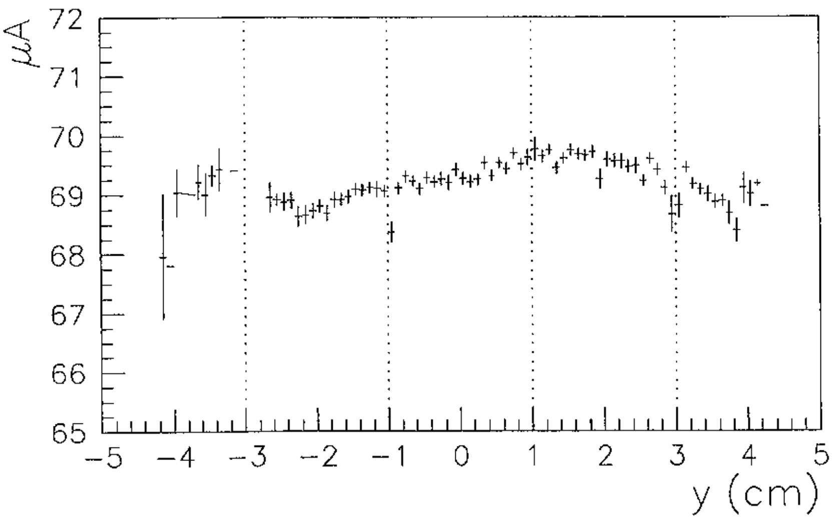

Fig. 5.23: Non-uniformity in the y-direction in the energy response of the calorimeter, averaged in the x-coordinate. Cell edges are at ...,-3,-1,1,3,... cm.

The time of the signal and the signal shape is also dependent on the impact point of the particle. The dependence of the time at half maximum and of the FWHM of the pulse on the x-coordinate is shown in figure 5.24 and figure 5.25. For the time information a regular pattern in the y-coordinate was also observed (fig. 5.26). The reason for this behavior will be explained in the next section. For all plots a pulse height correction was applied. This decreased pulse height effects as the amplitude itself was position dependent.

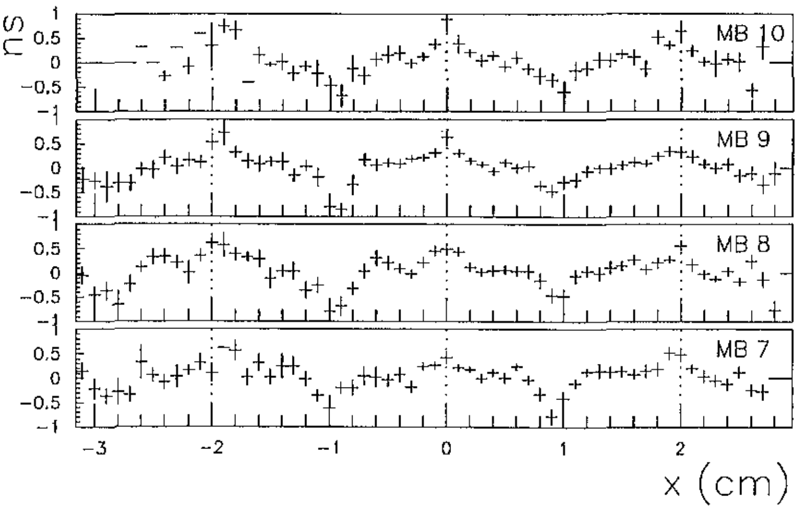

Fig. 5.24: Non-uniformity of the time at half of the amplitude for different motherboards (MB). The positions of the anodes are ...,-3,-1,1,3,... cm, the positions of the cathodes are...,-2,0,2,... cm.

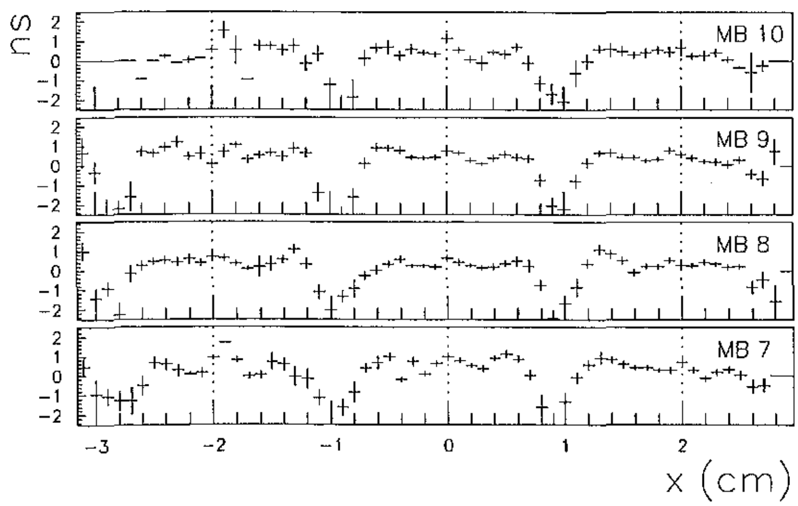

Fig. 5.25: Non-uniformity of the full width at half maximum (FWHM) for different motherboards (MB). The positions of the anodes are ...,-3,-1,1,3,... cm, the positions of the cathodes are...,-2,0,2,... cm.

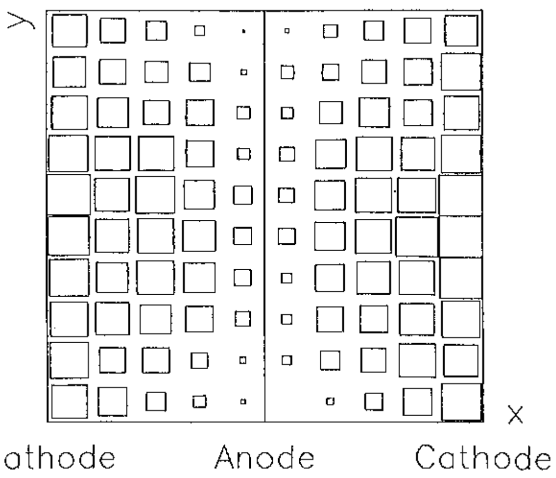

Fig. 5.26: Time dependence on the impact point in the cell. The plot is the average of all cells in the calorimeter. Larger boxes show later times.

Charge Collection Effects

Waveform Analyzer Studies

To understand the non-uniformity effects in the calorimeter, the preamplifier output was studied with a waveform analyzer (WFA). This device, a LeCroy LRS 6841 waveform analyzer, has a resolution of 8 bit and was programmed to record the signal with a frequency of 50 Msamples/s. It was connected with a Tektronix P6201 high impedance FET probe to the preamplifier output of one cell. The cell to which the probe was connected was changed after several runs. An example for a typical signal is given in figure 4.44. The signal was recorded with a pedestal of 30 LSB and an offset of 80 time samples. The whole time window recorded with the WFA was 256 time samples or 5.12 μs long. In total 3.5 μs of the signal was recorded.

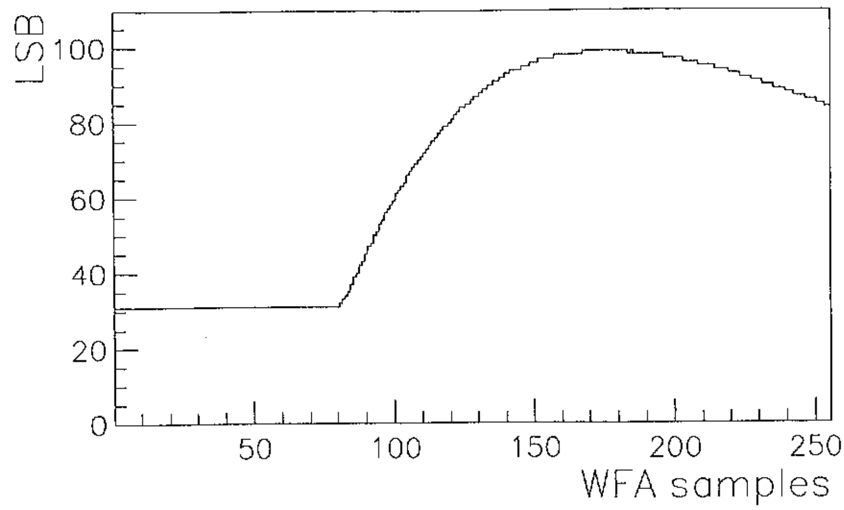

Fig. 5.27: Example of a preamplifier output pulse as recorded with the waveform analyzer.

The noise of the WFA was obtained from the distribution of samples before the start of the pulse, which contained only pedestals (fig. 5.28). The RMS of this distribution was about 0.8 LSB.

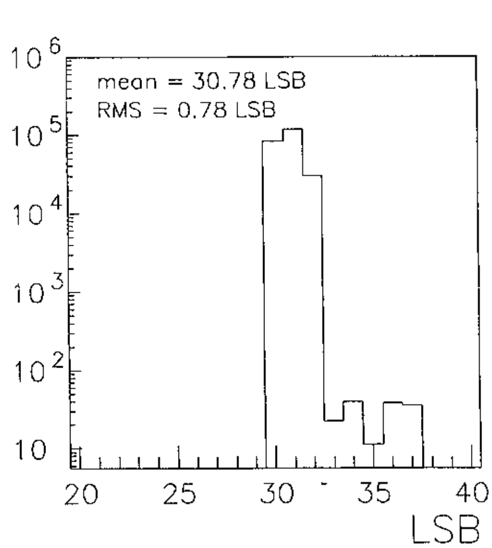

Fig. 5.28: Noise of the waveform analyzer.

The main item of the analysis was the time in which the maximum of the preamplifier output pulse was reached (peaking time). For a given shape of the input current into the preamplifier, the peaking time remains constant and does not depend on the amplitude of the input current. Any fluctuation of the peaking time indicates a deviation from the original shape of the input current.

Unfortunately, the resolution of the WFA was not sufficient to determine the time of the maximum unambiguously, since the maximum extended over up to 100 samples for lower amplitudes below 5 μA initial current. Therefore the pulse was scanned once from the beginning to the end to search for the first maximum and then scanned in the reverse direction to find the last sample with the maximum value. The peaking time was taken as the mean value of the time of the first and the time of the last sample with the value of the maximum. The fluctuation of the pulse height over the plateau was not larger than 1 LSB. Due to the asymmetric shape of the preamplifier output pulse, the calculated peaking time overestimates the real peaking time for longer plateaus. Still it gives a much better approximation than the time of the first maximum.

The peaking time in dependence of the impact point of the electron (which was reconstructed with the center of gravity) was studied (fig. 5.29).

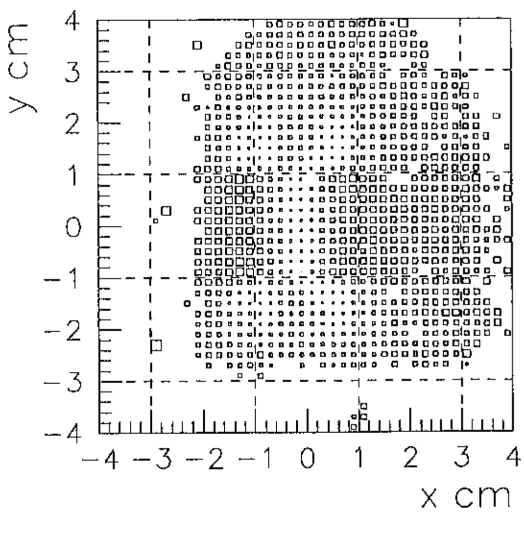

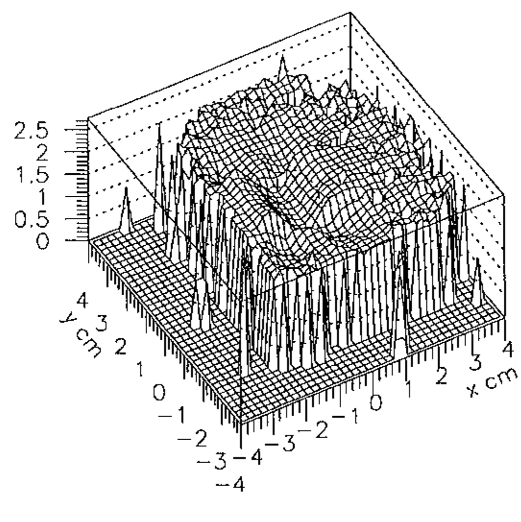

Fig. 5.29: Peaking time as a function of the impact point. The cell with the WFA has the coordinates -1 cm < x < 1 cm and -1 cm < y < 1 cm. The left plot shows a box plot, where larger boxes show later peaking times. The right plot shows a surface plot, where the z-coordinate gives the peaking time. The plots are asymmetric with respect to the cell axis, as they show the result from a run with a tilted calorimeter.

A strong effect is observed, whenever the impact point of the electron is in the cell which is connected to the WFA. The signal peaks earlier, if the impact point is near the anode and later, if it is near the cathode. This effect indicates a more convex shape of the input current for the first case and a more concave shape in the latter case. If the impact point lies in the cells left or right of the cell with the WFA, the peaking time remains constant. To check the shape of the input current, it has been reconstructed by deconvolution of the preamplifier output signal using the ideal preamplifier response function. Unfortunately this could not be done event by event because the resolution of the signal digitization by the WFA was not sufficient. Therefore only the sum of the deconvoluted signals for all events, in which the electron had hit certain regions of the calorimeter, has been calculated (fig. 5.30).

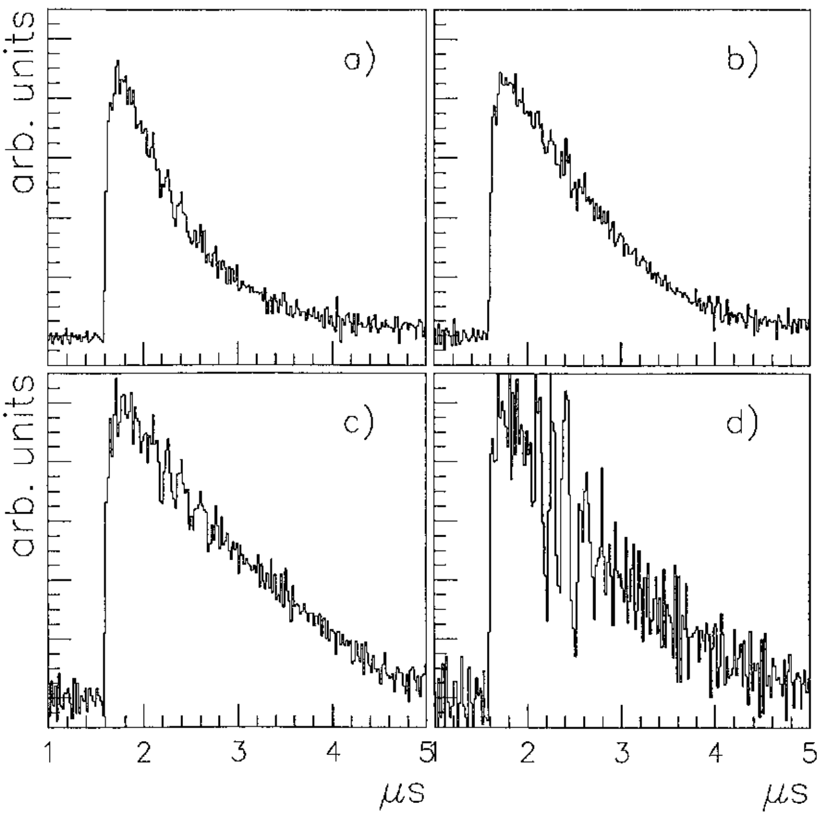

Fig. 5.30: Deconvoluted input current for different regions of the calorimeter. Only cells with the same y-coordinate as the cell with the WFA (left and right of it) were taken. a) -0.3 cm $< x < 0.3$ cm. b) ± 0.3 cm $< x < \pm 0.7$ cm. c) ± 0.7 cm $< x < \pm 1.3$ cm. d) ± 1.3 cm $< x$. The anode is at 0 cm and the cathodes are at ± 1 cm.

In the direction of the y-coordinate, an additional structure can be observed. In the cell with the WFA connected, the preamplifier signal has the largest peaking time if the electron hits in the corner of the cell, near the cathode and in the region near to the adjacent cells (in electrode direction). In these adjacent cells, the V-shape is reversed with respect to the behavior in the cell with the WFA. The signal peaks later, if the electron hits near the anode and earlier for impact points close to the cathodes.

Tilting of the calorimeter decreases the depth of the V-shape, which is also an indication for smaller non-uniformity effects (fig. 5.31). In the tilted case, the shape becomes asymmetric. It is shifted by 2 mm and the latest peaking times are different in the cells left and right of the cell with the WFA. The difference between the latest peaking times on the two sides is about 100 ns.

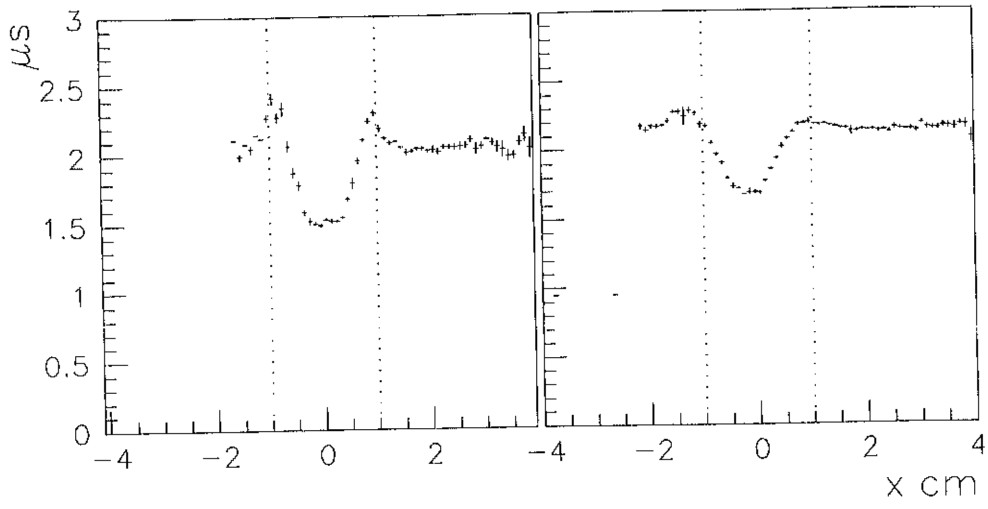

Fig. 5.31: Peaking time for cells with the same y-coordinate as the cell with the WFA (cells left and right of it). The left plot shows the results in the case of the non-tilted calorimeter. The right plot shows the results for a tilted calorimeter (26 mrad).

Simulation of Charge Collection Effects

To understand the reason for the observed effects in the peaking time of the preamplifier output signal, the charge collection in a system of parallel plate capacitors of finite size was simulated. In this analysis, a different approach to the normal weighting field method was used, which gave qualitatively the same results. Exploiting the fact, that the 1 mm gap between two strips on one foil is small, the analytical solution for the charge density on one plate of a parallel plate capacitor of infinite size [Fon67]

$$\rho(r)_{x=L} = \frac{q}{\pi L}\sum_{n}\frac{n\pi}{L}(-1)^n \sin\left(\frac{n\pi x_0}{L}\right)\mathrm{K}_0\left(\frac{n\pi r}{L}\right) \tag{5.8}$$

was used. x_0 denotes the distance of the charge inducing electron to the electrode at x=0 and K_0 is the modified Bessel function of zero order. The charge density on the plate was integrated between $\pm\infty$ in one direction and in strips of 20 mm in the second direction for different positions of the drifting electron (fig. 5.32).

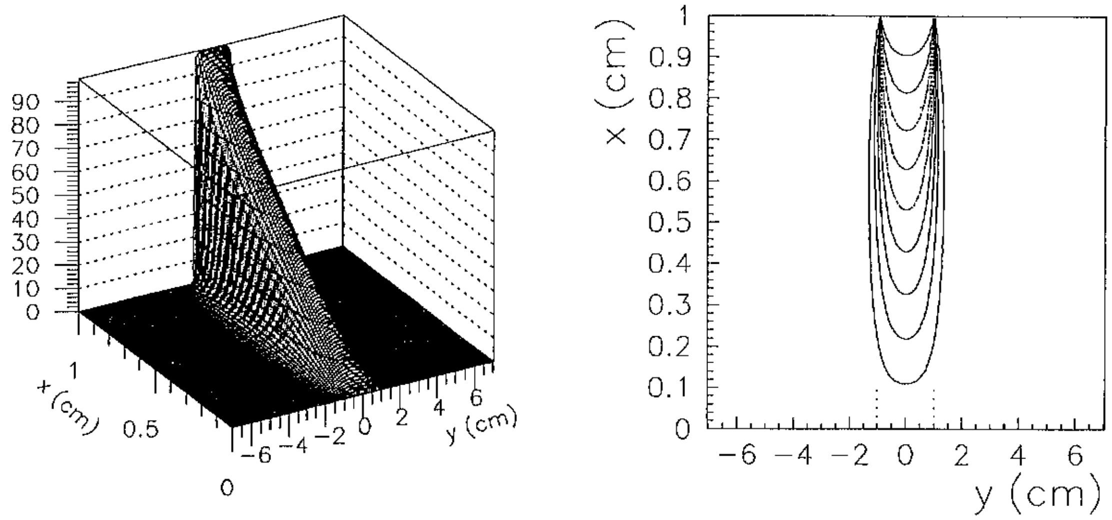

Fig. 5.32: Charge induced by a point charge on one strip on one plate (x = 1 cm) of a parallel plate capacitor. The strip is at x = 1 cm and -1 cm < y < 1 cm. The x- and the y-coordinate give the position of the charge carrier. For each point the charge induced on the strip is shown by the height of the histogram. The width of the strip is shown by the two lines at the bottom. (Note different scales for x and y).

The difference of the charge induced on the strip between two consecutive positions of the drifting electron was calculated. Thus a function was obtained that, after multiplication with the drift velocity, describes the current induced by a single drifting electron (fig. 5.33). For a parallel plate capacitor of infinite size, the current induced by a single drifting electron has a rectangular shape. The simulated current induced on a strip of finite size shows a different behavior. It increases with the proximity of the drifting electron to the strip, if the electron is produced in the gap of the same strip. If the electron is produced in an adjacent cell it induces a current in the electrode, which is positive for larger distances but decreases and even gets negative for smaller distances[7] (fig. 5.34).

---

[7] Another study of edge effects in ionization chambers with similar results as in this analysis can be found in [Ros49].

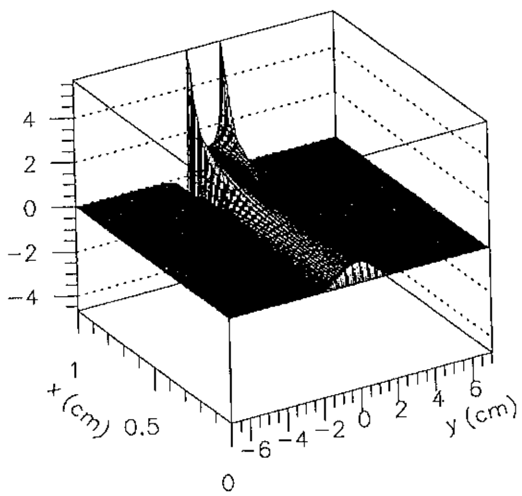

Fig. 5.33: Change of the charge induced by a drifting point charge on one strip on one plate (x = 1 cm) of a parallel plate capacitor. The strip is at x = 1 cm and -1 cm < y < 1 cm. The point charge moves in the gap parallel to the y-axis toward the plate at x = 1 cm. The height of the histogram shows the difference of the charge induced on the strip between two consecutive positions of the point charge. The last position gives the coordinate of the histogram. The input current to the preamplifier can be obtained by multiplication with the drift velocity. (Note the different scale for x and y).

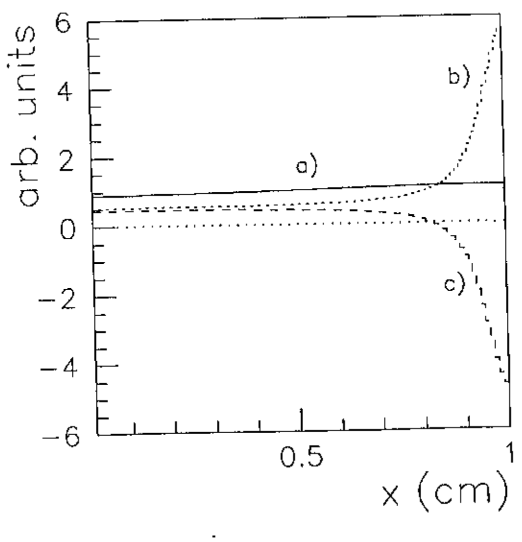

Fig. 5.34: Change in the charge induced by a drifting point charge on one strip on one plate (x = 1 cm) of a parallel plate capacitor. This plot shows slices from the previous figure which correspond to the currents induced by charge carriers drifting in the gap. a) The charge carrier moves in the center of the cell. b) The charge carrier moves at the edge of the cell, but still inside. c) The charge carrier moves at the edge of the cell, already in the next cell.

The shape of the input current in one cell produced by a whole shower was computed by adding the current induced by single electrons starting their drift at all points in the two gaps of the cell. Each single electron current was weighted with the charge density produced by the shower at its starting point. The radial charge density used for this calculation was obtained from an EGS Monte Carlo simulation adapted to compute the energy deposition in concentric rings of constant area.

The preamplifier output signal was obtained from a convolution of the input current with the preamplifier response function. The resulting dependence of the preamplifier peaking time is given in figure 5.35. It is in good agreement with the data. The V-shape of the peaking time dependence on the direction perpendicular to the electrodes and also the latest peaking times in the corners of the cell are reproduced. In the adjacent cells, the opposite behavior is observed, later peaking times close to the anode, earlier peaking times close to the cathode.

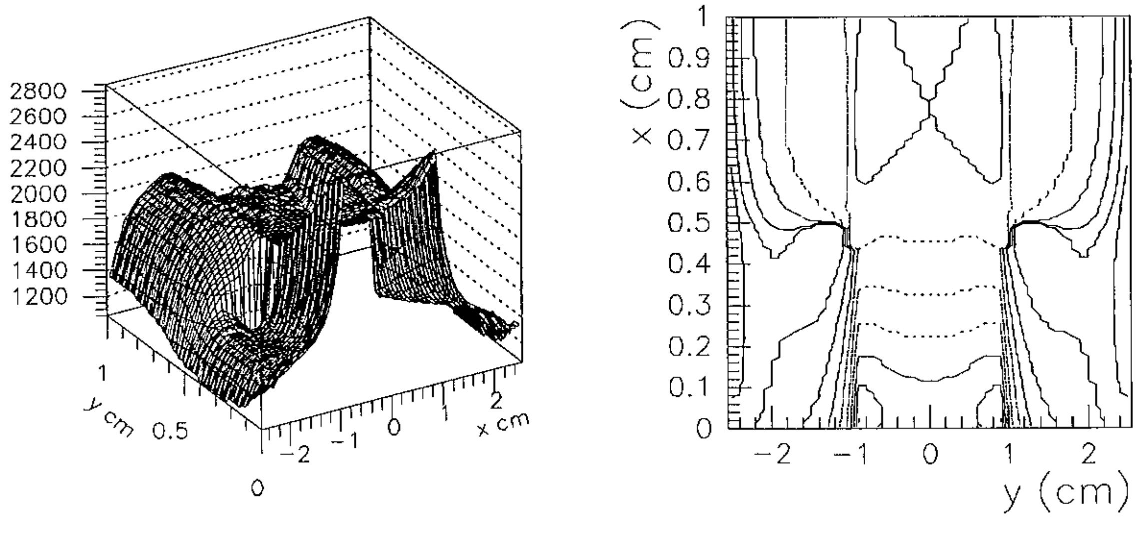

Fig. 5.35: Peaking time of the simulated preamplifier output signal in one half-cell as a function of the center of the charge distribution. The strips end at -1 cm and 1 cm in the y-coordinate. (Note the different scale for x and y).

The sudden change in the response of the peaking time at the border between two cells can be understood from the shape of the input current to the preamplifier (fig. 5.36). Near the edge of the cell, a small second peak in the input current appears. It comes from the peaks of figure 5.33, at the time when the drifting charge produced by the center of the shower reaches the anode. Crossing the border between the two cells this second peak turns down and causes an earlier peaking time.

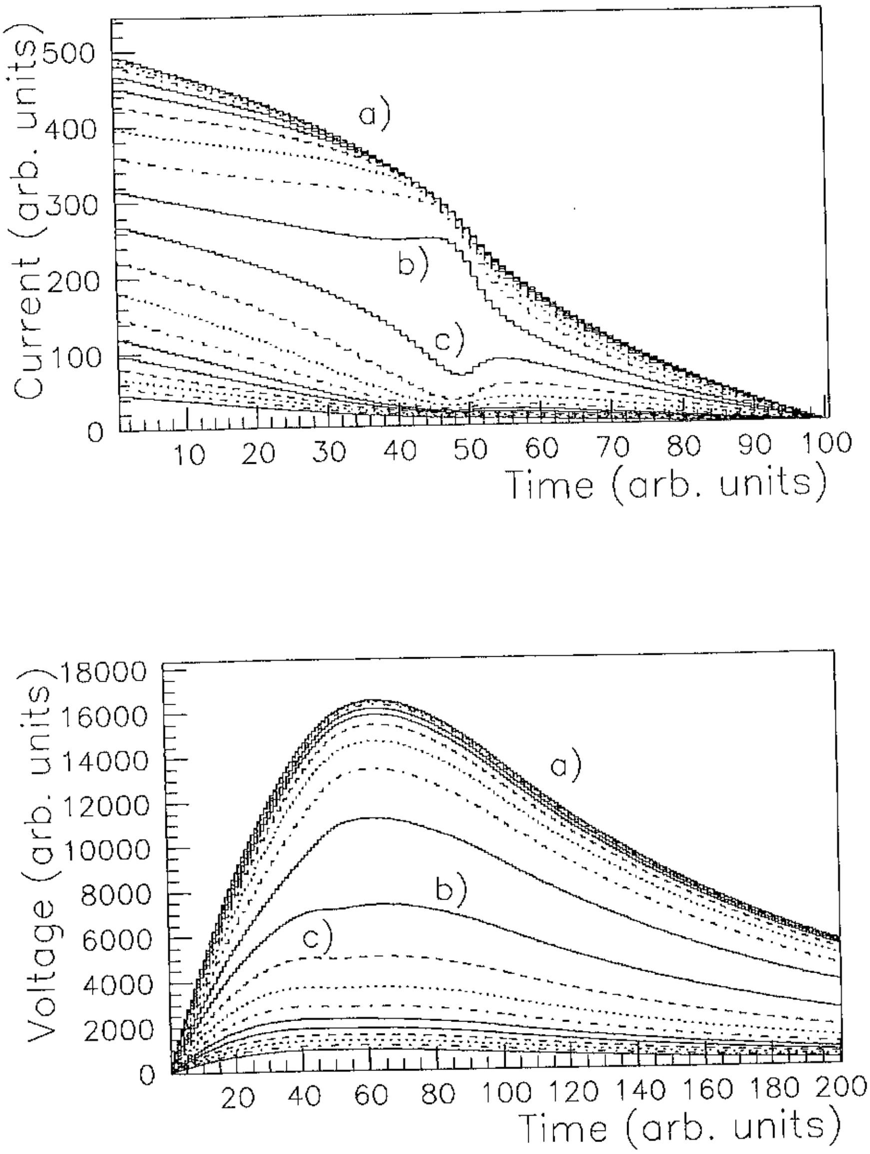

Fig. 5.37: Simulated input currents (upper plot) and the resulting output signals of the preamplifiers (lower plot) for different positions of the center of the charge distribution in the x-coordinate (direction of the electrodes). In the y-direction (perpendicular to the electrodes) the center of the charge is at half the width of the gap. The highest current is produced by an electron hitting in the center of the cell. The input current is decreasing, if the impact point is moving away from the center of the cell. If the impact point is near the edge of the cell there is a second peak with different orientation for impact points in- and outside the cell. a) The impact point of the electron is in the center of the cell. b) The impact point of the electron is at the edge of the cell, but still inside. c) The impact point of the electron is at the edge of the cell, already in the next cell.

In reality the peaks for electrons at the edges of the cells are smaller than in the simulated currents as the use of the analytical solution of the charge on one plate of a plate capacitor neglects the finite distance between adjacent strips. A detailed Monte Carlo study of the zig-zag calorimeter structure using the virtual weighting field method as well as position-dependent drift velocities was completed meanwhile. This simulation yielded a sampling term of $3\% / \sqrt{E}$ for the energy resolution of the calorimeter [Coll4/93].

The different slope of the input current during the integration time of the shaper is also the reason for the non-uniformity of the time response of the calorimeter from the analysis of the FADC data (fig. 5.26). The shaper output signal peaks earlier, if the falling slope of the current from the calorimeter cell is less negative or even positive. Therefore events with impact points near the upper or lower edge of the cells have an earlier peaking time of the shaper output signal. This effect is stronger near the anode foils, as the additional peak in the input current is closer to the integration interval of the shaper.

Electron Lifetime in the Calorimeter Prototype

The simulated input current to the preamplifier can be used to obtain an estimate for the lifetime of the electrons in the calorimeter prototype. The real input current should be equal to the simulated one with a falling exponential function superimposed, which is given by the finite lifetime of the electrons. In the following, the steps which were taken to compare the two cases are described. The cell with the WFA was divided into five regions, each 2 mm wide in the x-coordinate and 2 cm high in the y-coordinate. The deconvoluted current was calculated from the test beam data as for the plots in figure 5.30. In parallel, the simulated input current was averaged over the same regions. The shapes of the calculated and the simulated currents were compared region by region. In a fit of the simulated current to the calculated current, the simulated current was adjusted in amplitude and time to obtain the best agreement.

$$f(t) = \begin{cases} p_4 & ,t < p_1 \\ p_4 + p_5 \dfrac{t}{p_3 - p_1} f_{sim}(t) e^{-t/p_6} & ,p_1 > t > p_3 \\ p_4 + p_5 f_{sim}(t) e^{-t/p_6} & ,p_3 > t > p_1 + p_2 \\ p_4 & ,t > p_1 + p_2 \end{cases} , \qquad (5.9)$$

where the $p_{1,\dots,6}$ denote the fit parameters. The width of the time bins of the simulated data was scaled such, that the current was zero after a time corresponding to p_2, which gave the drift time of the electrons in the gap. The lifetime of the electrons is described by p_6. The parameter p_3 allowed for a finite risetime.

The main problem was the error due to the numerical differentiation necessary for the deconvolution of the WFA data. The pedestal following the pulse seemed to be higher than the pedestal before it. Unfortunately the time window provided by the WFA was not long enough to decide unambiguously where the pulse ended. A tail of the pulse affects the lifetime. A longer drift time (long tail) fakes a shorter lifetime, whereas a shorter drift time (short tail) leads to a longer lifetime. Therefore four different kinds of fits were done. For the first two fits, a fixed drift time has been assumed and used in the fit. These values were taken from previous measurements of the drift velocity of electrons in liquid krypton. As the measurements do not agree completely, the first fit was done with a drift time of 3.3 μs, calculated from the measurements of [Mil68]. The second fit used a drift time of 2.4 μs, which was obtained from [Yos76]. At 3 kV, the voltage used for the test beam data, this measurement is also in good agreement with the data measured by NA48 with the krypton used for the test beam [Min13/5/93]. For the third fit, the drift time and the lifetime were obtained from the fit, but only the first 2 μs of the pulse and the pedestal before it were used. For the last fit, all samples were taken. An example for each fit is given for the region $0.6\ \mathrm{cm} < x < 0.8\ \mathrm{cm}$ in figure 5.39. The fit with the drift time fixed to 2.4 μs does not describe the data. The results for the electron lifetime and drift time obtained from the four fit methods are shown in figure 5.38.

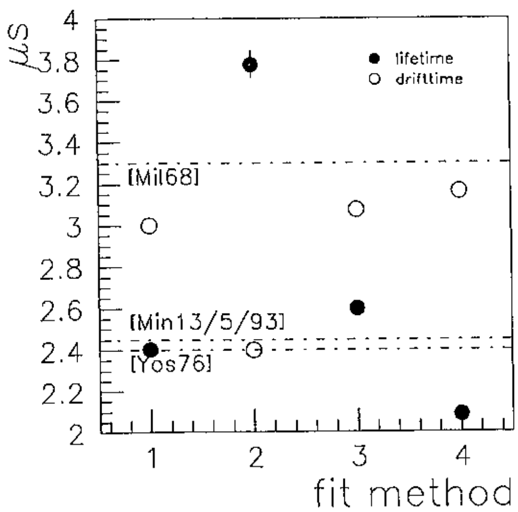

Fig. 5.38: Results for the lifetime and the drift time of drifting electrons from different fits of simulated current shapes to the data from the test beam.

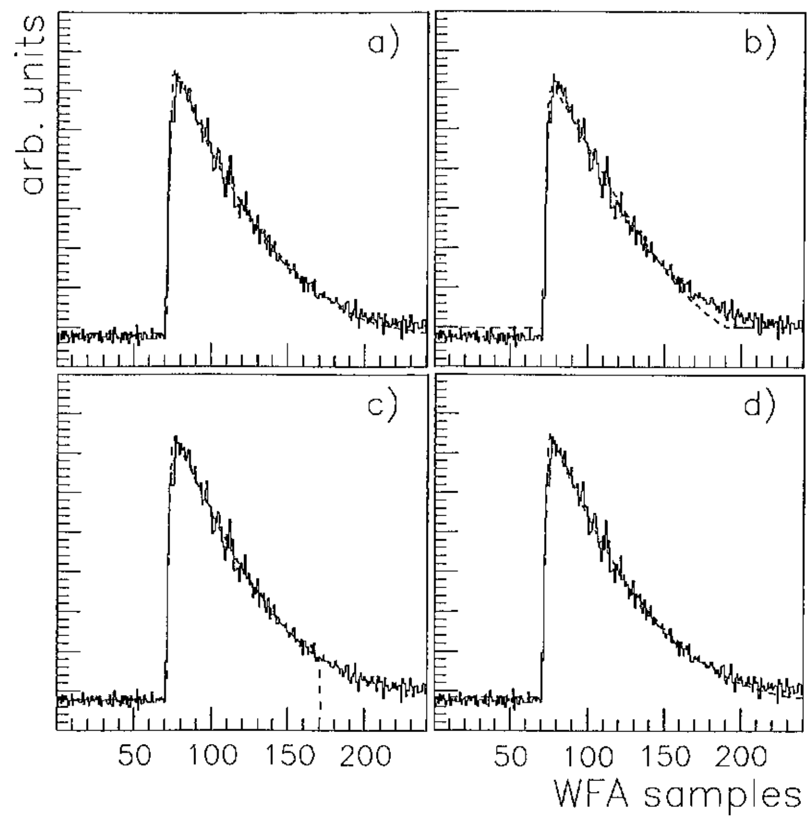

Fig. 5.39: Fit of the simulated current to the current obtained from the deconvolution of the preamplifier output signals. a) Fit with drift time fixed to 3.3 μs, all samples used. b) Fit with drift time fixed to 2.4 μs, all samples used. c) Fit with free drift time. Only the first 2 μs of the pulse and the pedestal before it were used. d) Fit with free drift time, all samples used.

The lifetime obtained with this method is only a lower limit. The shape of the current from the deconvoluted preamplifier output is affected by many parameters, where the main contribution comes from the resolution of the center of gravity. This leads to a decrease of the bumps in the current shapes, which fake a shorter lifetime. This effect is difficult to estimate. To conclude, the lifetime of electrons in the liquid krypton of the calorimeter prototype was certainly longer than 2 μs and most probably even longer than 2.5 μs.

Charge Collection Effects and Non-uniformities

The non-uniformities in the energy response of the calorimeter can now be understood as the consequence of the charge collection effects in connection with the highly non-uniform ionization in the gaps of the calorimeter.

The energy resolution is influenced by the changing amount of charge that is produced in the region near the anodes. Electrons that reached the anode before the end of the integration time of the shaper give a smaller contribution to the signal. Signal induction in adjacent cells does not directly contribute to the energy resolution as the energy is summed in all cells of the showerbox. However, the error of the measurement is increased due to miscalibrations between different motherboards. As a consequence of these effects, each drifting electron produced in a shower is measured with a position-dependent weight.

In principle, a correction depending on the impact point of the incoming particle is possible. However, this correction can only improve the constant term of the energy resolution. Fluctuations in the lateral energy distribution still influence the sampling term of the energy resolution.

The space resolution suffers from the same problems as the energy resolution. Additional problems arise from the spread of the induced charge in the direction parallel to the electrodes. This is the reason that for a non-tilted calorimeter the space resolution is worse in this direction than in the direction perpendicular to the electrodes.

The impact of charge collection effects on the time resolution have already been discussed. Again a position-dependent correction would be possible. However, it is questionable, whether this correction is necessary. The correction will be difficult due to the two-dimensional structure of the dependence and the required time resolution is already reached without this correction.

All effects are decreased in the case of a tilted calorimeter. However, the correction of the remaining non-uniformities will be difficult, as the intersection of the shower with the cells of the calorimeter leads to a non-trivial dependence of the correction factors on the energy.

Chapter 6: Summary

The two main items of this analysis were the study of the capabilities of the FADC system in respect of energy, space and time resolution and the reasons and consequences of the non-uniformities in the calorimeter response.

The quantitative results of this analysis are summarized in table 6.1.

	Proposal	FADC June 92	LRS Peak November 92	FADC November 92
Noise per cell	3 MeV/cell	60 MeV/cell	4 MeV/cell	6 MeV/cell
Energy resolution $\frac{\sigma}{E} = \frac{c_1}{\sqrt{E}} \oplus c_2 \oplus \frac{c_3}{E}$	$c_1 = 3\%$ $c_2 = 0.5\%$	$c_1 = 7.1\%$ $c_2 = 0.52\%$ in 72 cells, non-tilted	$c_1 = 5.4\%$ $c_2 = 0.57\%$ in 80 cells, tilted	$c_1 = 5.6\%$ $c_2 = 0.54\%$ in 80 cells, tilted
Space resolution	$\sigma = 1$ mm			
tilted			$\sigma_x = 1.55$ mm $\sigma_y = 1.4$ mm	$\sigma_x = 1.7$ mm $\sigma_y = 1.65$ mm
non-tilted			$\sigma_x = 1.25$ mm $\sigma_y = 1.45$ mm	$\sigma_x = 1.45$ mm $\sigma_y = 1.7$ mm
Time resolution	$\sigma = 1$ ns			$\sigma = 0.6$ ns

Tab. 6.1: Results of the Analysis and the values required by the NA48 proposal.

The results of the analysis can be summarized by the following statements:

- The results for the energy and the space resolution of the liquid krypton calorimeter prototype using a FADC system consisting of 8 bit linear FADCs grouped in two or three different gain types were compared to the results of a conventional peak sensing ADC system with 12 bit linear resolution. For the FADC system with three different gains as used in November 1992 a similar result was reached, if the same showerbox was used[8].

[8]The best result for the peak sensing ADC system in a showerbox of 11×11 cells and after the correction of non-uniformity effects was $\frac{\sigma(E)}{E} = \frac{4.7\%}{\sqrt{E}} \oplus 0.2\% \oplus \frac{50 MeV}{E[GeV]}$ [NA48/93].

For this analysis digital signal processing methods like auto correlation functions (ACF) and the reconstruction with ideally bandpass limited digital filters were used. These procedures avoided problems due to the asymmetry of the pulse shape and provided a tool to suppress events with distorted pulse shapes.
The space resolution was calculated from the center of gravity of the charge in the calorimeter, which had to be corrected for effects due to the discrete cell structure.
One important contribution to the energy and space resolution comes from the non-uniform response of the calorimeter.

- The time resolution of the calorimeter prototype is about 600 ps, independent of the energy. This time resolution was achieved for the time at which half the maximum amplitude is reached and is the weighted average of the times of a box of 3×3 cells around the center cell of the shower. To reach this result, cell-to-cell corrections of about 25 ns and pulse height dependent corrections of several nanoseconds needed to be applied. The limitation of the time resolution is given by non-uniformity effects.

- The non-uniformities in the calorimeter are caused by (1) miscalibrations between different half-cells and between different motherboards, (2) the highly non-uniform ionization in the longitudinal tower structure and (3) the mechanism of charge collection.
  A simulation of the charge collection of a non-uniformly distributed space charge was carried out, which gave results which are in good agreement with the effects observed in the test beam data.
  The use of a longitudinal tower structure is imposed by the particular requirements of the NA48 experiment. In a zig-zag shaped structure, as planned for the final experiment, non-uniformity effects will be decreased.

References

Chapter 1

[Alt81] I.S.Altarev et al.; A New Upper Limit on the Electric Dipole Moment of the Neutron; Phys. Lett. **102B**(1981)13.

[Ari92] K.Arisaka et al.; KTeV Design Report; Fermi National Accelerator Laboratories FN-580 (1992).

[Bur93] A.J.Buras, M.Jamin, M.E.Lautenbacher; The Anatomy of ε'/ε Beyond Leading Logarithms with Improved Hadronic Matrix Elements; MPI-Ph/93-11 CERN-TH-6821/93.

[Chi54] W.Chinowsky, J.Steinberger; Absorption of Negative Pions in Deuterium: Parity of the Pion; Phys. Rev. **95**(1954)1561.

[Chr64] J.H.Christenson, J.W.Cronin, V.L.Fitch, R.Turlay; Evidence for the 2π Decay of the K_L^0 Meson; Phys. Rev. Lett. 13(1964)138.

[Ciu93] M.Ciuchini, E.Franco, G.Martinelli, L.Reina; ε'/ε at the next-to-leading order in QCD and QED; Phys. Lett. **B301**(1993)263.

[Cro83] J.W.Cronin; CP Violation: Status and Prospects; Act. Phys. Pol. **B15**(1984)419.

[Dre68] W.B.Dress, J.K.Baird, P.D.Miller, N.F.Ramsey; Upper Limit for the Electric Dipole Moment of the Neutron; Phys. Rev. **170**(1968)1200.

[E731/93] L.K.Gibbons et al.; E731 Collaboration; Measurement of the CP-Violation Parameter $\mathrm{Re}(\varepsilon'/\varepsilon)$; EFI 93-06; subm. to Phys. Rev. Lett..

[Eic92] R.Eichler; Experimental Prospects for CP Violation Measurements; 1991-1992 Academic Training Programme, CERN.

[Fly89] J.M.Flynn, L.Randall; The Electromagnetic Penguin Contribution to ε'/ε for large Top Quark Mass; Phys. Lett. **B224**(1989)221.

[For84] E.N.Fortson, L.L.Lewis; Atomic Parity Nonconservation Experiments; Phys. Rep. **113**(1984)289.

[Fri57] J.I.Friedman, V.L.Telegdi; Nuclear Emulsion Evidence for Parity Nonconservation in the Decay Chain π^+-μ^+-e^{+*}; Phys. Rev. **105**(1957)1681.

[Frö91] J.Fröhlich, J.Heinrich, E.A.Paschos, J.-M.Schwarz; An Improved Estimate for Direct CP Violation; DO-TH 02/91 (1991).

[Gar57] R.L.Garwin, L.M.Lederman, M.Weinrich; Observation of the Failure of Conservation of Parity and Charge Conjugation in Meson Decays: The Magnetic Moment of the Free Muon; Phys. Rev. **105**(1957)1415.

[Gel55] M.Gell-Mann, A.Pais; Behavior of Neutral Particles under Charge Conjugation; Phys. Rev. **97**(1955)1387.

[Hei92] J.Heinrich, E.A.Paschos, J.-M.Schwarz, Y.L.Wu; Accuracy of the predictions for direct CP violation; Phys. Lett. **B279**(1992)140.

[Jar85] C.Jarlskog; A Basis Independent Formulation of the Connection Between Quark Mass Matrices, CP Violation and Experiment; Z. Phys. **C29**(1985)491.

[Kle76] K.Kleinknecht; CP Violation and K^0 Decays; Ann. Rev. Nucl. Sci. **26**(1976)1.

[Kob73] M.Kobayashi, T.Maskawa; CP-Violation in the Renormalizable Theory of Weak Interaction; Prog. Theor. Phys. **49**(1973)652.

[Lee56] T.D.Lee, C.N.Yang; Question of Parity Conservation in Weak Interactions; Phys. Rev. **104**(1956)254.

[Lee57] T.D.Lee, R.Oehme, C.N.Yang; Remarks on Possible Noninvariance under Time Reversal and Charge Conjugation; **106**(1957)340.

[Lee65] T.D.Lee, L.Wolfenstein; Analysis of CP-Noninvariant Interactions and the K_1^0, K_2^0 System; Phys. Rev. **138**(1965)B1490.

[Lee66] T.D.Lee, C.S.Wu; Decays of Neutral K Mesons; Ann. Rev. Nucl. Sci. **16**(1966)511.

[Lüd54] G.Lüders, Kgl. Danske Videnskab. Selskab, Mat.-fyss. Medd. **28**(1954)1.

[NA31/93] G.D.Barr et. al.; NA31 Collaboration; A New Measurement of Direct CP Violation in the Neutral Kaon System; to be published.

[Nac91] Nachtmann; Elementarteilchenphysik; Vieweg; ISBN 3-528-08926-1; p. 380-399, p. 437-447.

[Noe18] E.Noether; Invariante Variationsprobleme; Klg. Ges. d. Wiss. Nachr., Math.-phys. Kl., Göttingen. (1918)235.

[PDG92] Particle Data Group; Review of Particle Properties; Phys. Rev. **D45**(1992)Part 2.

[Pan51] W.K.H.Panofsky et al.; The Gamma-Ray Spectrum Resulting from Capture of Negative π-Mesons in Hydrogen and Deuterium; Phys. Rev. **81**(1951)565.

[Pas92] E.A.Paschos, Quark Mixing and CP Violation; DO-TH 92/6 (1992).

[Pau55] W.Pauli in: Niels Bohr and the Development of Physics (Pergamon Press, London, 1955) p. 30.

[Pen84] J.M.Pendlebury et al.; Search for a Neutron Electric Dipole Moment; Phys. Lett. **136B**(1984)327.

[Pla59] R.Plano et al.; Parity of the Neutral Pion; Phys. Rev. Lett. **3**(1959)525.

[Ram78] N.F.Ramsey; Dipole Moments and Spin Rotations of the Neutron; Phys. Rep. **43**(1978)409.

[Ram90] N.F.Ramsey; Electric Dipole Moment of the Neutron; Ann. Rev. Nucl. Part. Sci. **40**(1990)1.

[Sch53] J.Schwinger; Phys. Rev. **91** (1953) 720,723; **94**, 1366 formula (54) and 1576 discussions after formula (208).

[Ste89] J.Steinberger; Experimental Status of CP Violation; talk at the XXVth Anniversary of CP Violation Discovery, Chateau de Blois, France, 1989; printed in: CP Violation in Particle and Astrophysics; ed. by J. Tran Thanh Van; Editions Frontières; 1990, ISBN 2-86332-071-8.

[Wah89] H.Wahl; Cisatlantic Rare Kaon Decays; CERN-EP/89-86 (1989).

[Wei30] V.Weisskopf, E.Wigner; Berechnung der natürlichen Linienbreite auf Grund der Diracschen Lichttheorie; Zeitsch. f. Ph. **63**(1930)54 and: Über die natürliche Linienbreite in der Strahlung des harmonischen Oszillators; Zeitsch. f. Ph. **65**(1930)18.

[Wic58] G.C.Wick; Invariance Principles of Nuclear Physics; Ann. Rev. Nucl. Sci. **8**(1958)1.

[Wig32] E.Wigner; Über die Operation der Zeitumkehr in der Quantenmechanik; Gött. Nachr., Math. Naturw. Kl. (1932)546.

[Wol64] L.Wolfenstein; Violation of CP Invariance and the Possibility of Very Weak Interactions; Phys. Rev. Lett. **13**(1964)562.

[Wu57] C.S.Wu et al.; Experimental Test of Parity Conservation in Beta Decay; Phys. Rev. **105**(1957)1413.

[Wu64] T.T.Wu, C.N.Yang; Phenomenological Analysis of Violation of CP Invariance in Decay of K^0 and $\overline{K}^0$; Phys. Rev. Lett. **13**(1964)380.

Chapter 2

[Buc92] NA48 Collaboration, presented by P.Buchholz; The NA48 Liquid Krypton Calorimeter; Nucl. Instr. Meth. **A316**(1992)1.

[NA31/88] H.Burkhardt et al.; NA31 Collaboration; The Beam and Detector for a High-Precision Measurement of CP Violation in Neutral-Kaon Decays; Nucl. Instr. Meth. **A268**(1988)116.

[NA48/90] G.D.Barr et al.; NA48 Collaboration; Proposal for a Precision Measurement of ε'/ε in CP Violating $K^0 \to 2\pi$ decays; CERN/SPSC/90-22 SPSC/P253 (1990).

[NA48/90/2] NA48 Collaboration; Memorandum; SPSC/P253 Add. 1. (1990).

[NA48/91] NA48 Collaboration; Memorandum; Status Report on NA48; CERN/SPSLC 91-58 SPSLC-M479 (1991).

[NA48/92] G.D.Barr et al.; NA48 Collaboration; The NA48 Liquid Krypton Calorimeter Prototype; Nucl. Instr. Meth. **A323**(1992)393.

[Note92/4] H.Blümer; Status of the NA48 Tagging Counter; NA48 Note92/4.

[Schi] D.Schiuma; private communication, the original Monte Carlo simulation was done by R.Carosi.

Chapter 3

[Ama81] U.Amaldi; Fluctuations in Calorimetry Measurements; Phys. Scr. **23**(1981)409.

[Bet34] H.Bethe, W.Heitler; Proc. Roy. Soc. **A146**(1934)83.

[BNL90] Brookhaven National Laboratory; SSC Detector R&D at BNL; ed. by B.Yu and V.Radeka; BNL 52244 (1990).

[DELPHI85] A.Cattai et al.; Status of the High Density Projection Chamber; Nucl. Instr. Meth. **A235**(1985)310.

[DELPHI87] F.Navarria; Some Aspects of the DELPHI HPC Project; Nucl. Instr. Meth. **A257**(1987)499.

[D0/88] S.Aronson et al.; Hadron and Electron Response in a Uranium Liquid Argon Calorimeter from 10 to 150 GeV; Nucl. Instr. Meth. **A269**(1988)492.

[Fab82] C.W.Fabjan, T.Ludlam; Calorimetry in High-Energy Physics; Ann. Rev. Nucl. Part. Sci. **32**(1982)335.

[Fab89] C.W.Fabjan, R.Wigmans; Energy Measurement of Elementary Particles; Rep. Prog. Phys. **52**(1989)1519.

[Fab92] C.W.Fabjan; Detectors, Particle, Calorimetric; Enc. Appl. Phys. **4**(1992)485.

[Gar60] R.L.Garwin; The Collection of Light from Scintillation Counters; Rev. Sci. Instr. **31**(1960)1010.

[H1/88] W.Braunschweig et al.; Results from a Test of a Pb-Cu Liquid Argon Calorimeter; Nucl. Instr. Meth. **A265**(1988)419.

[L3/88] L3 Collaboration, pres. by R. Sumner; The L3 BGO Electromagnetic Calorimeter; Nucl. Instr. Meth. **A265**(1988)252.

[MARS83] C.Cerri et al.; MARS, a fine grain Aluminium-Liquid Argon Calorimeter; Nucl. Instr. Meth. **214**(1983)217.

[Mei30] L.Meitner, W.Orthmann; Über eine absolute Bestimmung der Energie der primären β-Strahlen von Radium E; Z. f. Phys. **60**(1930)143.

[Mül72] D.Müller; Electron Showers of High Primary Energy in Lead; Phys. Rev. 5(1972)2677.

[NA31/88] H.Burkhardt et al.; NA31 Collaboration; The Beam and Detector for a High-Precision Measurement of CP Violation in Neutral-Kaon Decays; Nucl. Instr. Meth. **A268**(1988)116.

[Ort30] W.Orthmann; Ein Differentialkalorimeter zur Absolutbestimmung kleinster Wärmemengen; Z. f. Phys. **60**(1930)137.

[Rad88/1] V.Radeka; Low-Noise Techniques in Detectors; Ann. Rev. Nucl. Part. Sci. **38**(1988)217.

[Rad88/2] V.Radeka; Speed and Noise Limits in Ionization Chamber Calorimeters; Nucl. Instr. Meth. **A265**(1988)228.

[RD3/92] B.Aubert et al.; RD3 Collaboration; Performance of a Liquid Argon Accordion Calorimeter with Fast Readout; Nucl. Instr. Meth. **A321**(1992)467.

[Ros41] B.Rossi, K.Greisen; Cosmic-Ray Theory; Rev. Mod. Phys. **13**(1941)240.

[UA1/91] UA1 Collaboration; Performance of a Uranium/Tetramethylpentane Calorimeter Backed by an Iron/Scintillator Calorimeter; Nucl. Instr. Meth. **A305**(1991)331.

[Wig87] R.Wigmans; On the Energy Resolution of Uranium and other Calorimeters; Nucl. Instr. Meth. **A259**(1987)389.

[Wig91] R.Wigmans; Advances in Hadron Calorimetry; Ann. Rev. Nucl. Part. Sci. **41**(1991)133.

[Wil74] W.J.Willis, V.Radeka; Liquid-Argon Ionization Chambers as Total-Absorption Detectors; Nucl. Instr. Meth. **120**(1974)221.

[Yud69] T.Yuda; Electron-Induced Cascade Showers in Inhomogeneous Media; Nucl. Instr. Meth. **73**(1968)301.

Chapter 4

[Buch] P.Buchholz, private communication.

[Coll2/93] A.Norton; Minutes of the NA48 Collaboration Meeting; Feb. 93.

[Mart] M.Martini, private communication.

[Min3/6/93] V.Marzulli; Minutes of the NA48 LKr 1993 test meeting; July 3th, 1993.

[NA48/93] V.Fanti et al.; NA48 Collaboration; Performance of the NA48 Liquid Krypton Prototype Calorimeter; to be published.

[Note91/5] P.Buchholz, E.Steininger, B.Überschär, G.Viehhauser; Measurement of the Calibration Capacitances and Resistances for the Liquid Krypton Calorimeter, 1991; NA48 Note91/5.

[Note91/9] B.Hallgren, G.Laverierre; A Modular 100 ns Shaper and Linear Fanout; NA48 Note91/9.

Chapter 5

[Coll12/92] E.Mazzucato; Minutes of the NA48 Collaboration Meeting; Dec. 92.

[Coll4/93] P.Debu, E.Mazzucato; Minutes of the NA48 Collaboration Meeting; Apr. 93.

[Fon67] C.Y.Fong, C.Kittel; Induced Charge on Capacitor Plates; Am. J. Phys. **35**(1967)1091.

[Mil68] L.S.Miller, S.Howe, W.E.Spear; Charge Transport in Solid and Liquid Ar, Kr, and Xe; Phys. Rev. **166**(1968)871.

[Min13/5/92] T.Stemmler; Minutes of the NA48 weekly meeting; May 13th, 1992.

[Ros49] B.Rossi, H.Staub; Ionization Chambers and Counters, Experimental Techniques; McGraw-Hill, New York (1949); p.49 ff.

[Yos76] K.Yoshino, U.Sowada, W.F.Schmidt; Effect of Molecular Solutes on the Electron Drift Velocity in Liquid Ar, Kr, and Xe; Phys. Rev. **A14**(1976)438.

Acknowledgements

I would like to thank Prof. Meinhard Regler for his continuous support and motivation during my studies and during this work.

For his supervision during my stay at CERN I wish to thank my friend Peter Buchholz. I profited a lot from his suggestions and learned much about high energy physics in numerous fruitful discussions with him.

I would like to thank my group leaders at CERN, Dieter Schinzel and Heiner Wahl, for the possibility to work in their group and many helpful discussions.

Many valuable suggestions for the FADC analysis were contributed by Erich Griesmayer. The analysis of the WFA and the calculation of the charge collection effects profited from discussions with Daniele Schiuma and Piet Wertelaers.

I am very grateful to Günther Neuhofer for his support of my appointment as a technical student.

My special thanks belong to Giles Barr for the very careful proof-reading of this work.

I am very grateful to all members of the NA48 collaboration for the warm reception and the environment that made this work possible. Special thanks are dedicated to the members of the software group, especially to Ginette Bouquet and Paolo Calafiura for their fast and untiring help in technical problems with the off-line program.

I want to thank my mother, Martina Viehhauser, who passed on to me her dedication to science and who always supported me in gaining the experiences that contributed to this work.

My biggest gratitude belongs to Silvia. Apart from her help in proof-reading this work she was a permanent source of power and I acknowledge her readiness to accompany me to Geneva.

Finally, I would like to thank all my friends, in physics and elsewhere, who influenced my way of thinking and working. They might find the outcome of our discussions in this work.